PROPERTIES OF THE SIMULATED AGN ACTIVITY FUNCTION IN

ISOLATED GALAXY MERGERS

by

Maan H. Hani

A Thesis Submitted to
Saint Mary's University, Halifax, Nova Scotia
in Partial Fulfillment of the Requirements for
the Degree of Master of Science in Astronomy
(Department of Astronomy and Physics)

August 2015, Halifax, Nova Scotia

Approved:	Dr. Robert Thacker
	Advisor
Approved:	Dr. Luigi Gallo
	Examiner
Approved:	Dr. David Guenther
	Examiner
Date:	Aug 25$^{\text{th}}$, 2015

إلى العيون الطّيبة التي رافقتني...
إلى والديّ حكمت وأليسار

أهدي هذه الأطروحة.

Acknowledgments

I would like to express my deepest gratitude to my research supervisor and mentor, Professor Rob Thacker, for his patient guidance, enthusiastic encouragement and useful critiques of this research work. This work would not have been possible without his enormous efforts and support. Next, I would like to express my sincere gratitude to Dr. James Wurster for his encouragement, support, helpful advice, and for providing the models and some simulation results used in this study. I would also like to thank (Guru) Dave Lane who has been a great source of knowledge, and extremely effective at fixing the clusters after I am done breaking them.

During my time at Saint Mary's University, I had the opportunity to interact with amazing faculty members and administrative staff. Their support, and guidance made this journey full of amazing memories. Thank you all! I would like to particularly thank the faculty members on my committee, Professors David Guenther and Luigi Gallo, for their time, support, suggestions, and useful discussions.

Dr. Daniel Majaess provided me with endless support, the voice of wisdom, great discussions, useful insight, and helpful advice for which I am grateful.

I have also been blessed with a friendly and cheerful group of fellow graduate students: The Godfather and King of DurDaloo (aka. Amit), Anneya, Bobby, Diego, Jaspreet(o), Jenn(y), Jess, Kirsten, Liz, Mitch, Nozhan, Sam.

Beyond Astrophysics, I would like to thank all my friends who have made Halifax feel like home!

As always, I am grateful and profoundly indebted to my family, whose value to me only grows with time. They have been an indispensable source of support and encouragement.

Contents

List of Tables

List of Figures

Abstract

Properties of the simulated AGN activity function in isolated galaxy mergers

by Maan H. Hani

Numerical modeling of active galactic nuclei (AGN) poses many challenges, from uncertainties about the underlying physics to dynamic range issues. We present a study of simulated activity functions (AF; the differential of the amount of time spent by a black hole above a given Eddington ratio) in simulations of mergers of Milky-Way like galaxy models using seven different BH feedback algorithms, accretion algorithms, and initial conditions. When considered over the entire simulation the simulated AFs are more dominant at high Eddington ratios than observationally (Schechter-type) inferred AFs. However, during passive evolutionary stages there is considerably closer agreement with observational results. We also demonstrate that two separate algorithms produce AFs which are approximately mass invariant, in agreement with observations. Lastly, we show that numerical uncertainties in AFs and other properties of the remnant such as black hole mass, star formation rates, and accretion rates, are well below a factor of two.

Aug 25th, 2015

Chapter 1

INTRODUCTION

In the past century, the study of cosmological structure formation and evolution has emerged as an established field of astrophysics. Since the Great Debate (Shapley-Curtis Debate) in May of 1921, followed by Edwin Hubble determining the distance to M31 (Hubble 1929), a vast legacy of research has been accumulated. Thanks to this research, our understanding of the formation of structure and its evolution has been remarkably enhanced.

Galaxy formation and evolution can best be understood by dividing them into two separate stages. Although such a separation may be somewhat unnatural, it provides valuable insight into the physics and processes that affect the formation and evolution of galaxies. We first examine the formation of structure from minuscule inhomogeneities in the early universe (observed in the Cosmic Microwave Background Radiation) in section 1.1.3 and then discuss the processes that affect galaxy formation and evolution in sections 1.2 and 1.3.

1.1 STRUCTURE FORMATION

Developing a precise understanding of the origin and evolution of structure is one of the most important issues in modern astrophysics. Observations provide strong evidence that present day structures evolved from a nearly homogeneous early universe. However, there remain many unanswered questions as to what happened between that nearly homogeneous state and today. Therefore, the understanding of the formation and evolution of structure, requires a detailed knowledge of the early universe as well as the physics governing its evolution.

1.1.1 FRIEDMANN'S EQUATION

The theory of General Relativity has had an enormous impact on our understanding of the evolution of the universe. Einstein's field equation describes the relation between spatial geometry and mass-energy; it is written as

$$\mathcal{G}_{\mu\nu} = -\frac{8\pi G}{c^4}\mathcal{T}_{\mu\nu},$$ (1.1)

where G is Newton's gravitational constant, $\mathcal{T}$ is the stress-Energy tensor which evaluates the effect of a given mass-energy distribution on the nature of space time, and $\mathcal{G}$ is the Einstein tensor. The field equation can be thought of as the relativistic equivalent of Poisson's equation in Newtonian mechanics, and in the so-called weak field limit, reproduces Poisson's equation.

By imposing the Cosmological Principle, that the universe is isotropic and homogeneous, and then solving Einstein's field equation, one can derive a relationship that describes the evolution of the universe. This relationship is known as Friedmann's equation and can generally be expressed as (e.g. Ryden 2003):

$$\left(\frac{\dot{a}}{a}\right)^2 = \frac{8\pi G}{3c^2}\epsilon(t) - \frac{\kappa c^2}{R_0^2}\frac{1}{a(t)^2},$$ (1.2)

where R_0 is the radius of the curvature of the universe, a is the scale factor of the universe, and ϵ is the cumulative energy density contribution of matter, radiation and vacuum ($\epsilon = \epsilon_m + \epsilon_r + \epsilon_\Lambda$). κ is a parameter describing the geometry of the universe: it can take values of 1, 0, or -1 corresponding to a closed, flat or open universe, respectively.

Introducing three new parameters, one can arrive at a more useful form of the equation. Define the Hubble parameter H such that:

$$H(t) = \frac{\dot{a}(t)}{a(t)},$$ (1.3)

and, by association, the critical density ϵ_c for which $\kappa = 0$ such that:

$$\epsilon_c(t) = \frac{3c^2 H(t)^2}{8\pi G}. \tag{1.4}$$

Let the dimensionless density Ω be defined as:

$$\Omega_i(t) = \frac{\epsilon_i(t)}{\epsilon_c(t)}, \tag{1.5}$$

where i represents different components of the universe (radiation, matter, vacuum).

Substituting the dimensionless density and the Hubble parameter into equation 1.2, Friedmann's equation[1] can be rearranged into the following unit-less form:

$$\left(\frac{H(t)}{H_0}\right)^2 = \frac{\Omega_{r,0}}{a(t)^4} + \frac{\Omega_{m,0}}{a(t)^3} + \Omega_{\Lambda,0} + \frac{1 - \Omega_0}{a(t)^2} \tag{1.6}$$

where $H_0 = H(t_0)$ is the Hubble constant in today's universe, $\Omega_0 = \Omega_m(t_0) + \Omega_r(t_0) + \Omega_\Lambda(t_0)$, and the curvature of the universe (κ) is expressed in terms of the total energy density.

In this form, Friedmann's equation expresses the global change in the scale factor of the universe as a function of time and energy density. The change in the scale factor is an important quantity which is to be considered when studying structure formation and evolution; it is also used as a key parameter in cosmological simulations.

1.1.2 The ΛCDM Universe

Following Einstein's and de Sitter's work in 1917, Friedmann and Lemaître proposed a more generalized universe that consists of radiation, matter and the cosmological constant (Λ). The Friedmann-Lemaître universe can be reduced to the Einstein-deSitter universe by ignoring the cosmological constant. In the past two decades, various observations have supported the Friedmann-Lemaître universe by providing evidence[2]

---

[1] Note that equation 1.6 explicitly assumes a Friedmann-Lemaître universe which is considered to be a good model of the universe we live in (see §1.1.2).

[2] Note that the initial evidence for dark matter predates the past two decades (see Rubin and Ford 1970 and Rubin et al. 1978).

for dark matter and the cosmological constant. We next review the aforementioned observational evidence and highlight some general facts about dark matter and the cosmological constant.

Dark Matter

The observable universe is comprised of radiative baryonic matter in the form of gas, dust, and stars. On galactic scales and larger, the observed baryonic matter is believed to be embedded in dark matter halos that dominate the gravitational potential (first postulated by F. Zwicky; Zwicky 1933, 1937). While the exact nature of dark matter remains unknown, some of its basic properties are understood: dark matter is collision-less matter that, in the current evolutionary epoch, *only* interacts gravitationally with other matter.

The mass distributions inferred from observations and kinematic studies show that large structures, such as galaxies and clusters of galaxies, significantly differ from mass distributions of luminous matter (e.g. the Bullet Cluster). Rotation curves of spiral galaxies also indicate that a significant fraction of the mass is unaccounted for when only considering the luminous mass (e.g. van Albada et al. 1985; Rubin et al. 1978; Rubin and Ford 1970). Moreover, gravitational lensing studies conducted using galaxy clusters show that the luminous mass (in galaxies and X-ray gas) represents an insignificant fraction of the total mass of a given cluster (e.g. Subramanian et al. 1987).

Dark matter can be broadly categorized into two models, although there is arguably a spectrum of possibilities including mixtures. The cold dark matter (CDM) model considers dark matter to comprise non-relativistic, and gravitationally interacting particles. The rival model, considers dark matter to be relativistic, at matter-radiation decoupling, and it is known as the hot dark matter (HDM) model. Observations of structure formation favor models incorporating CDM (see §1.1.3). Note that CDM is easily modeled within the Friedmann equation as pressure-less dust.

The Cosmological Constant (Λ)

The cosmological constant, first introduced by Einstein to allow for a *static* universe, is now considered a necessary component of our universe. Various observations support the need for a cosmological constant (e.g. Barrow and Saich 1993; Riess et al. 1998; Perlmutter et al. 1999). Some of the main arguments are:

- Age calculations using a decelerating universe (matter only) yield an age ($\approx$ 9 Gyr) lower than the age of the oldest stars ($\gtrsim 13\,\mathrm{Gyr}$).

- The observed flatness of the universe is not possible when only considering the observed matter density. Invoking the cosmological constant reconciles the flatness problem.

- Supernovae (which can be used as "standard candles") at high redshift appear to be dimmer than what would be expected in a matter only (decelerating) universe.

Taken together, the arguments/observations supporting CDM and the cosmological constant are combined into the ΛCDM model.

1.1.3   FROM PERTURBATIONS TO STRUCTURE

Theoretical models can essentially trace the observed structure in today's universe back to slight inhomogeneities in the early universe (e.g. Springel et al. 2005b). These density inhomogeneities are observed as temperature perturbations in the Cosmic Microwave Background (CMB; figure 1.1) and can be described to high accuracy by a Gaussian field. The CMB photons we observe date back to the era of recombination when the temperature dropped sufficiently to make the early universe optically thin to radiation less energetic than the ionization energy of Hydrogen[3]. The escaped photons were then cosmologically redshifted from the high energies of the early universe to the microwave frequencies that we observe today. As the universe continued to expand,

---

[3]Note that even after the universe is optically thin to some radiation, some wavebands are still absorbed.

the inhomogeneities grew and acted as seeds for the observed structure in today's universe. The details of the evolution of the inhomogeneities are highly dependent on the geometry and energy density of the universe.
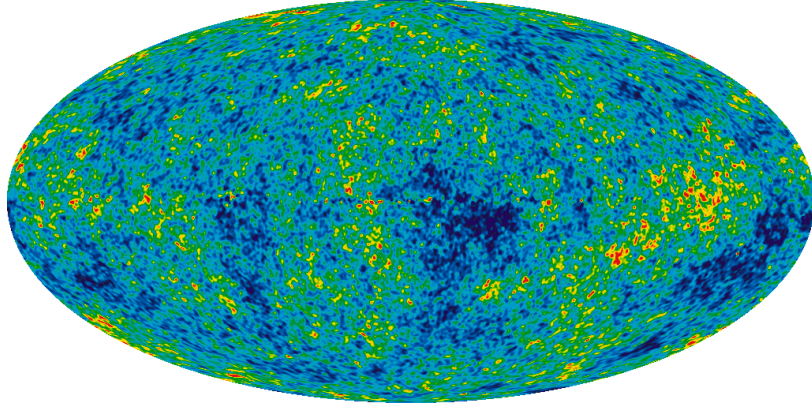
Figure 1.1: Simulated WMAP Cosmic Microwave Background (CMB) map showing the slight inhomogeneity of the early universe represented as small perturbations at the last scattering surface (NASA-WMAP Science team, WMAP # 121238; used within the normal NASA Image Use Guidelines).

Growth of Perturbations

One can gain significant understanding of the growth and evolution of structure in today's universe by examining the effects of expansion on a single perturbation. Consider a spherical over-density, of radius $R(t)$ surrounded by a uniform density[4] $\bar{\rho}(t)$. The density of the sphere can be expressed as:

$$\rho(t) = \bar{\rho}(t) \left[1 + \delta(t) \right], \tag{1.7}$$

where $\delta(t)$ represents a perturbation. The acceleration of the growth of the sphere can be expressed in terms of the density as follows (e.g. Ryden 2003):

$$\frac{\ddot{R}(t)}{R(t)} = \frac{-4\pi G}{3} \bar{\rho}(t) \left[1 + \delta(t) \right]. \tag{1.8}$$

---

[4]Often called the "Swiss Cheese" model.

Imposing the principle of conservation of mass and noting that the scale factor, $a(t)$, is proportional to $\bar{\rho}(t)^{-1/3}$, we can write (for small perturbations):

$$\frac{\ddot{a}(t)}{a(t)} - \frac{1}{3}\ddot{\delta}(t) - \frac{2}{3}\frac{\dot{a}(t)}{a(t)}\dot{\delta}(t) \propto -\frac{4\pi G}{3}\bar{\rho}(t)\left[1 + \delta(t)\right]. \qquad (1.9)$$

Subtracting the expansion of the background universe, $\frac{\ddot{a}(t)}{a(t)} = -\frac{4\pi G}{3}\bar{\rho}(t)$, the growth of the perturbation can then be expressed as:

$$\frac{1}{3}\ddot{\delta}(t) + \frac{2}{3}H(t)\dot{\delta}(t) \propto \frac{4\pi G}{3}\bar{\rho}(t)\delta(t), \qquad (1.10)$$

where $H(t)$ is the Hubble parameter (see equation 1.3).

Radiation dominated universe	Matter dominated universe[5]	Λ dominated universe
$\Omega_m \ll 1$	$\Omega_m \simeq 1$	$\Omega_m \ll 1$
$\delta(t) \propto \ln(t)$	$\delta(t) \propto t^{2/3} \propto a(t)$	$\delta(t) \simeq constant$

Table 1.1: The growth of over-densities in a flat single-component universe (solutions to equation 1.10).

Equation 1.10 can be solved analytically for a flat, single-component universe (the results are shown in table 1.1). Dark matter perturbations grow as described by equation 1.10. However, the baryon-photon fluid oscillates about an equilibrium state (due to gravity and pressure) until decoupling occurs when the baryons fall into the dark matter potential wells and start forming structures while the photons escape. This model explains the temperature fluctuations observed in the CMB as well as the large scale structure observed today.

Heirarchical Structure Formation

Dark matter halos begin forming before any baryonic matter structure can. Therefore, the formation of structure is explicitly dependent on the properties and structure of dark matter. The two dark matter models, discussed in section 1.1.2, predict drastically different structure formation scenarios. Because of the relativistic nature of dark

---

[5]White (1993) showed, using a linear perturbation derivation, that perturbations in an Einstein de Sitter universe grow proportional to the scale factor.

matter particles in the HDM model, free-streaming of particles smooths small scale fluctuations. Therefore, in an HDM universe, large structures such as super clusters and galaxy clusters form first then fragment to form smaller structures (groups then galaxies). This formation scenario is known as the top-down formation scenario. On the other hand, in a CDM universe, structure forms in a hierarchical, bottom-up fashion. The bottom-up scenario predicts small structures (galaxies) forming first then combining to form larger structures (groups, clusters, and super clusters). Figure 1.2 depicts the bottom up formation scenario.

Observations favor the bottom-up scenario: Galaxies at high redshifts are observed to be smaller than local galaxies. Also, galaxy clusters are not observed at high redshifts. Moreover, mergers are observed to be more common at high redshift. However, it is worth noting that the most massive and active systems at high redshift have turned quiescent[6] while systems exhibiting less activity (less luminous systems) are successively more dominant at lower redshifts (e.g. Ueda et al. 2003; Hopkins et al. 2008; this is known as cosmic downsizing (see §1.2.3).

1.2 GALAXY EVOLUTION

A key part of understanding galaxy evolution is examining the different processes, both environmental and internal, that can affect the evolution of the galaxy.

1.2.1 GALAXIES IN THEIR NATURAL HABITAT

Galaxies are often observed in groups or clusters. The environment a galaxy resides in has a notable effect on its evolution. Various mechanisms have been proposed to explain the effect of the environment on galaxy evolution. Below we provide a brief list of those mechanisms:

i. **Harassment:** High speed galaxy encounters result in impulsive heating therefore increasing the internal energy of a galaxy. The galaxy becomes less bound and more vulnerable to disruptions. This scenario is important in explaining the

---

[6]Otherwise the most massive and active galaxies would be forming today.
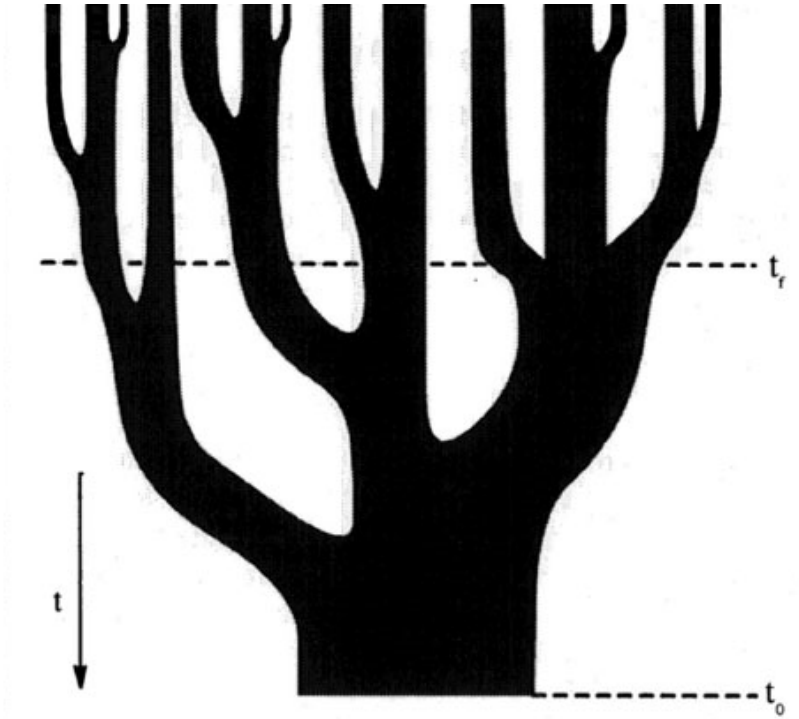
Figure 1.2: A schematic representation of a merger tree depicting the growth of a halo (Lacey and Cole 1993; used with the permission of C. Lacey).

transition of late-type spiral galaxies into dwarf ellipticals where the mass loss and perturbation of stellar orbits becomes evident (e.g. Farouki and Shapiro 1981; Moore et al. 1998).

ii. **Cannibalism/Mergers:** In this scenario, a massive galaxy can merge with a less massive satellite galaxy resulting in a more massive galaxy. Note that for merger ratios approaching unity, the interaction is referred to as a major merger.

iii. **Strangulation:** In this scenario as the galaxy moves in a cluster, it interacts with the intra-cluster medium which strips its gas halo causing a gradual decrease in the star formation rate. With the decreasing star formation as there is no halo gas to fuel further star formation, the galaxy becomes redder and fainter (e.g. Larson et al. 1980).

iv. **Ram Pressure Stripping:** Similar to the Strangulation scenario, interactions with the intra-cluster medium strips the galaxy's gas reservoir. In this case the

9

gas being stripped is from the gaseous disc. The effect is similar: The star formation rates diminish. This scenario is consistent with observations showing that star formation rates are lower in clusters (e.g. Gunn and Gott 1972; Abadi et al. 1999).

v. **Tidal Stripping:** In this scenario, tidal forces during close galaxy fly-bys cause smaller (less bound) galaxies to be stripped of their gas. This gas can be accreted onto the more massive galaxy therefore replenishing its gas reservoir while depleting the lower mass galaxy's gas (Dekel et al. 2003; Diemand et al. 2007).

1.2.2 Star formation and Stellar Feedback

Galactic evolution is strongly governed by the rate at which gas is converted into stars as well as the evolution of the stellar population. Therefore, tracking the galactic gas reservoir plays a vital role in understanding galaxy evolution. An important factor that must be understood when considering galaxy evolution is star formation: Star formation and stellar feedback directly influence the gas reservoir both depleting/repleting it while altering its overall properties. Supernovae (SN) explosions and winds from Asymptotic Giant Branch (AGB) stars can compress a molecular cloud inducing star formation (Kawata et al. 2014). Conversely, both SN explosions and AGB winds can heat up the gas or eject the gas from the galactic disc therefore hindering star formation (Oppenheimer and Davé 2006).

1.2.3 Downsizing

Observations indicate that the most luminous and most active galaxies were at redshift $z \sim 2$ (Shaver et al. 1996; Madau et al. 1996). At $z \sim 2$, galaxies hosted the most active supermassive black holes (SMBHs) with masses $M_{BH} \sim 10^9 \, M_\odot$ (e.g. Hasinger et al. 2005; Kriek et al. 2007; Hopkins et al. 2008), and exhibited the highest star formation rates (e.g. Hopkins 2004 and references therein; Madau et al. 1996; Behroozi et al. 2013; Bell et al. 2005). At lower redshifts, the most massive BHs start to accrete at lower rates while the less massive ones continue to grow subject to the

availability of fuel (Hopkins et al. 2008); additionally the star formation rates decrease (Behroozi et al. 2013). This is evident in the consistent increase in the number density of the less luminous and less active galaxies peaks with lower redshifts (Ueda et al. 2003). This decrease in the activity/star formation of the most active/star forming galaxies since $z \sim 2$ is referred to as "Downsizing"[7].

The decrease in activity and star formation is directly observed as a decrease in the total luminosity. Such a decrease in luminosity can be achieved by depleting the galactic gas reservoir (heating or ejecting the gas from the galaxy), therefore suppressing star formation and BH activity. Without young stars forming and replenishing the radiation engine of the galaxy, the galaxy will become red and faint (*red and dead* galaxies). Likewise, the lack of gas being accreted onto the central BH will have similar effects on the galaxy. Various mechanisms have been proposed to cause the observed downsizing. As mentioned in section 1.2.2, stellar feedback (i.e. supernovae, AGB winds) can drive star formation to a halt. Feldmann and Mayer (2015) showed using numerical simulations, and under certain assumptions for feedback, that star formation could play an important role in quenching massive galaxies. However, Silk and Mamon (2012) argue that stellar feedback is not strong enough to solely account for downsizing; additional feedback mechanisms are needed to quench residual star formation and maintain low star formation rates (contrary to Feldmann and Mayer 2015). Another proposed mechanism, which is becoming increasingly popular in research, is virial shock heating where the in-falling cool gas is heated by virial shocks when penetrating the hot gas medium (Dekel and Birnboim 2006). As a result, the hot/dilute gas becomes more vulnerable to feedback mechanisms. Active galactic nuclei (AGN) feedback, which is discussed in more detail in section 1.3.4, has also been proposed as mechanism to explain downsizing. Accretion of gas onto an AGN will return enough energy into the environment to quench the galaxy (e.g. Fabian 2012). While not universally agreed, AGN feedback is widely viewed as a major contributor to downsizing.

---

[7]This term was coined by Cowie et al. (1996)

1.3 Black Hole-Galaxy Co-evolution

1.3.1 Super Massive Black Holes (SMBH)

Observational Evidence

Although the concept of Black Holes (BH) dates back to the 18$^{\text{th}}$ century, they were not commonly accepted until the late 20$^{\text{th}}$ century. Several observations support the existence of super massive black holes (SMBHs) at the center of most galaxies (e.g. Kormendy and Richstone 1995; Ferrarese and Merritt 2000). Observations of the central star cluster dynamics, in the Milky Way, reveal high stellar velocities that are consistent with a massive and dense central object ($\sim 10^6 \, M_\odot$; e.g. Gillessen et al. 2009). Alos, the central regions of other galaxies are observed in X-ray light. The observed X-ray luminosities (e.g. Komossa 2001) are consistent with an accretion disc which is associated with SMBHs. Moreover, some galaxies show evidence of relativistic jets originating from their centers. BHs provide suitable explanations for such jets (e.g. Begelman et al. 1984) although the phenomenon by which the jets are created is still somewhat poorly understood.

Proposed Formation Scenarios for 'Seed' SMBHs

Many scenarios have been proposed for the formation of the seed BHs that then evolve into SMBHs. However, no formation scenario is widely accepted to date. Here we present a brief summary of the major proposed formation scenarios:

i. **Population III (popIII) Stars:** This scenario proposes that today's SMBHs formed from the direct collapse of massive popIII stars (e.g. Madau and Rees 2001). A $260 \, M_\odot$ popIII star can collapse and form a $100 \, M_\odot$ BH. Recent numerical studies show that fragmentation of the progenitor gas cloud is expected to be common in popIII star formation (e.g. Turk et al. 2009; Stacy et al. 2012). However, clusters and binary systems of popIII stars with masses $\sim 100 \, M_\odot$ should be common.

ii. **Direct Collapse:** Another proposed scenario is SMBH formation through the direct collapse of gas (e.g. Loeb and Rasio 1994; Begelman et al. 2006). This scenario requires no fragmentation and low gas angular momentum. However, the details of the BH formation from gas in-fall remains unclear.

iii. **Collapsing Cluster:** Observations show evidence of nuclear star clusters. Such clusters can undergo collapse and form a SMBH (e.g. Begelman and Rees 1978).

iv. **Primordial Black Holes (BHs):** Some theories propose that primordial BHs can exists with masses $M_{BH} < 10^5 \, \mathrm{M_\odot}$. However, Ricotti et al. (2008) used distortions in the CMB to argue that primordial BH mass must obey $M_{BH} < 10^3 \, \mathrm{M_\odot}$.

Growth of BHs

The aforementioned SMBHs are thought to grow via BH mergers or accretion of gas and stars. As gas spirals into the central region, it settles into an accretion disc after losing some of its angular momentum (e.g. Hobbs et al. 2012). The gas then migrates inwards in the disc as it loses more angular momentum due to viscous mechanisms. The two most commonly studied models for accretion discs are: (1) the geometrically thin, optically thick (radiatively efficient; Shakura and Sunyaev 1973) and (2) the geometrically thick, optically thin (radiatively inefficient; e.g. Narayan and Yi 1994; Narayan et al. 1998).

As matter is accreted into the BH, some of it is converted into energy that is returned into the surrounding environment. The produced luminosity (L) can be expressed in terms of the accretion rate $\dot{M}$, the speed of light c, and a radiative efficiency η as follows:

$$L = \eta \dot{M} c^2 \tag{1.11}$$

The radiative efficiency (typically $\eta = 0.1$) is the efficiency of extracting energy from the inner most circular orbit around the BH (e.g. Springel et al. 2005a).

Bondi Accretion

To calculate the accretion rate of gas onto a SMBH, assume, for simplicity, a static BH of mass M_{BH} with zero spin surrounded by a non-rotating polytropic gas. The gas's density is assumed to be uniform at infinity (ρ_∞; Hoyle and Lyttleton 1939; Bondi and Hoyle 1944). In this case the accretion of the gas will be temperature-limited and the accretion rate, $\dot{M}_{t-l}$, is given by:

$$\dot{M}_{t-l} = \frac{4\pi\lambda G^2 M_{BH}^2 \rho_\infty}{c_\infty^3}, \tag{1.12}$$

where c_∞ is the speed of sound at infinity, and λ is a dimensionless parameter dependent on the adiabatic parameter. However, if the BH was moving through the infinite gas cloud at a steady speed (v) relative to the distant parts of the cloud, the BH's gravity will direct the gas into a wake which is then accreted onto the BH. The gas will accrete at a velocity-limited rate, $\dot{M}_{v-l}$, given by

$$\dot{M}_{v-l} = \frac{2\pi\alpha G^2 M_{BH}^2 \rho_\infty}{v^3}, \tag{1.13}$$

where α is a dimensionless parameter of order unity ($\alpha \in [1:2]$; Bondi 1952).

Bondi (1952) interpolated the temperature-limited (equation 1.12) and velocity-limited (equation 1.13) accretion rates to obtain the Bondi rate[8] for spherically symmetric accretion of gas with uniform density onto a point mass with an adiabatic index $\gamma = \frac{3}{2}$. Equation 1.14 gives the Bondi accretion rate corrected by a factor of two, on the basis of numerical simulations by Shima et al. (1985), to match the Hoyle-Lyttleton rate (equation 1.12) at insignificant sound speeds,

$$\dot{M}_{Bondi} = \frac{4\pi G^2 M_{BH}^2 \rho_\infty}{(c_\infty^2 + v^2)^{3/2}}. \tag{1.14}$$

---

[8]also known as the Bondi-Hoyle-Lyttleton accretion rate

Eddington Accretion

The maximum accretion rate[9] that a BH can achieve, assuming that the gas surrounding the BH is isotropic and in hydrostatic equilibrium, is known as the Eddington accretion rate[10], $\dot{M}_{Edd}$. The luminosity associated with the Eddington rate is known as the Eddington Luminosity and is given by

$$L_{Edd} \equiv \frac{4\pi G M_{BH} m_p c}{\sigma_T}, \tag{1.15}$$

where m_p is the proton mass, σ_T is the Thomson cross section, and c is the speed of light. This luminosity will be generated by an Eddington accretion rate given by (see equation 1.11)

$$\dot{M}_{Edd} \equiv \frac{4\pi G M_{BH} m_p}{\eta \sigma_T c}. \tag{1.16}$$

Eddington Ratio

The Eddington luminosity and accretion rate provide a useful relative scale to measure accretion rates. Knowing that BHs vary in properties (mass and therefore luminosity and accretion rate), it is quite convenient to be able to normalize BH luminosities and accretion rates for comparison across different luminosity regimes. Hence, we introduce the Eddington ratio (λ). The Eddington ratio, given by equation 1.17, represents the BH luminosity (L) normalized by the Eddington luminosity (L_{Edd}).

$$\lambda \equiv \frac{L}{L_{Edd}}. \tag{1.17}$$

Equivalently, using equation 1.11, the Eddington ratio is the accretion rate normalized by the BH mass.

$$\lambda \propto \frac{\dot{M}_{BH}}{M_{BH}}. \tag{1.18}$$

---

[9]Note that the Eddington limit can be surpassed (super-Eddington accretion) by breaking the balance between radiative pressure and gravitational forces if the BH environment (gas distribution) is not isotropic.

[10]also referred to as the Eddington limit

Therefore, the Eddington ratio is arguably a more useful quantity when comparing the activity of different BHs.

1.3.2 Observational Evidence of BH-Galaxy Co-evolution

The co-evolution of black holes (BHs) and galaxies, widely viewed as an important factor in galaxy evolution, supported by various observed correlations between BH properties and galaxy properties (for example, bulge mass and luminosities, velocity dispersion of the spheroidal component). Here we discuss the major observations that paved the way for accepting BH-Galaxy co-evolution. For a more extensive review on BH-Galaxy co-evolution see Kormendy and Ho (2013).

Although BHs have been shown not to correlate with some galactic features such as discs and pseudo bulges (Kormendy and Gebhardt 2001; Kormendy et al. 2011) or dark matter (Kormendy and Bender 2011), some correlations are observed between the BH mass (M_{BH}) and bulge properties. Dressler (1989) was the first to propose a correlation between M_{BH} and bulge luminosity (L_{Bulge}). The $M_{BH} - L_{Bulge}$ correlation (see figure 1.3) was then demonstrated by several studies (e.g. Kormendy 1993; Magorrian et al. 1998). Marconi and Hunt (2003) used K-band magnitudes, which minimized internal Galactic absorption and the effect of young stars, to demonstrate a tight $M_{BH} - L_{Bulge}$ correlation with reduced scatter. The $M_{BH} - L_{Bulge}$ correlation, in the K band, is shown in equation 1.19 (Kormendy and Ho 2013).

$$\frac{M_{BH}}{10^9 \, \mathrm{M_\odot}} = 0.544^{+0.067}_{-0.059} \left(\frac{L_{K,bulge}}{10^{11} \mathrm{L_{L_{K,\odot}}}} \right). \tag{1.19}$$

The correlation between M_{BH} and L_{Bulge} motivated a search for a similar correlation with the mass of the bulge (M_{Bulge}). M_{Bulge} has been calculated using different techniques such as the virial theorem (Marconi and Hunt 2003), dynamical modeling (Magorrian et al. 1998; Häring and Rix 2004), as well as scaling relationships implied by fundamental plane parameters (McLure and Dunlop 2002). The different studies show good agreement on $\langle M_{BH}/M_{Bulge} \rangle \sim 0.001$ (e.g. Kormendy and Bender 2009; Marconi and Hunt 2003; Häring and Rix 2004).

BHs also correlate with other properties of their host galaxies, specifically the spheroidal component of the host. The correlation between the BH mass and the velocity dispersion of the spheroidal component ($M_{BH} - \sigma$ correlation, see equation 1.20; Kormendy and Ho 2013) is known to be one of the tightest correlations that BHs have with their hosts. The $M_{BH} - \sigma$ correlation (see figure 1.3; Ferrarese and Merritt 2000; Kormendy et al. 2000; Gebhardt et al. 2000), has had some important implications on the understanding of galaxy evolution: The $M_{BH} - \sigma$ correlation stands as strong evidence that BH growth and bulge formation are closely linked. It also provides an empirical method to estimate M_{BH},

$$\frac{M_{BH}}{10^9 \, \mathrm{M_\odot}} = 0.310^{+0.037}_{-0.033} \left(\frac{\sigma}{200 \mathrm{kms^{-1}}}\right). \tag{1.20}$$
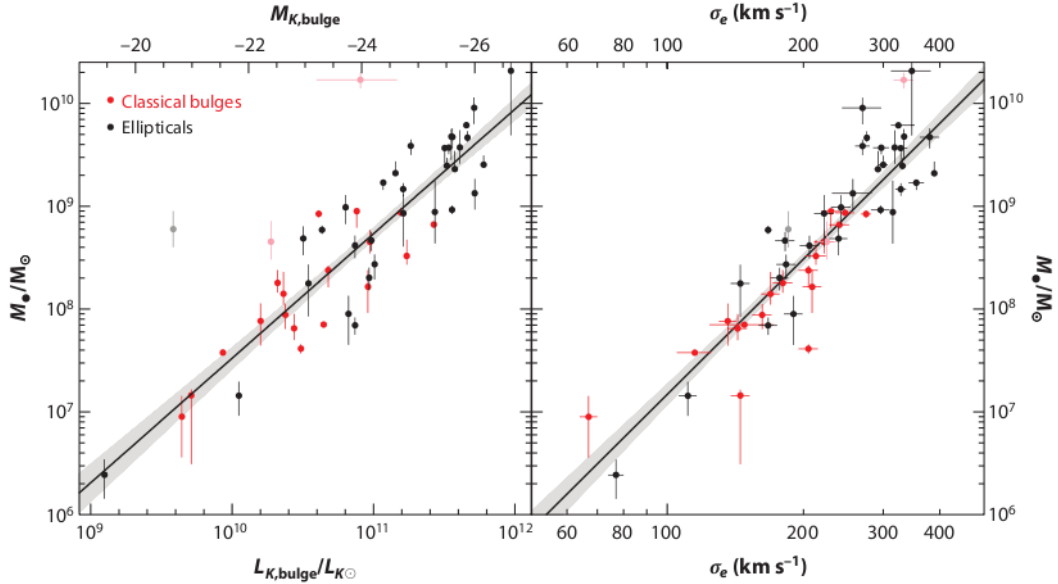
Figure 1.3: The $M_{BH} - L_{K,Bulge}$ correlation (left) and the $M_{BH} - \sigma$ correlation (right). The solid lines show the symmetric (Tremaine et al. 2002) least-squares fit (equations 1.19 and 1.20 respectively) with the gray region representing the 1σ range. (used with the permission of J. Kormendy; Kormendy and Ho 2013)

The Fundamental Plane

The aforementioned correlations between M_{BH} and various properties of the bulge are not the only known correlations. The tightest known correlations are between M_{BH} and effective radius (r_e), effective intensity (I_e), and velocity dispersion (Aller and Richstone 2007; Hopkins et al. 2007a,b; Snyder et al. 2011). Any three of these correlations form what is known as the BH fundamental plane. The tight correlations forming the fundamental plane are a sharp indicator of correlation between M_{BH} and the binding energy of the spheroidal component (Kormendy and Gebhardt 2001).

1.3.3 Active Galactic Nuclei (AGN)

Active Galactic Nuclei (AGN) are among the most luminous observed objects. Observations of AGN extend to the whole electro-magnetic spectrum ranging from X-ray (e.g. Bauer et al. 2004; Gilli et al. 2007), ultraviolet (e.g. Vasudevan and Fabian 2007), optical (e.g. Steidel et al. 2002) to infrared (e.g. Lacy et al. 2004; Hickox et al. 2007). An AGN episode is thought to occur when a large amount of cold gas falls towards the central region of a galaxy to be then accreted by the BH. Such events are triggered by various mechanisms that are grouped into two major categories: secular and external (see Alexander and Hickox 2012 for a review).

Secular mechanisms are triggered by internal structures (e.g. usually galactic bars, substructure transients, disk warps) that give rise to instabilities and drive the gas to the BH. Inflow triggered by secular mechanisms is likely to be weak (e.g. Hopkins et al. 2008) although some studies indicate that secular mechanisms may have been major drivers of AGN activity between $z \sim 2$ and today (Orban de Xivry et al. 2011; Kocevski et al. 2012). Other mechanisms that are thought to trigger major AGN activity are external mechanisms especially major mergers with ratios 3:1 or less (e.g. Dasyra et al. 2006; Woods et al. 2006). Such major mergers can trigger strong inflows of cold gas at high rates to the central galactic region (Hernquist 1989; Barnes and Hernquist 1991; Barnes and Hernquist 1996) causing significant growth in M_{BH}.

1.3.4 AGN Feedback

The observations of the fundamental plane and the other previously mentioned correlations, as well as the need for large amounts of energy to explain downsizing, were vital driving forces behind studying and incorporating AGN feedback in theoretical models. Other evidence has also played a strong role in motivating the study of AGN feedback. The binding energy of a BH $\sim M_{BH}c^2$ significantly surpasses that of the host bulge ($\sim M_{Bulge}\sigma^2$). If small fractions ($\sim 1\%$) of the BH energy couple to the galactic gas they can drive the gas away (Silk and Rees 1998) and heat the remaining gas halting any further accretion or star formation (e.g. Zubovas et al. 2013; Bower et al. 2006). However, this energy could also couple with the gas compressing it and inducing star formation (e.g. Silk and Norman 2009; Ishibashi and Fabian 2012). Also, the observed correlation between AGN and star formation histories provides further motivation for considering AGN feedback. Most star forming systems host an AGN, and AGN systems exhibit signs of recent star formation (Kauffmann et al. 2003; Shi et al. 2009; Hickox et al. 2014). Moreover, both the star formation cosmic history (e.g. Inoue et al. 2013) and the AGN activity history (e.g. Treister and Urry 2012) peak at approximately redshift $z \sim 2$ (see figure 1.4). Simulations provide further support for the effects of AGN feedback, as models with AGN feedback reproduce cosmic star formation histories while those excluding AGN feedback do not (see figure 1.5; Taylor and Kobayashi (2014)). On large scales, there is significant evidence that AGN affect the evolution of the intra-cluster medium. Observations of the hot X-ray gas in clusters indicate the presence of void bubbles that are thought to be caused by AGN jets (McNamara and Nulsen 2007; Fabian 2012). Such jets are ionized and travel relativistically with kinetic energies on the order of $\sim 0.2\%$ the rest mass of a BH (e.g. Nesvadba et al. 2008).

Many mechanisms have been put forward to explain the physics governing the coupling of the energy produced by AGN to the environment such as line radiation pressure (e.g. Castor et al. 1975), radiation pressure affecting dust (e.g. Murray et al. 2005), Compton heating of in-falling gas (e.g. Ciotti and Ostriker 2001), and
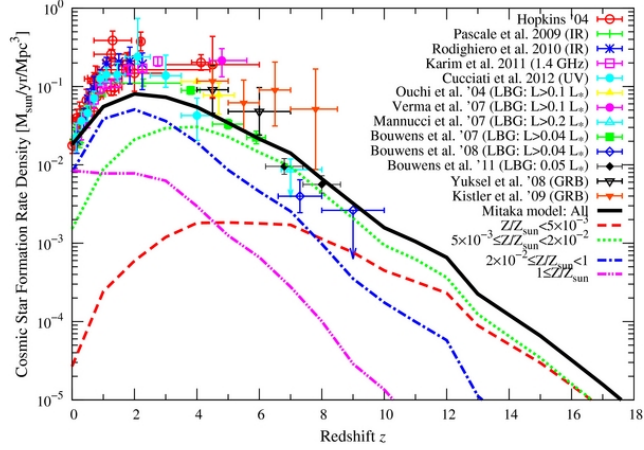
(a)
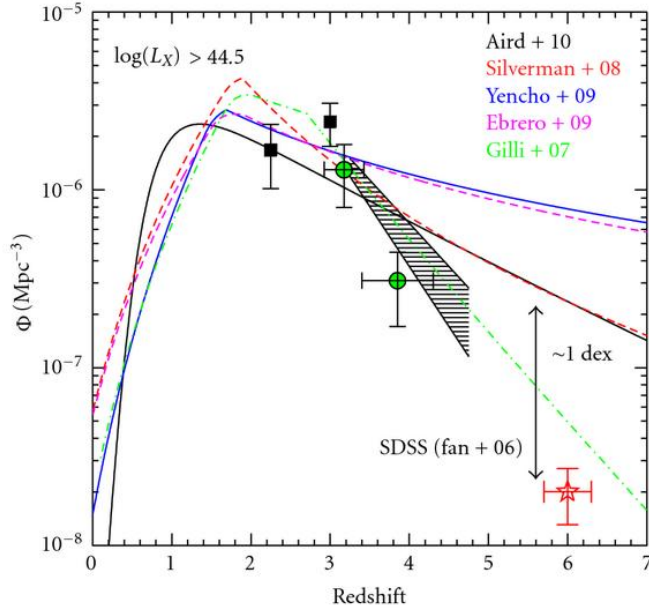
(b)

Figure 1.4: (a) The cosmic star formation history peaking at $z \sim 2$. The solid line shows the Mitaka model, the dotted and dashed lines show the contribution from stars with different metalicities, while the data was compiled from various observations (used with the permission of Y. Inoue; Inoue et al. (2013) and references therein). (b) The cosmic number density of X-ray selected AGN ($L_X > 44.5$ erg.s^{-1}) showing a peak at $z \sim 2$. The lines show different AGN luminosity functions, and the shaded region shows observations of optically bright SDSS QSO (used with the permission of E. Treister; Treister and Urry (2012) and references therein).

photo-ionization pressure (Buff and McCray 1974; Cowie et al. 1978). However, the detailed physics governing the coupling of the energy to the environment remains poorly understood. Given that the details are not clear yet, AGN feedback has been
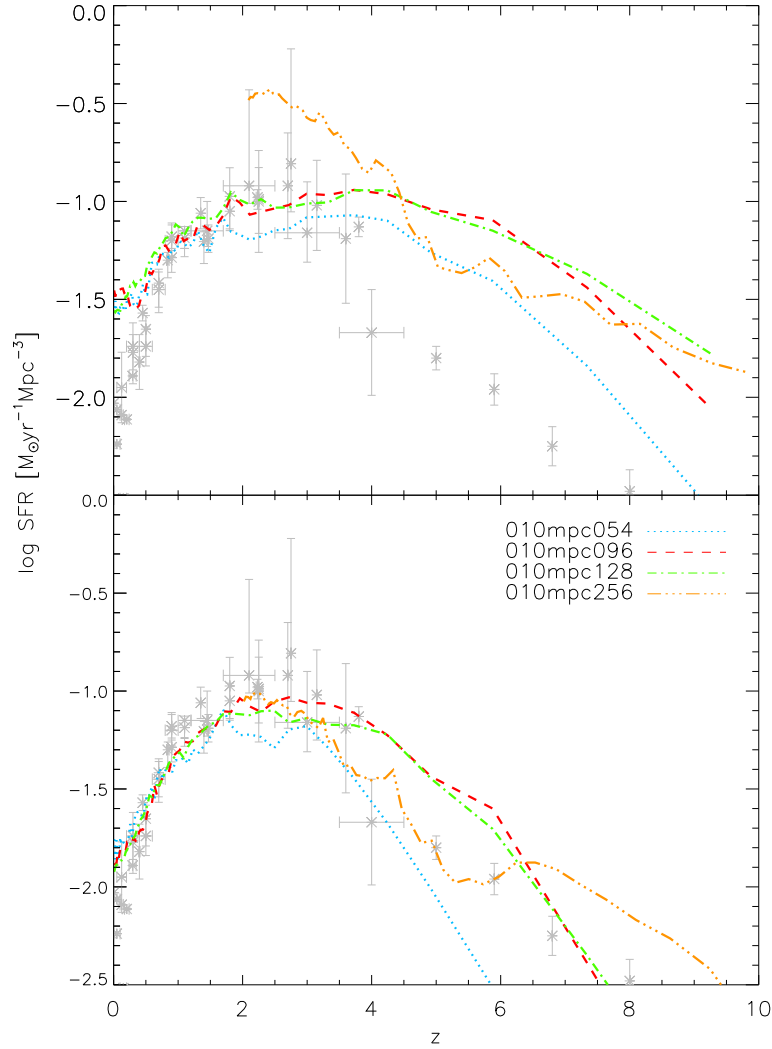
Figure 1.5: Star formation histories of simulations without (top) and with (bottom) AGN feedback. The lines represent simulations of different resolutions while observational data is represented in gray (used with the permission of P. Taylor; Taylor and Kobayashi (2014) and references therein).

categorized into to major forms: (1) radiative (thermal) feedback and (2) kinetic feedback. While physically the mechanisms separate into radiative and kinetic feedback, they impact the galaxy via thermal or kinetic mechanisms.

The radiative mode of feedback, also known as the wind mode or quasar mode, requires high radiative efficiency. The energy is released in the form of a sub-relativistic wind with a wide opening angle. The radius of influence of this

mechanism is low making it more effective in the direct neighborhood of the BH. This mode is likely responsible for correlations with the spheroidal component of the galaxy ($M_{BH} - \sigma$ correlation).

The competing mode of feedback is the kinetic feedback (radio mode). The energy is released in the form of jets launched from the optically thick, geometrically thin accretion disc surrounding the BH (e.g. Rees et al. 1982) during radiatively inefficient accretion. This mode of feedback columnates the gas into jets and drives it away keeping it too hot to be accreted (Fabian 2012).

Theoretical Modeling of AGN Feedback

Various astrophysical phenomena, including galaxy evolution, are impacted by physics on a vast range of scales, although often smaller scales are particularly important. Proper modeling of such phenomena requires several orders of magnitude of spatial resolution. AGN feedback is a vital mechanism in understanding galaxy evolution, and suffers from this problem. While being launched from a small region (BH's radius: $R_{BH} \sim 10^{6-8}$ km, accretion discs $\gtrsim 1000\, R_{BH}$), AGN feedback affects gas on galactic scales ($\sim 3 \times 10^{9-12}\, R_{BH}$), as well as cluster scales ($\sim 3 \times 10^{11-13}\, R_{BH}$). Also, AGN variability is observed on orders of days to years, while the AGN is active for Salpeter (1964) time of $\sim 10^{7-8}$ yr (Martini 2004). Furthermore, AGN feedback impacts regions of discrepant densities: the BH's immediate environment (accretion disc number density $\sim 10^2\, \mathrm{cm}^{-3}$, the narrow-line region electron density $\sim 10^{3-6}\, \mathrm{cm}^{-3}$, and the broad line region electron density $\sim 10^8\, \mathrm{cm}^{-3}$), the interstellar medium with number densities $\sim 10^{2-6}\, \mathrm{cm}^{-3}$, and -sometimes- the intra-cluster medium with particle density $\sim 10^{-3}\, \mathrm{cm}^{-3}$. Therefore, when studying AGN feedback, and its effects on the environment, one must consider the variety of scales that are involved: ~ 13 spatial orders of magnitude, ~ 10 temporal orders of magnitude, and ~ 4 density orders of magnitude. The need for implementing processes that occur on scales below the resolution of the simulation gave rise to the concept of sub-resolution modeling.

Two physical processes that are of particular interest to this study are star formation and AGN feedback. We save a discussion of the detailed implementation of these processes for chapter 3.

1.4   GOAL OF THIS STUDY

This study aims to constrain the implementation (models) of AGN activity (i.e. accretion, feedback) in numerical simulations of isolated disc galaxy mergers. If numerical models were able to *perfectly* model the observed AGN, the predicted Eddington ratio distribution should, in theory, match the observed Schechter-like Eddington ratio distribution and quasar luminosity function (QLF). Therefore, as discussed in chapter 2, the predicted activity function (AF; described in §2) should be in good agreement with the AF inferred from observations, i.e. fitted by a Schechter function (Hopkins and Hernquist 2009). In practice, factors, such as the difficulty of reproducing the ensemble characteristics of observations, make this comparison challenging.

Here, we present the analysis of theoretically predicted AFs of simulated AGN in isolated disc-galaxy mergers; the mergers were simulated using a parallel version (Thacker and Couchman 2006) of HYDRA (see §3.2; Couchman et al. 1995). This work demonstrates the correlation, or lack thereof, between the predicted AFs and some galaxy properties (i.e. M_{BH}, galaxy mass) as well as the effects of different AGN models (different accretion, advection, and feedback models) on the predicted AFs. This study provides some insight into possible approaches to better model AGN in isolated galaxy mergers. However, the reader must be warned that although such simulations provide valuable insight, they may not fully represent the details of mergers or AGN. Being isolated, the simulations do not include the effects of the cosmological environment on the galaxies (see §1.2.1). Moreover, the simulated galaxies are Milky Way-like disc-galaxies with a merger ratio 1:1 which does not represent the populations of all galaxies (i.e. different galaxy types and properties, different gas fraction). Also, the presented galaxy models lack any substructure which

is somewhat unnatural. It is worth noting that the effects of substructure on AGN activity are not yet clear.

In chapter 2 we review important aspects of the AGN phenomenology and introduce the concept of the activity function. We then follow with an introduction of the numerical methods (i.e. SPH, N-body simulations), the models (i.e. BH models, star formation), and the initial conditions used in this study in chapter 3. In chapter 4, we detail the calibrations performed before we introduce the results of this work which are discussed in chapter 5 in the context of the other theoretical and observational studies.

Chapter 2

Theoretical Formalism:
The AGN Activity Function

We first review aspects of the AGN phenomenology that are important to understanding the concept of the activity function.

2.1 AGN Variability

AGN show considerable short-term and long-term variability (as briefly mentioned in section 3.6). Local X-ray observations of the Milky Way, show reflections off of molecular clouds indicating significant short-term variability in the Galactic center ($\sim 10^3 \times$ in brightness over the past ~ 5 centuries; e.g. Ponti et al. (2010); Ryu et al. 2013). Possible long-term AGN variability ($\sim 10^6$ yr) *may* be inferred from gamma ray observations of Galactic Fermi bubbles (e.g. Zubovas et al. 2011; Zubovas and Nayakshin 2012). Further, AGN light echos are observed in some non-active extragalactic objects in the form of large [O III] emitting clouds (e.g. Schawinski et al. 2010), or ultra luminous galaxy-wide narrow line regions excited by intense ($\lesssim 10^5 \times$ brighter) AGN continuum radiation (Schirmer et al. 2013). Also, observations of lobes and cavities in the intra-galactic medium carved by relativistic jets launched by AGN show sporadic activity with timescales on the order of $\sim 10^{4-7}$ yr (e.g. McNamara and Nulsen 2007). Similar lifetimes can be calculated using observations of luminous high redshift quasars (e.g. Jakobsen et al. 2003). The sizes of ionized regions surrounding luminous, high redshift quasars indicate luminous accretion with lifetimes on the order of $\sim 10^{6-7}$ yr.

2.2 Motivations & Implications of the AGN AF

Kauffmann and Heckman (2009) showed that the observed AGN variability is consistent with the observed distribution of Eddington ratios in extra-galactic surveys. Therefore, understanding AGN variability, and properly modeling AGN episodes are necessary when studying AGN feedback: tracking AGN activity provides a powerful test of AGN models (Hopkins and Hernquist 2009). The AGN activity function[1] (AF; Hopkins and Hernquist 2009) tracks the strength and length of AGN episodes independent of the AGN fueling mechanism (Hopkins and Hernquist 2009, 2006; Hopkins et al. 2006a). AGN AFs are best represented as luminosity-dependent distributions (Hopkins et al. 2005a,b; Hopkins and Hernquist 2009), i.e. the time spent above a given luminosity or Eddington ratio, $t(> \lambda)$, or the differential of the amount of time spent above a given luminosity or Eddington ratio, $dt(> \lambda)/d\log\lambda$ (the time spent in a logarithmic luminosity or Eddington ratio bin).

An AGN AF can be paired with a quasar luminosity function (QLF) or Eddington ratio distribution to derive essential information pertaining to AGN evolution (i.e. Eddington ratio distributions, active BH mass functions; Hopkins and Hernquist 2009). The Eddington ratio distribution (Φ) can be related to the duty cycle distribution (δ) and the mass distribution of BHs ($n(BH)$) as follows:

$$\Phi(\lambda|M_{BH}) \equiv \frac{dn(\lambda, M_{BH})}{d\log\lambda} = n(M_{BH})\frac{d\delta}{d\log\lambda}. \tag{2.1}$$

Assuming short AGN variation compared to the Hubble time (t_H) at the redshift of interest, the Eddington ratio distribution at a given luminosity is proportional to the activity function $dt/d\log L$. Therefore, the duty cycle can be expressed in terms of the activity function follows:

$$\frac{d\delta}{d\log\lambda} = \frac{d\delta}{d\log L} \approx \frac{1}{t_H(z)}\frac{dt}{d\log L}. \tag{2.2}$$

---

[1] The concept of AGN activity functions was introduced by Hopkins & Hernquist (2009) as AGN/quasar lifetime.

Combining equations 2.1 and 2.2, one can express the Eddington ratio distribution in terms of the AF modulo a normalization,

$$\Phi(\lambda|M_{BH}) \propto n(M_{BH})\frac{dt}{d\log L}. \tag{2.3}$$

Equation 2.3 indicates a strict correlation between the shape of the Eddington ratio distribution and the AF. Constraining the AF also has direct implications for the evolution of BH mass. Given an AF, the mass of BH that formed at t_{form} is given by:

$$M_{BH}(t) = \int_{t_{form}}^{t} L(t')dt' = \int_{0}^{\log L_{edd}(t)} L'\frac{dt}{d\log L'}d\log L' \tag{2.4}$$

In addition to affecting the QLF, Eddington ratio distribution, and M_{BH}, different AFs will have a distinct impact on the morphology and evolution of a galaxy. Knowing that the AGN feedback power being returned to the galaxy is proportional to the accretion rate, constraining matter accretion will determine the power of the feedback returned to the galaxy. For more details on how feedback can affect a galaxy consult section 1.3.4.

2.3 AF Models & Observational Constraints

There have been various attempts at modeling AGN activity, in turn yielding several AGN light curves and therefore AFs. The produced AFs can be generally approximated as a Schechter function (power-law decay with an exponential cut-off at higher luminosities or Eddington ratios; e.g. Hopkins and Hernquist 2009) given by:

$$\frac{dt}{d\log L} = t_0 \left(\frac{L}{L_{cut}}\right)^{-\alpha} \exp\left(\frac{-L}{L_{cut}}\right), \tag{2.5}$$

where $L_{cut} \equiv \eta L_{Edd}$ with $\eta \sim 1$, and t_0 and α are fitting parameters. The AF can also be expressed as a function of the Eddington ratio, λ:

$$\frac{dt}{d\log \lambda} = t_0 \left(\frac{\lambda}{\eta}\right)^{-\alpha} \exp\left(\frac{-\lambda}{\eta}\right). \tag{2.6}$$

27

The shape of the AF is primarily constrained by the value of the slope α. Different accretion models predict different values for the slope[2], α, and therefore different AFs. These models (shown in figure 2.1) include, but are not limited to, the lognormal model, the light-bulb model, the exponential model, and the Schechter models, as well as combination of the aforementioned models (e.g. Hickox et al. 2014; Hopkins and Hernquist 2009).
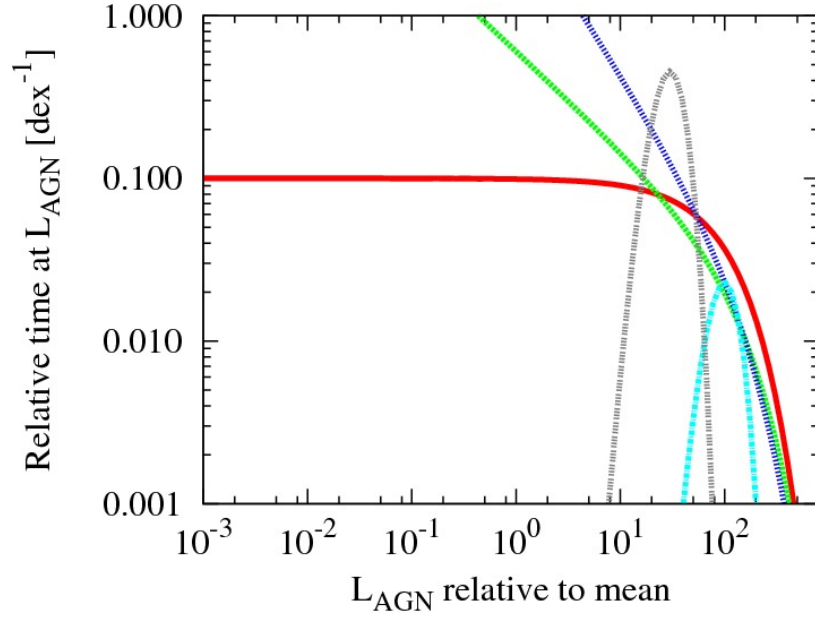
Figure 2.1: A comparison of different activity function (AF) models and observations. The lognormal distribution presented by Kauffmann and Heckman (2009) as a good fit for optically selected, low redshift, passive galaxies is shown as the dashed grey line. The green dashed line shows the observed AF (Shechter model with $\alpha \approx 0.6$; Hopkins and Hernquist 2009). For demonstration purposes, the upper limit for the AFs (Schechter function with $\alpha = 1$; e.g. Soltan 1982; Shankar et al. 2004) is shown as the blue dashed line while the solid red line and the dashed cyan-blue line represent the exponential ($\alpha = 0$) and light-bulb AFs respectively. Different self-regulated models yield AFs that lie between the exponential and upper limit AFs (between the solid red and dashed cyan-blue lines).

i. **Lognormal models:** Kauffmann and Heckman (2009) showed that the distribution of optically selected AGN in low redshift passive galaxies hosting a young stellar population is well described by a lognormal distribution (with width $\sigma \approx 0.4$ dex). Such a distribution corresponds to an AF that can be modeled as

---

[2]Physical/observational constraints limit $\alpha < 1$ (e.g. Soltan 1982; Yu and Tremaine 2002; Shankar et al. 2004)

a Schechter function with $\alpha < 0$. Equivalently, a lognormal distribution given by,

$$\frac{dt}{d\log \lambda_{edd}} = t_0 \exp\left(-\frac{(\log \lambda - \log \lambda_0)^2}{2\sigma^2}\right) \tag{2.7}$$

where σ represents the width of the distribution, λ_0 is the center of the lognormal distribution, and t_0 is a scaling coefficient (Hickox et al. 2014). This distribution is shown as the dashed grey line in figure 2.1.

ii. **Light-bulb models:** In a light-bulb model, the AGN "turns on" for a short time with a given Eddington ratio λ_{on}. The AF is modeled as a Dirac-delta function. If we allow for measurement errors in the accretion rate, the AF can be modeled as a narrow lognormal distribution with $\lambda_0 = \lambda_{on}$ or a Schechter function with $\alpha \ll 0$. Although light-bulb models lack the ability to reproduce the Eddington ratio distribution of moderate luminosity AGN (e.g. Shankar et al. 2013; Hopkins and Hernquist 2009), they have been shown to be effective at reproducing various properties of quasars, e.g., the QLF and quasar clustering (e.g. Shankar et al. 2013; Conroy and White 2013). This distribution is shown as the dashed cyan-blue line in figure 2.1.

iii. **Exponential models:** In such models, accretion is allowed to occur at a constant or exponentially decaying Eddington ratio. The resultant AF is a Schechter function with a flat tail ($\alpha \approx 0$) where the AGN spends equal time in all logarithmic intervals of Eddington ratios with an exponential cutoff near the Eddington limit. Simulations of BH accretion with small scale feedback (e.g. Novak et al. 2011; Gabor and Bournaud 2013) allowing for strong stochastic variations show exponential AFs (Novak et al. 2011). However, the slope of the low luminosity tail is dependent on the gas fraction (Gabor and Bournaud 2013). This distribution is shown as the solid red line in figure 2.1.

iv. **Hybrid power-law and lognormal models:** Some studies used an accretion rate distribution consisting of the sum of a power-law and a lognormal distribution (e.g. Kauffmann and Heckman 2009; Shankar et al. 2013). The predictions

of such a hybrid distribution are similar to those of a pure Schechter function; however they are highly dependent on the relative normalization of the components. This model is omitted from figure 2.1 for clarity purposes.

v. **Schechter models:** In these models the AGN spends consistently more time accreting at lower luminosities. These models produce an AF which is best represented by a Schechter function with $\alpha > 0$. Feedback-regulated (self-regulated) AGN implementations have been shown to yield Eddington ratio distributions that are best fitted by a Schechter function with $\alpha \in [0.3 : 0.8]$ (e.g. Hopkins and Hernquist 2006). Hydrodynamical simulations performed by Hopkins et al. (2006b) reproduce Eddington ratio distributions in the form of a Schechter function with $\alpha \approx 0.6$ which is consistent with current observations (e.g. Hopkins and Hernquist 2009; Ueda et al. 2003). This AF is represented by the dashed green line in figure 2.1. Other models such as the BHs fed by stellar loss (e.g. Ciotti and Ostriker 2007) and disc starvation models (e.g. Yu et al. 2005; Yu and Lu 2008) produce Eddington ratio distribution described by Schechter functions with slopes ranging between $\alpha \approx 0.6$ and the physical maximum $\alpha = 1$. These models are omitted from figure 2.1 for clarity but the resulting AFs lie between the self regulating models' AF (dashed green line) and the physical maximum AF (dashed blue line).

Observational Constraints

Various observations have helped constrain the AGN Eddington ratio distribution, thus inferring the AGN AF and resolving the degeneracy between the proposed models. Observations are in good agreement with the AFs predicted by the self-regulated models. Hopkins and Hernquist (2009) used a variety of observations to rule out simplified models of the AF while showing that the observations are best fitted by a Schecter function with a slope $\alpha \approx 0.6$. Other indirect observations, although suffering from some selection bias and imposing additional assumptions, also favor models where the AGN spends increasingly more time at lower luminosities (the increase in

activity with decreasing Eddington ratios of the Schechter function). AGN cluster-ing analysis shows a weak dependence on luminosity therefore favoring models that spend more time at lower luminosities (e.g. Lidz et al. 2006; Hopkins et al. 2007c). Multi-redshift observations of SMBHs show an evolution in the QLF (e.g. Ueda et al. 2003; Hasinger et al. 2005; Hopkins et al. 2006b) consistent with the predictions of some self-regulated models where the AF is dependent (weakly) on the BH mass and peak luminosity. Other studies show that BH mass functions of luminosity-selected samples include more massive BHs at low luminosities (e.g. Hopkins et al. 2006a,b; Heckman et al. 2004; Greene and Ho 2007) which is consistent with the predictions of feedback-regulated models.

Chapter 3

Numerical Methods & Simulation Details

The long timescales associated with galaxy evolution motivate the need for numerical simulations to help piece together the observed snapshots of galaxies during different evolutionary epochs. Numerical simulations coupled with improved observations helped advance our understanding of the full galactic evolutionary process; although current knowledge is still very incomplete. This chapter details the numerical methods and simulations used in this work.

3.1 A Basic Approach to Galaxy Evolution

The physics of galaxy formation and evolution is governed by hydrodynamics, gravity, chemistry and radiative trasfer. The key processes in galaxy evolution are hydrodynamics and gravitodynamics. Galaxies, and for that matter many other astrophysical processes, are modeled using the following closed system of equations:

- The continuity equation:
$$\frac{\mathrm{D}\rho}{\mathrm{D}t} + \rho \nabla \cdot \boldsymbol{v} = 0 \tag{3.1}$$

- The equation of motion:
$$\frac{\mathrm{D}\boldsymbol{v}}{\mathrm{D}t} = -\frac{1}{\rho}\nabla P - \nabla \phi \tag{3.2}$$

- The conservation of energy equation:
$$\frac{\mathrm{D}u}{\mathrm{D}t} = -\frac{1}{\rho}\left[P\nabla \cdot \boldsymbol{v} + \Gamma - \Lambda\right] \tag{3.3}$$

- An equation of state:
$$P \equiv P(\rho, u) \tag{3.4}$$

- Poisson's Equation:

$$\nabla^2 \phi = 4\pi G \rho \tag{3.5}$$

where $\rho, \boldsymbol{v}, P, \phi, u, \Gamma$, and Λ are the density, velocity, pressure, gravitational potential, specific energy, heating term, and cooling term respectively. The $\frac{\mathrm{D}}{\mathrm{D}t}$ represents the Lagrangian, or comoving derivative:

$$\frac{\mathrm{D}}{\mathrm{D}t} \equiv \frac{\partial}{\partial t} + \boldsymbol{v} \cdot \nabla \tag{3.6}$$

The above system of equations[1] is typically solved by two types of numerical methods: (1) grid methods and (2) particle methods. The latter are often used to simulate dynamical systems of particles (e.g. galaxies) and to study the nonlinear processes of structure formation (see Hockney and Eastwood 1981). Being Lagrangian in nature, particle methods have the advantage begin naturally adaptive because the resolution elements move with the flow as opposed to the fixed Eulerian grid approach where spatially resolving several orders of magnitude is a challenge. However, it is worth noting that in computational simulations the Eulerian approach has proven to be effective in modeling shocks and magnetic fields[2]. There are various approaches within the two main types of methods; however, we will only discuss the approach (see §3.3) implemented in HYDRA (see §3.2; Couchman et al. 1995; Thacker and Couchman 2006).

The aforementioned approach, solving the gravito-hydrodynamic system of equations, is overly simplistic. A more realistic approach to galaxy evolution must also include other vital physical processes such as star formation and stellar feedback (1.2.2) as well AGN feedback (1.3.4). The star formation algorithm and BH models that were used in this work are presented and discussed in sections 3.5 and 3.6 respectively.

---

[1]Can also be written in an Eulerian form and solved on a mesh, while in the Lagrangian form given it lends itself to solution via particle-based methods.

[2]At fixed resolution they are arguable considerably more accurate.

3.2   Hydra

Hydra is a SPH-AP³M code written in FORTRAN77 by Couchman et al. (1995) to simulate cosmological hydrodynamics. It uses smoothed particle hydrodynamics (SPH; see §3.3) to calculate gas properties, and an adaptive particle-particle, particle-mesh (AP³M; see §3.3.3) algorithm to calculate the gravitational forces. This work uses a parallel version of Hydra (Hydra_OMP; Thacker and Couchman 2006) which includes a star formation algorithm (§3.5; Thacker and Couchman 2000) and has been modified to include BHs and AGN feedback (§3.6; Wurster and Thacker 2013a,b).

3.3   Smoothed Particle Hydrodynamics (SPH)

Smoothed particle hydrodynamics (SPH; Lucy 1977; Gingold and Monaghan 1977) is a particle based Lagrangian method (for a review see Monaghan 1992). Being a particle method, SPH approximates the fluid dynamics equations without the need of a grid.

At heart, SPH interpolates a field quantity, $A(\boldsymbol{r})$, defined at a set of points (the particles) to a given point of interest. This interpolation is done using the integral interpolant, $A_I(\boldsymbol{r})$, which is given by:

$$A_I(\boldsymbol{r}) = \int \frac{A(\boldsymbol{r'})}{\rho(\boldsymbol{r'})} W(\boldsymbol{r} - \boldsymbol{r'}, h)\rho(\boldsymbol{r'}) \mathrm{d}^3\boldsymbol{r'}, \qquad (3.7)$$

where W is an interpolating kernel and h is the so-called smoothing length of a particle of density ρ. In numerical simulations, the integral interpolant is approximated by the discrete sum interpolant which is effectively a mass weighted sum over neighboring particles. The sum interpolant may be expressed as:

$$A_S(\boldsymbol{r}) = \sum_j m_j \frac{A_j}{\rho_j} W(\boldsymbol{r} - \boldsymbol{r}_j, h), \qquad (3.8)$$

34

where m_j is the mass of particle j. The subscript j represents quantities at $\boldsymbol{r}_j$ (the position of the jth particle); for example the density ρ_j can be expressed as:

$$\rho_j \equiv \rho(\boldsymbol{r}_j) = \sum_k m_k W(\boldsymbol{r}_j - \boldsymbol{r}_k, h_j), \tag{3.9}$$

where the sum over k is used to avoid confusion with the jth particle subscript.

Derivatives, in SPH, can be calculated using ordinary differentiation as shown below:

$$\nabla A_S(\boldsymbol{r}) = \sum_j m_j \frac{A_j}{\rho_j} \nabla W(\boldsymbol{r} - \boldsymbol{r}_j, h). \tag{3.10}$$

However, this derivative does not vanish for a constant A; therefore, we often use the following form of the derivative that will equal zero if A is constant:

$$\nabla A_S(\boldsymbol{r}) = \frac{1}{\rho} \sum_j m_j (A_j - A_S) \nabla W(\boldsymbol{r} - \boldsymbol{r}_j, h). \tag{3.11}$$

In practice the precise numerical derivative used depends upon a number of issues (see §3.3.2).

Because SPH does not need a grid to calculate spatial derivatives, the equations of energy and momentum become a set of differential equations that are easy to derive and manipulate (see §3.3.2). This is one of the strengths of SPH in modeling structure formation and evolution.

3.3.1   THE INTERPOLATING KERNEL

The basis of SPH is interpolating field quantities from a set of neighboring particles using an interpolating kernel. The interpolating kernel describes the contribution of neighboring particles based on their distance from the particle of interest while the smoothing length, h, represents the characteristic width of the kernel (figure 3.1).

35
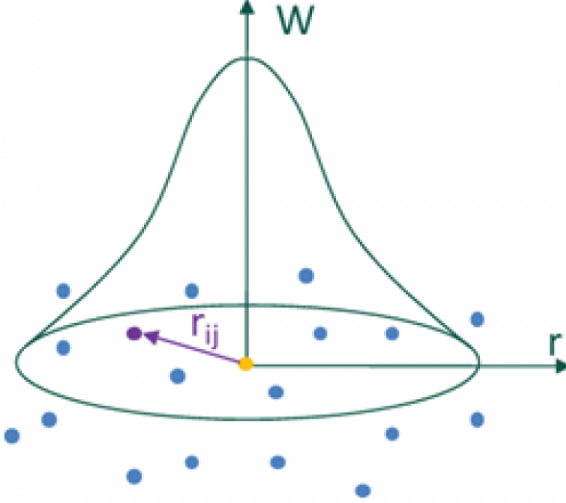
Figure 3.1: A schematic drawing depicting a function expressed in terms of its interpolating kernel (in 2D) smoothed over its neighboring particles (Komoroczi et al. 2013, used with permission of J. Urai and A. Komoroczi) .

Every interpolating kernel must have the following properties:

$$\int W(\boldsymbol{r} - \boldsymbol{r}', h)d^3\boldsymbol{r}' = 1$$

and

$$\lim_{h \to 0} W(\boldsymbol{r} - \boldsymbol{r}', h) = \delta(\boldsymbol{r} - \boldsymbol{r}').$$

(3.12)

Many kernels have been proposed (see Gingold and Monaghan 1982); however, computational efficiency requires a kernel that equals zero at finite distances. HYDRA uses a kernel based on spline functions (Monaghan and Lattanzio 1985), the B_2 spline, viz.

$$W(\boldsymbol{r} - \boldsymbol{r}_j, h) = \frac{\sigma}{4h^\nu} \begin{cases} 4 - 6x^2 + 3x^3 & \text{if } 0 \le x \le 1; \\ (2 - x)^3 & \text{if } 1 \le x \le 2; \\ 0 & \text{otherwise.} \end{cases}$$

(3.13)

where $x = \frac{|\boldsymbol{r} - \boldsymbol{r}_j|}{h}$, ν is the number of dimensions ($\nu = 3$ in HYDRA) and σ is a normalization constant with the values $\frac{2}{3}$, $\frac{10}{7\pi}$, and $\frac{1}{\pi}$ corresponding to one, two and three dimensions respectively ($\sigma = \frac{1}{\pi}$ in HYDRA).

Thomas and Couchman (1992) presented a modified form for the first derivative of the B_2 kernel to prevent artificial clustering by introducing a repulsive force

36

at small distances. The first derivative from Thomas and Couchman (1992) is given by:

$$\nabla W(\boldsymbol{r} - \boldsymbol{r}_j, h) = -\frac{1}{4\pi h^3} \begin{cases} 4 & \text{if } 0 \le x \le \frac{2}{3}; \\ 3(4 - 3x) & \text{if } \frac{2}{3} \le x \le 1; \\ 3(2 - x)^2 & \text{if } 1 \le x \le 2; \\ 0 & \text{otherwise}. \end{cases} \qquad (3.14)$$

Knowing that the width of the interpolating kernel is defined by the smoothing length, it is important to discuss the choice of smoothing length in HYDRA as it defines the region over which quantities are smoothed. HYDRA uses an adaptive smoothing length, h_i, for every particle i such that the particle has $\sim N$ neighbors where $30 < N < 80$ (on average $N \sim 50$). The value of h_i is limited by the simulation volume on the high end and numerical resolution limits on the low end.

Neighbor Particle Definitions

Because SPH calculates field quantities using a set of neighboring particles, it is important to decide on what particles are considered neighbors and therefore will be used when smoothing. The Nearest Neighboring Particle (NNP) method is used to select a particle's neighbors. Different interpretations of the NNP method lead to different understandings of the smoothing length, h, and therefore different approaches to select NNPs (Hernquist and Katz 1989; Shapiro et al. 1996). The two approaches are depicted in figure 3.2.

In the first approach, known as the 'gather' approach, h is considered the radius of the smoothing kernel of a particle t at $\boldsymbol{r}$. Particles, t_b, within the radius $2h$ are considered NNPs of t. In the second approach, known as the 'scatter' approach, h_i is the radius of the smoothing kernel of a particle t_i at $\boldsymbol{r}_i$. Particle t_i is considered as a NNP of t only if $|\boldsymbol{r} - \boldsymbol{r}_i| < 2h_i$. HYDRA uses an explicit 'gather' smoothing kernel.
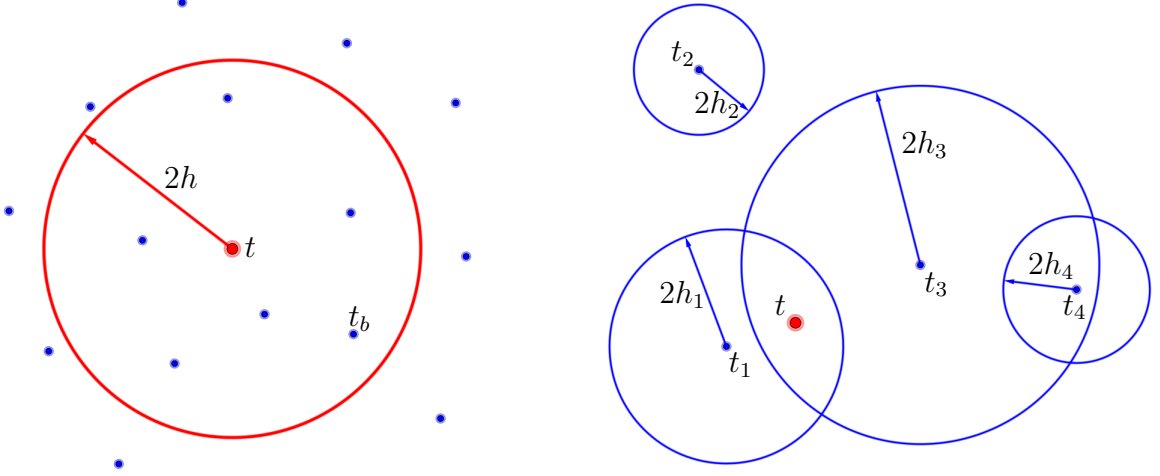
Figure 3.2: A schematic drawing depicting the NNPs for particle t using the two different approaches: the gather approach (left), the scatter approach (right).

3.3.2 SPH INTERPOLATION

As mentioned in section 3.3, the strength of SPH is it's ability to simplify the equations governing galaxy evolution to a series of easily evaluated differential equations. In HYDRA, this is achieved by following Thomas and Couchman (1992) and making use of kernel averaging:

$$W_{ij} \rightarrow \frac{1}{2}[W(\boldsymbol{r}_i - \boldsymbol{r}_j, h_i) + W(\boldsymbol{r}_i - \boldsymbol{r}_j, h_j)], \tag{3.15}$$

and the following approximation:

$$\nabla_i W(\boldsymbol{r}_i - \boldsymbol{r}_j, h_i) \simeq -\nabla_j W(\boldsymbol{r}_i - \boldsymbol{r}_j, h_j). \tag{3.16}$$

Also, because SPH can not naturally model shocks, it is necessary to add a dissipation term to increase the entropy across the shock. The dissipation term is introduced as an artificial viscosity term, Π, which is added to the pressure, P. HYDRA uses the artificial viscosity presented by Thacker and Couchman (2000) based on Monaghan and Gingold (1983).

The SPH interpolation of the continuity equation (3.1) using equations 3.8, 3.9, and 3.11 is:

$$\frac{\mathrm{d}\rho_i}{\mathrm{d}t} = \rho_i \sum_j \frac{m_j}{\rho_j} \boldsymbol{v}_{ij} \cdot \nabla_i W_{ij}, \tag{3.17}$$

where $\boldsymbol{v}_{ij} \equiv \boldsymbol{v}_i - \boldsymbol{v}_j$ and $W_{ij} \equiv W(\boldsymbol{r}_i - \boldsymbol{r}_j, h_i)$. Introducing the viscosity term and ignoring the gravitational acceleration term ($\nabla\phi$) for reasons discussed in 3.3.3, the equation of motion (3.2) and conservation of energy equation (3.3) become

$$\begin{aligned}
\frac{\mathrm{d}\boldsymbol{v}_i}{\mathrm{d}t} = & -\sum_j m_j \left(\frac{P_i}{\rho_i^2} + \frac{\Pi_{ij}}{2} \right) \nabla_i W(\boldsymbol{r}_i - \boldsymbol{r}_j, h_i) \\
& + \sum_j m_j \left(\frac{P_j}{\rho_j^2} + \frac{\Pi_{ji}}{2} \right) \nabla_j W(\boldsymbol{r}_i - \boldsymbol{r}_j, h_j),
\end{aligned} \tag{3.18}$$

and

$$\frac{\mathrm{d}u_i}{\mathrm{d}t} = \sum_j m_j \left(\frac{P_i}{\rho_i^2} + \frac{\Pi_{ij}}{2} \right) \boldsymbol{v}_{ij} \cdot \nabla_i W(\boldsymbol{r}_i - \boldsymbol{r}_j, h_i) \tag{3.19}$$

respectively, where P is the pressure and Π is the artificial viscosity term.

3.3.3 Gravitational Solvers

As discussed in section 3.1, galaxy evolution is a gravito-hydrodynamic problem. SPH is used to solve the hydrodynamics while a separate algorithm is required to evaluate non-local forces such as gravity[3]. Some of the major gravitational solvers are: tree codes (Barnes and Hut 1986) and particle-mesh models (for a detailed review see Hockney and Eastwood 1981). HYDRA uses the Adaptive Particle-Particle, Particle-Mesh (AP³M) model (Couchman 1991).

The AP³M method is a combination of the Particle-Particle (PP) and the Particle-Mesh (PM) methods, and therefore combines both of their advantages. The PP method considers the forces acting on a system from a distance (e.g. gravity, Coulomb force) by directly calculating forces through pairwise interaction (N^2 interactions are considered). While the PM method approaches the forces as field

---

[3]This is the reason we ignored the gravitational forces ($\nabla\phi$) in the SPH equations.

quantities that are then approximated on a mesh. For example, the gravitational potential of the system is constructed over a grid starting from the density field and by solving the associated Poisson equation using fourier methods. Hence, the AP³M method accurately represents close encounters (PP method) and allows rapid calculations of long-range forces (PM method). The adaptive part of the algorithm relates to placing refined meshes in regions where the PP algorithms becomes slow. This feature remedies the slow-down due to clustering in high density regions that the PP method is vulnerable to. Therefore, the AP³M method is computationally efficient and allows high resolution.

Thus, in the AP³M model, the gravitational force is expressed in terms of two components: the short-range force and the long-range force (equation 3.20),

$$\boldsymbol{F}_{grav} = \boldsymbol{F}_{short} + \boldsymbol{F}_{long}. \tag{3.20}$$

The short-range force is calculated using the PP method on refined mesh versions of P³M which considers pairwise interactions between the particle of interest and all other particles within a given radius. However, to compute the long-range force the PM method is used. The adaptive PM accelerations are calculated as follows:

i. Interpolate the particle mass density onto an adaptive grid (i.e. transform the Lagrangian representation to a Eulerian format).

ii. The density grid is Fourier transformed and multiplied by a Green's function.

iii. After transforming back, the resultant potential grid is differentiated to compute the force grid.

iv. The force grid and mass assignment function are then used to calculate the PM acceleration.

v. Repeat (i)-(iv) for all sub-grids

3.4 Hydra Solution Cycle

We present the solution cycle of a single time-step as summarized in Thacker and Couchman (2006), modified to include BHs:

i. Assign mass to the Fourier mesh.

ii. Convolve with the Green's function using the FFT method to get potential. Difference this to recover mesh forces in each dimension.

iii. Apply mesh force and accelerate particles.

iv. Decide where it is more computationally efficient to solve via the further use of Fourier methods as opposed to short-range forces and, if so, place a new sub-mesh (refinement) there.

v. Accumulate the gas force (and state changes) as well as the short-range gravity for all positions not in the sub-meshes.

vi. Repeat (1)-(5) on all sub meshes until forces on all particles in simulation have been accumulated.

vii. Run star formation and cooling routines.

viii. Run BH routines.

ix. Update time-step and repeat.

We note that star and dark matter particles are handled the same way in Hydra.

3.5 Star Formation

As mentioned in section 1.2.2, galaxy evolution depends on how fast the galactic gas reservoir is consumed (i.e. converted into stars). Therefore, calculating the star formation rate (SFR) is key to quantitatively modeling galaxy evolution.

Since star formation occurs on sub-resolution scales relative to scales that can be simulated at present, it is necessary to implement an algorithm that approximates

the effects of star formation at larger scales appropriate for the simulation's resolution. HYDRA uses a "threshold-Schmidt law" star formation algorithm (Thacker and Couchman 2000) where gas is converted to stars if:

i. the gas is dense ($n_H \geq 0.01 \text{cm}^{-3}$),

ii. the gas is cool ($T < 3 \times 10^4 \text{K}$),

iii. baryonic matter is partially self-gravitating ($\rho_{gas} > 0.4\rho_{DM}$),

iv. the flow is convergent ($\nabla \cdot \boldsymbol{v} < 0$).

The SFR ($\dot{M}_\star$) is then calculated using a Lagrangian[4] form of the Schmidt law (Thacker and Couchman 2000; Kennicutt 1998; Katz 1992):

$$\dot{M}_\star = C_{sfr}\rho_g^{1/2}M_g, \tag{3.21}$$

where C_{sfr} is the star formation rate normalization, ρ_g and M_g are the SPH density and mass of the gas. When the mass of the gas to-be-converted reaches $\frac{1}{2}m_g$, a star particle (of mass $\frac{1}{2}m_g$) is formed. The remaining gas is converted to a $\frac{1}{2}m_g$ star particle when the amount of gas to-be-converted to stars reaches 80% of the remaining gas whilst the gas particle is removed.

A complementary part of star formation is stellar feedback which can be in the form of either stellar winds or super-nova (SN) feedback. In HYDRA, feedback is immediately returned to the environment when a star particle is formed. For every $100\,\text{M}_\odot$ of stars formed, one SN event is assumed to occur. Each SN event returns $5 \times 10^{15}e^*$ erg per gram of converted gas to the interstellar medium where the dimensionless parameter $e^* = 0.4$ (Navarro and White 1993). When applying the feedback algorithm, a reduced density is used in the cooling algorithm which makes sure that the feedback energy influences the environment as it does not radiate away

---

[4]Knowing that computational efficiency is a valuable commodity in computational science, the Lagrangian form of the Schmidt law is used as it provides a more efficient approach to calculating the SFR.

quickly (Katz 1992). This reduced density decays back to the local SPH value. The density decay half-life ($t_{1/2} = 5\text{Myr}$) and the value for e^* are the same as those used by Thacker and Couchman (2000) to reproduce the observed Milky Way SFR in simulations of isolated Milky Way-like galaxies.

3.6   BH Models & Algorithms

In this study we use the models described and implemented in Wurster and Thacker (2013a,b). Further details and analysis of the models can be found in Wurster and Thacker (2013a,b), Thacker et al. (2014), and references therein. There are five key components to an AGN feedback algorithm:

 i. The accretion rate on to the BH.

 ii. The SPH particle accretion algorithm.

iii. The energy feedback algorithm.

iv. The BH advection algorithm.

 v. The BH merger algorithm.

Knowing that most of these algorithms account for physics on sub-resolution scales, models (discussed in §3.6.1 through §3.6.7) implement different algorithms to estimate their effects on larger scales appropriate for the simulation resolution. In this section we will first provide an overview of the aforementioned components and then describe the BH models that were used in this study (based on Wurster and Thacker 2013a,b). For a summary of all the models see table 3.1. Note that we follow the same nomenclature as in Wurster and Thacker (2013a,b) where models are named after the authors' initials, subscripts f and l represent fiducial and low resolution runs (see table 3.3) respectively, and lower case suffixes to the parent model name indicates a variant model with the letter signifying the difference.

| Model | Accretion | | | Feedback | | BH Advection | BH Merger |
	Accretion Rate	Particle Accretion	Energy	Model	Distribution		
SDH	$\dot{M}_B(\alpha=100)$	stochastic-unconditional	$\dot{E}=0.005\dot{M}_{BH}c^2$	heating	kernel-weighted	gas particle in r_{inf} with $v_{rel}<0.25c_s$ & $U=U_{min}$	$d<h_{BH}$ & subsonic $v_{\rm rel}$
BS	$\dot{M}_B(\alpha(n_H))$	stochastic-conditional	$\dot{E}=0.015\dot{M}_{BH}c^2$	heating	increments of E_{crit}	gas particle in r_{inf} with $v_{rel}<0.25c_s$ & $U=U_{min}$	$d<h_{BH}$ & $v_{\rm rel}<v_{\rm circ}$
ONB	$\dot{M}_{drag}$	continual-conditional	$\dot{E}=0.1L_{jet}$	halo heating	40 lowest-ρ particles	Δl_{ONB} along stellar ρ gradients	$d<\epsilon_{S2}$ & gravitationally bound
DQM	$\dot{M}_{visc}$	continual-conditional	$\dot{p}=10L/c$	winds	isotropic	tracer mass	$d<h_{BH}$
WT	$\dot{M}_B(\alpha=100)$	continual-conditional	$\dot{E}=0.005\dot{M}_{BH}c^2$	heating	isotropic	Δl_{WT} towards centroid	$d<h_{BH}$ & subsonic $v_{\rm rel}$
PNK	M_{disc}/t_{visc}	continual-unconditional with mass transfer	$\dot{p}=10L/c$	winds	isotropic	Δl_{WT} towards centroid	$d<h_{BH}$ & subsonic $v_{\rm rel}$
HPNK	$\dot{M}_{interp}$	continual-conditional	$\dot{E}=0.005\dot{M}_{BH}c^2$	heating	isotropic	Δl_{WT} towards centroid	$d<h_{BH}$ & subsonic $v_{\rm rel}$

Table 3.1: A summary of the BH models used in this study (Wurster and Thacker 2013a,b). Note, this table does not include the variant models.

Accretion Rates

The accretion rate describes the rate at which the BH mass changes. It is usually modeled as the Bondi accretion rate and it is limited to a maximum of the Eddington rate (see §1.3.1). Note that the radiative efficiency in the Eddington rate (equation 1.16) is set to $\eta = 0.1$ (Shakura and Sunyaev 1973).

Particle Accretion & BH Growth

When modeling BHs in the simulation a distinction can be made between the mass of the BH (sink) particle (the dynamical mass) versus the actual mass used in calculating the accretion rate (the internal mass). This artificial separation has been used in simulations where it is desired to dampen the motion of the BH particle or where finer knowledge of the BH mass is required as compared to the discrete values associated with particles. The internal BH mass (M_{BH}) is updated by discretely integrating the accretion rate as such: $M_{BH} = \dot{M}_{BH} \mathrm{d}t$. While the dynamic BH mass (m_{BH}) is updated by adding the mass of every gas particle that is accreted. Ideally the two masses are equal[5] ($M_{BH} \sim m_{BH}$). Furthermore, every BH is assigned a radius of influence, r_{inf}, which is defined as $r_{inf} \equiv 2 \times \max(h_{BH}, h_{min})$ where h_{BH} is the smoothing length of the BH and h_{min} is the smallest resolved smoothing length. The BH smoothing length is defined such that there exist 60 neighboring gas particles in a sphere of radius $2h_{BH}$. Note that the BH smoothing length corresponds to its neighboring particles as the BH is not treated hydrodynamically. The significance of r_{inf} stems from the fact that only particles within a sphere of radius r_{inf} are eligible for accretion and feedback[6].

When accreting particles onto the BH, both the principles of conservation of mass and angular momentum are invoked where the mass and the momentum of the gas particle are added to the BH mass and momentum respectively. Particle accretion algorithms can be grouped into three major categories:

---

[5]The DQM poses as an exception where the dynamic BH mass is constant.
[6]Note that the ONB model does not return feedback energy locally.

i. Stochastic-unconditional: Neighboring particles are always tested for stochastic accretion.

ii. Stochastic-conditional: Neighboring particles are tested for stochastic accretion if a given criteria of the $m_{BH} - M_{BH}$ relationship is satisfied.

iii. Continual-conditional: Neighboring particles are continually accreted whilst a given criteria of the $m_{BH} - M_{BH}$ relationship is satisfied.

AGN Feedback

As discussed in section 1.3.4, AGN feedback plays an important role in galaxy evolution, primarily massive galaxies. In simulations, while the exact details may be lengthy, AGN feedback is returned to the BH neighborhood[7] as: (1) thermal feedback (increasing the internal energy of gas particles), and/or (2) kinetic feedback (increasing the momentum of gas particles). The feedback energy (E) is calculated using the BH accretion rate (see equation 1.11) such that:

$$E = Ldt = \eta \dot{M}_{BH} c^2 \mathrm{d}t, \qquad (3.22)$$

where $\eta = 0.1$.

BH Advection

Accretion (hence feedback) is highly dependent on the gas properties in the BH's local neighborhood. Therefore, proper tracking of the BH position is essential when modeling AGN activity and is particularly important in the early stages of BH growth. If the BH is of a comparable mass to stellar and gas particles, two body forces can cause significant displacement therefore changing the BH's environment. This can have undesirable (inaccurate) effects on the accretion process. To avoid such artificial inaccuracies, simulations employ advection algorithms[8] to minimize BH motion by

---

[7]Note that the ONB model does not return feedback energy locally.

[8]The DQM poses as an exception where the BH position is updated by assuming it has a large dynamic mass throughout the simulation.

relocating the BH using different methods (i.e. to the core's centroid, along stellar gradients, towards the gas particle with minimal potential energy).

BH Mergers

In this study, we model major galaxy mergers at different mass scales where the final state is a merged galaxy. Under such circumstances, given long enough evolution, it is reasonable to assume that the BHs merge. Of course a general solution to the study of BH mergers is a challenge far beyond modern astrophysics. Models include sub-resolution prescription which allow BHs to merge when a set of criteria is met. Merger criteria are model dependent; they include, but are not limited to, limits on the distance between the BHs (i.e. BHs are within each others smoothing lengths, h_{BH}, or softening length, ϵ_{S2}) and BH velocities (i.e. BHs are gravitationally bound or have subsonic relative velocities). Regardless of the merger criteria, when two BHs merge, their masses (both internal and dynamic) and momenta are added and assigned to one BH while the other is removed from the simulation. The resultant BH is relocated to the centroid of the progenitors.

3.6.1   MODEL: SDH

This model is based on Springel et al. (2005a), hereafter SDH05. The accretion rate is modeled by a modified Bondi accretion rate:

$$\dot{M}_B = \frac{4\alpha\pi G^2 M_{BH}^2 \rho}{(c_s^2 + v_{rel}^2)^{3/2}}, \qquad (3.23)$$

where c_s and ρ are the local sound speed and gas density, v_{rel} is the relative velocity of the BH and the nearby gas, while α is a free parameter which relates the numerical local density and sound speed to their expected (real) values. Following SDH05 and Wurster and Thacker (2013a), α is set to $\alpha = 100$. This large value for α agrees with the argument in Booth and Schaye (2009) that at modest resolutions c_s and ρ are over/underestimated (respectively) by orders of magnitude due to a lack of resolution. The Accretion rate is Eddington-limited such that $\dot{M}_{BH} = \min(\dot{M}_B, \dot{M}_{Edd})$.

47

In this model, the feedback energy is returned to the BH's neighborhood (particles within r_{inf}), weighted by the local SPH kernel, at the following rate:

$$\dot{E}_{feed} = \eta_f \eta_r \dot{M}_B c^2, \tag{3.24}$$

where η_r and η_f are the radiative efficiency ($\eta_r = 10\%$) and the fraction of energy that can couple to gas ($\eta_f = 5\%$) respectively.

The BH growth is controlled by a stochastic-unconditional particle accretion algorithm. Every iteration an accretion probability (p_i) is calculated for each particle (i) such that:

$$p_i = w_i \dot{M}_{BH} \rho^{-1} \mathrm{d}t, \tag{3.25}$$

where w_i is the kernel weight of the gas particle relative to the BH, and $\mathrm{d}t$ is the timestep. Particles are allowed to accrete if $p_i < x_i$ where $x_i \in (0,1)$ is a uniformly distributed random number.

To minimize any unwanted BH motion, an advection algorithm relocates the BH to the neighboring gas particle with the lowest potential energy with $v_{rel} < 0.25c_s$. If the velocity criterion is not met for at least one particle in r_{inf} the BH position is not corrected. The advection algorithm is turned off when the BH dynamical mass (m_{BH}) exceeds $10m_g$; BH advection is then treated by the gravitational solver only.

Finally, the BH merger algorithm contains both velocity and distance restrictions. The BHs are assumed to merge when they are within each other's smoothing lengths and have a relative velocity $v_{rel} < c_s$.

3.6.2 MODEL: BS

This model is based on Booth and Schaye (2009), hereafter BS09, and is similar to the SDH model; however, it was initially implemented in cosmological simulations. The accretion rate, as in the SDH model, is calculated using the Eddington-limited modified Bondi accretion law shown in equation 3.23. In contrast to the SDH model,

α is determined as a function of the local Hydrogen number density (n_H) as follows:

$$\alpha = \begin{cases} 1 & \text{if } n_H < n_H^* \\ \left(\dfrac{n_H}{n_H^*}\right)^\beta & \text{otherwise} \end{cases}, \tag{3.26}$$

where n_H^* is the critical value for the formation of a cold interstellar gas phase, and β is a free parameter. Following BS09, we use $n_H^* = 0.1\text{cm}^{-3}$ and $\beta = 1$. BS09 favor a density-dependent α as the argument for a large α used in SDH05 is inappropriate for low-density regions. This implementation allows higher accretion, and therefore higher feedback, at higher densities.

The feedback efficiency is similar to SDH but is set slightly larger $(\eta_f = 0.15)$. The feedback energy, contrary to the SDH model, is allowed to accumulate until $E_{feed} > E_{crit}$ which is defined as:

$$E_{crit} = \frac{m_g k_B \Delta T}{(\gamma - 1)\mu m_H}, \tag{3.27}$$

where m_g is the mass of a gas particle, and Δ is the incremental increase in temperature of the particle per feedback event. We set $\Delta T = 5 \times 10^6\text{K}$ as in Wurster and Thacker (2013a). When E_{feed} exceeds E_{crit} random neighboring particles (within r_{inf}) receives an energy burst in increments of E_{crit} until $E_{feed} < E_{crit}$.

In this model, the BH growth is determined by a stochastic-conditional particle accretion algorithm. If $M_{BH} < m_{BH}$ the accretion probability is set to $p_i \equiv 0$. Otherwise, similar to the SDH model, an accretion probability is calculated for each neighboring particle (i). The particle is then accreted if $p_i > x_i$. The probability is defined as:

$$p_i = w_i(M_{BH} - m_{BH})\rho^{-1}. \tag{3.28}$$

The BH advection algorithm is the same as that in the SDH model. However, BH mergers are treated differently. BS09 argued that feedback may increase c_s and therefore it may no longer be a suitable velocity scale. This motivates a different

merger algorithm based on the BH distances (within each others' smoothing lengths) and the circular velocity at the more massive BH's smoothing length ($v_{rel} < v_{circ}$).

Lastly, we note that Wurster and Thacker (2013a) introduced a variation of the BS model which uses the BH advection algorithm of the WT model. This model is denoted by a 'w' affixed to the model name: BSw.

3.6.3 Model: ONB

This model was first implemented in cosmological simulations by Okamoto et al. (2008). In this algorithm, the BH is fed by gas inflow caused by the loss of angular momentum due to stellar activity (Umemura 2001). Therefore, an accretion rate is calculated by examining gas clouds in regions of star formation (RSF) neighboring the BH. The accretion rate is modeled using a drag accretion rate:

$$\dot{M}_{drag} = \begin{cases} \eta_{drag} \dfrac{L_{RSF}}{c^2}(1 - e^{-\tau_{RSF}}) & \text{if } \rho_{RSF} \geq \rho_{threshold} \\ 0 & \text{otherwise} \end{cases}, \qquad (3.29)$$

where $\rho_{threshold} = 5 \times 10^{-25} \text{g cm}^{-3}$ is the threshold density, ρ_{RSF} is the gas density in the RSF, $\eta_{drag} = 1$ is the drag efficiency, L_{RSF} is the total bolometric luminosity of the stellar component in the RSF (calculated using look-up tables by PEAGASE2; Fioc and Rocca-Volmerange 1997), and τ_{RSF} is the total optical depth of the RSF. The optical depth, τ_{RSF}, is approximated by:

$$\tau_{RSF} = \frac{3\chi_d}{4\pi} \frac{M_c}{R_{RSF}^2}, \qquad (3.30)$$

where $\chi_d = 50 \text{ cm}^2 \text{ g}^{-1}$ is the mass extinction coefficient, M_c is the total mass of the clouds in the RSF (set to half of the total mass of the gas in the RSF), and R_{RSF} is the radius of the RSF. R_{RSF} is defined as $R_{RSF} \equiv \min(R_{40}, 2h_{min})$ where h_{min} is the minimum smoothing length, and R_{40} is the radius of a sphere centered on the BH and including 40 gas particles.

This model reproduces the radio mode of AGN where the feedback energy is deposited into the halo in the form of jets. The feedback energy, $E_{feed} = \eta_r L_{jet}$, is returned (heating) to the 40 nearest diffused gas particles with $\rho < 0.1\rho_{threshold}$. While the jet luminosity, L_{jet}, is accretion dependent and can be divided into two categories depending on the accretion flow:

$$
\begin{aligned}
L_{jet}^{SD} &\approx 8.1 \times 10^{-5} \dot{M}_{BH} c^2 \quad \text{if } \lambda > \alpha^2, \\
L_{jet}^{RAIF} &\approx 2.6 \times 10^{-1} \dot{M}_{BH} c^2 \quad \text{if } \lambda \leq \alpha^2,
\end{aligned}
\tag{3.31}
$$

where λ is the Eddington ratio, and $\alpha = 0.1$ is the viscosity parameter. The superscripts SD and RAIF represent the accretion flow type: standard accretion disc (optically thick, geometrically thin, radiatively efficient) and radiatively inefficient accretion flow (optically thin, geometrically thick), respectively.

The BH growth is tracked by a continual-conditional particle accretion algorithm where gas particles are allowed to accrete with a probability p_i while $M_{BH} > m_{BH}$. The accretion probability assigned to every gas particle within R_{RSF} is:

$$
p_i = \frac{M_{BH} - m_{BH}}{m_i N_{RSF}},
\tag{3.32}
$$

where m_i is the particle mass and N_{RSF} is the number of gas particles in the RSF.

The BH is advected along the steepest stellar density gradient by

$$
\Delta l_{ONB} = \min(0.1\epsilon_{S2}, 0.03|\boldsymbol{v}|\mathrm{d}t),
\tag{3.33}
$$

where ϵ_{S2} is the gravitational softening length, $|\boldsymbol{v}|$ is the BH velocity, and $\mathrm{d}t$ is the timestep.

Finally, the BH merger algorithm merges the BHs when they are within each other's softening lengths and gravitationally bound.

Wurster and Thacker (2013a) introduced a variation of this model which uses a very conservative search algorithm when calculating the drag accretion rate (small

R_{acc}). This model is denotes as ONBc. Overall, this model can be thought of as having comparatively little feedback.

3.6.4 MODEL: DQM

This model is based on Debuhr et al. (2011), hereafter DQM11. DQM models accretion through the transport of angular momentum (Hopkins and Quataert 2010) and calculates the accretion rate as:

$$\dot{M}_{visc} = 3\pi\delta\Sigma\frac{c_s^2}{\Omega}, \qquad (3.34)$$

where δ is the dimensionless viscosity ($\delta = 0.05$ as per DQM11), Σ is the mean gas surface density, and Ω is the rotational angular velocity of the gas.

The feedback energy is returned kinetically (in the form of momentum) such that all particles within r_{inf} receive an equal radial acceleration. The feedback energy is calculated such that

$$\dot{p} = \tau\frac{L}{c}, \qquad (3.35)$$

where τ is the infrared optical depth ($\tau = 10$ as per DQM11), and L is the Eddington-limited luminosity. It is worth noting that the variant model DQMe (as in DQM11) fixes $r_{inf} \equiv 4\epsilon_{S2}$ while the DQM model (as implemented in Wurster and Thacker 2013a) calculates $r_{inf} = 2\max(h_{BH}, h_{min})$.

To minimize any unwanted BH motion, this model uses a constant tracer mass (only increased via mergers) to represent the BH such that $m_{BH} = 10^9\,M_\odot$. With such a comparatively large dynamic mass, no advection algorithm is needed and any advection is dealt with using the gravitational solver. Note that although this model uses a different dynamic mass, the internal BH mass (M_{BH}) is still initialized to $10^5\,M_\odot$.

This model uses a continual-conditional particle accretion algorithm ($M_{BH} > m_{BH}$). Note that the particles that are removed from the simulations are not added

to the constant dynamic mass. BHs are assumed to merge when they are within each other's r_{inf}. No velocity restrictions are required in this merger algorithm.

3.6.5   MODEL: WT

This model is introduced in Wurster and Thacker (2013a). The accretion is modeled, as in the SDH model, using an Eddington-limited modified Bondi accretion rate with $\alpha = 100$. The feedback energy is equally distributed amongst all particles within r_{inf} applying an isotropic heating to the core.

This model uses an adaptation of the advection algorithm in the ONB model with two major differences. First, the BH is moved towards the center of mass of a sphere of radius r_{inf} centered at the BH. Second, the BH is advected by

$$\Delta l_{WT} = \min(0.10 h_{BH}, 0.3|\boldsymbol{v}|\mathrm{d}t, d_{CM}), \qquad (3.36)$$

where h_{BH} is the BH's smoothing length, and d_{CM} is the distance between the BH and the center of mass. This advection algorithm has several advantages. Moving the BH towards the center of mass includes the stellar component as well as gas and DM unlike the ONB model which only includes stellar gradients. Moreover, using the center of mass of the central sphere prevents coupling the BH to gas particles on the edge of the sphere in case the AGN creates a void.

Particle accretion is treated using a continual-conditional particle accretion algorithm (similar to the ONB and DQM models). The gas particle which is nearest to the BH is accreted while $M_{BH} > m_{BH} + m_g/2$. Choosing the nearest particle to be accreted (instead of a random particle) reduces the random effects in the simulation.

As in the SDH model, the BH merger algorithm includes both distance and velocity criteria. BHs are assumed to merge when they are within each other's smoothing lengths and have a subsonic relative velocity.

For resolution testing purposes, Wurster and Thacker (2013a) introduced the WTh model which is identical to the WT model with the sole different in the smoothing length ($h_{min} \rightarrow h_{min}/2$).

3.6.6 Model: PNK

This model –based on Power et al. (2011), hereafter PNK11– is motivated by some of the major issues with Bondi accretion. Bondi accretion does not account for the angular momentum of gas clouds and therefore allows the instantaneous accretion of rotationally supported particles. On the contrary, a more realistic model should allow the gas to shed its angular momentum before it is accreted; particles accrete onto an accretion disc from which they are then funneled onto the BH. Therefore, the model implements a two-stage accretion process using an accretion disc particle defined as a sink particle including both the central BH and its accretion disc[9] ($M_{ADP} = M_{disc} + M_{BH}$). The smoothing length associated with the ADP is $h_{ADP} = \max(h_{ADP}, h_{min})$ such that a sphere of radius $2h_{ADP}$ includes 60 neighboring particles. First, gas particles within a radius R_{acc} (free parameter) are accreted onto the accretion disc increasing the mass of the disc (M_{disc}) by m_g. The accreted mass then transfers onto the BH with a delay on the order of the disc's viscous time scale t_{visc} (free parameter). When the mass is accreted by the BH, it is removed from the accretion disc and added to the BH mass such that M_{ADP} remains constant. Hence, the Eddington-limited accretion rate onto the BH is defined such that:

$$\dot{M}_{BH} = \min\left(\frac{M_{disc}}{t_{visc}}, \dot{M}_{Edd}\right). \tag{3.37}$$

Knowing that R_{acc} and t_{visc} are free parameters that have defining effects on the models, we follow the same naming convention as in Wurster and Thacker (2013b) in which we incorporate the values of R_{acc} and t_{visc} into the model name as follows: PNK$[100R_{acc}/h_{min}][t_{visc}/\mathrm{Myr}]$. The free parameters, as in Wurster and Thacker (2013b), span the following sets:

  i. $R_{acc}/h_{min} \in \{0.02, 0.05, 0.10\}$

 ii. $t_{visc}/\mathrm{Myr} \in \{1, 5, 10\}$

---

[9]The mass of the accretion disc is initialized to $M_{disc} = 0$.

The growth of the ADP is tracked using a direct accretion algorithm. As explained before, particles within R_{acc} are accreted onto the accretion disc regardless of other gas properties (i.e. velocity). Once a particle is accreted, its mass and momentum are added to those of the ADP.

The original model as described in PNK11 implements feedback by introducing wind particles with radial momenta (Nayakshin and Power 2010). However, such implementation is impractical in our simulations as it can, over time, increase the particle load causing a major slowdown. Therefore, as in Wurster and Thacker (2013b), we use the same feedback prescription used in the DQM model where the feedback is returned in the form of momentum such that all particles within $r_{inf} \equiv 2h_{ADP}$ receives an equal radial acceleration. The feedback rate is given by equation 3.35.

The BH advection algorithm is identical to the one used in the WT model. The ADP is displaced towards the centroid of the sphere centered at the ADP with radius r_{inf}.

Lastly, the BH merger algorithm, as in the WT model, has both distance and velocity restrictions. The ADPs instantly merge when they are within each others smoothing lengths and have a subsonic relative velocity. To conserve mass, the merged BH and accretion disc have the sum of the masses of their progenitors.

3.6.7 MODEL: HPNK

The last BH model we will discuss is the HPNK model. This model was introduced by Hobbs et al. (2012), hereafter HPNK12. We will discuss the implementation of Thacker et al. (2014) in this section. This model aims to overcome some of the defects of the Bondi-Hoyle accretion (i.e. potential due to M_{BH} only). HPNK12 introduce a modified Bondi-Hoyle accretion rate that includes the potential due to the mass enclosed (M_{enc}) within a smoothing radius (fixed to ϵ_{S2}) and the velocity dispersion (σ). This rate is expressed as the interpolating accretion rate:

$$\dot{M}_{interp} = \frac{4\pi\lambda(\Gamma)G^2 M_{enc}^2 \rho_\infty}{(c_\infty^2 + \sigma^2)^{3/2}} \tag{3.38}$$

In a way, our implementation of this model (same as Thacker et al. 2014) can be considered a variant of the WT model. This implementation of the HPNK model uses the same feedback, BH advection and merger algorithms used in the WT model.

3.7   INITIAL CONDITIONS

Galaxy formation and evolution are initial value problems where we start from a set of initial conditions (ICs) and allow the system to evolve under preset physical laws. For the purpose of examining AGN activity in major mergers of Milky Way-like galaxies (this study), we use Milky Way ICs produced by the GALACTICS package (Kuijken and Dubinski 1995; Widrow and Dubinski 2005; Widrow et al. 2008). We then modify these galaxies to include a gas disc, hot gas halo, and a central BH (Wurster and Thacker 2013a; Williamson and Thacker 2012). In this study we follow the same IC generation algorithms used in Wurster and Thacker (2013a). We first provide an overview of the GALACTICS ICs which is followed by a discussion of the associated modifications.

3.7.1   GALACTICS

The GALACTICS package iteratively produces a Milky Way-like galaxy with a stellar bulge, stellar disc, and a DM halo (for a detailed description of the GALACTICS package and the equations presented below see Widrow et al. 2008). The stellar bulge density profile ($\tilde{\rho}_b$) is chosen to reproduce a Sérsic projected density profile; it can be expressed as:

$$\tilde{\rho} = \rho_b \left(\frac{r}{R_e} \right)^{-p} \mathrm{e}^{-b(r/R_e)^{1/n}}, \tag{3.39}$$

where R_e is the radial scale parameter (free parameter), and ρ_b is related to the bulge's gravitational potential (σ_b^2; free parameter) as follows:

$$\sigma_b \equiv \{4\pi n b^{n(p-2)} \Gamma[n(2-p)] R_e^2 \rho_b\}^{1/2}. \tag{3.40}$$

The value of b is chosen such that R_e encloses half the projected mass, or light, whereas p is related to the Sérsic index (n; free parameter): $p = 1 - 0.6097/n + 0.05563/n^2$.

The stellar disc has a density profile analogous to that of the Milky Way. The disc's density profile falls of exponentially in the radial direction and proportional to sech^2 in the vertical direction as such:

$$\rho_{disc}(R, z) \propto \mathrm{sech}^2(z/z_d) \times \mathrm{e}^{-R/R_d}, \tag{3.41}$$

R_d and z_d are the radial and vertical scale heights (free parameters) respectively. For numerical purposes, the stellar disc is truncated at R_{trunc} and z_{trunc} (free parameters). Furthermore, the disc's radial velocity dispersion (σ_R) is expressed as an exponential profile in terms of the central velocity dispersion (σ_{R_0}; free parameter) as follows:

$$\sigma_R^2(R) = \sigma_{R_0}^2 \mathrm{e}^{-R/R_\sigma}. \tag{3.42}$$

For simplicity R_σ is set to $R_\sigma = R_d$.

The DM halo follows the following density profile:

$$\tilde{\rho}_h = \frac{2^{2-\gamma}\sigma_h^2}{4\pi a_h^2} \frac{1}{(r/a_h)^\gamma(1 + r/a_h)^{3-\gamma}} C(r; r_h, \delta r_h), \tag{3.43}$$

with $C(r; r_h, \delta r_h)$ is a truncation function[10]. The free parameters associated with the DM halo profile are: the halo scale length (a_h), the cutoff radius (r_h), the width associated with the truncation function (δr_h), the central cusp strength (γ), and the velocity scale (σ_h).

3.7.2 Modifications to Galactics

As mentioned above, the galaxies produced by Galactics only include stellar (disc and bulge) and DM (halo) components. We modify the Galactics output by including: (1) a gas disc, (2) a hot gas halo, and (3) a super massive central BH. These

---

[10]$C(r; r_h, \delta r_h) = \frac{1}{2}\mathrm{erfc}\left(\frac{r-r_h}{\sqrt{2}\delta r_h}\right) \in [1 : 0]$ for $r \in [r_h - \delta r_h : r_h]$

modifications are described in detail in Wurster and Thacker (2013a) and Williamson and Thacker (2012).

Gas Disc

The gas disc is produced by converting 10 per cent of the stellar disc into gas. The particles are then reflected in the x-y plane to prevent any overlap with stellar particles. The generated disc's scale height is larger than the observationally motivated scale height. However, gas cooling over short timescales (a few 10Myr) allows the gas disc to collapse into a thin disc producing a transient evolution in the gas (i.e. a brief artificial peak in SFR). Another major result of this collapse, although insignificant for this study[11], is a ring-shaped shock which propagates outwards in the disc.

Hot Gas Halo

The hot gas halo, within 40kpc, has a mass equal to 2 per cent of the total disc mass (Rasmussen et al. 2009). This total mass of the gas halo is subtracted from the DM halo to conserve the total halo mass. The hot gas halo, follows the observationally motivated β-profile (e.g. Cavaliere and Fusco-Femiano 1976):

$$\rho_{hgh}(f) = \rho_0 \left[1 + \left(\frac{r}{r_c} \right)^2 \right]^{-\frac{3}{2}\beta}, \tag{3.44}$$

where ρ_0 is the central density, r_c is the core radius (free parameter), and β is the outer slope parameter (free parameter). The temperature profile of an isotropic halo in hydrostatic equilibrium is given by (Kaufmann et al. 2007):

$$T_{hgh}(r) = \frac{\mu m_p}{k_B} \frac{1}{\rho_{hgh}(r)} \int_r^\infty \rho_{hgh}(r) \frac{GM(r)}{r^2} dr, \tag{3.45}$$

---

[11]Williamson and Thacker (2012) demonstrated that this artificial wave dissipates quickly in both our fiducial and low resolution simulations.

where μ is the mean molecular weight, m_p is the mass of a proton, k_B is the Boltzmann constant, and $M(r)$ is the total mass enclosed in a sphere of radius r centered about the galactic center. To prevent the immediate collapse of the hot gas halo, gas particles are given an initial angular momentum, $j_{hgh}(R)$. The angular momentum scales with the circular velocity (v_{circ}) and the distance from the Galactic spin axis (R) as in Moster et al. (2011).

Black Hole

The third, and final modification to the GALACTICS output is the introduction of an SMBH at the center of the galaxy. The BH is defined as a sink particle located at the galaxy's centroid and assigned an internal mass[12] of $10^5\,\mathrm{M_\odot}$ which is consistent with Springel et al. (2005a) and Debuhr et al. (2011). We note that although the mass of the BH is lower than the mass inferred from observations ($M_{BH} \simeq (4.36 \pm 0.42) \times 10^6\,\mathrm{M_\odot}$; Gillessen et al. 2009), the BH grows quickly within a few Salpeter times due to the weak feedback at low M_{BH}.

3.7.3 SCALED GALAXY MODELS

Knowing that we are interested in studying AGN activity in galaxy mergers at different mass scales, it is necessary to devise an efficient way to scale the galaxy models to different masses as opposed to the time-consuming IC generation process. To scale the galaxy models to different masses we follow the prescription outlined in Taranu et al. (2013). Let Γ_m be the mass scale factor (free parameter). Keeping the mass to light ratio constant, and assuming that the Tully-Fisher relationship ($V \propto L^{0.29}$; Courteau et al. 2007) holds, the velocity scale factor is:

$$\Gamma_{\boldsymbol{v}} = \Gamma_m^{0.29}. \qquad (3.46)$$

In order to maintain the virial equilibrium ($R \propto M/\sigma^2$) of the system the distances of particles from the center of the galaxy have to be scaled by the distance

---

[12]A different internal mass is used in simulations testing the effects of the seed BH mass

scale factor:

$$\Gamma_{\boldsymbol{r}} = \frac{\Gamma_m}{\Gamma_{\boldsymbol{v}}^2} = \Gamma_m^{0.42}. \tag{3.47}$$

This scaling in mass and distance implies the following scale factor for density:

$$\Gamma_\rho = \frac{\Gamma_m}{\Gamma_{\boldsymbol{r}}^3} = \Gamma_m^{-0.26}. \tag{3.48}$$

Hydrostatic equilibrium is maintained by scaling the temperature of the hot gas halo. The temperature scale factor can be calculated by scaling equation 3.45:

$$\Gamma_T = \frac{\Gamma_m}{\Gamma_{\boldsymbol{r}}} = \Gamma_m^{0.58}. \tag{3.49}$$

This temperature scaling is consistent with the scaling of the virial temperature ($T_{virial} \propto \sigma^2 \Rightarrow \Gamma_T \propto \Gamma_{\boldsymbol{v}}^2 = \Gamma_m^{0.58}$). Note that Taranu et al. (2013) do not include a temperature scaling as their models are generated by GALACTICS and therefore do not include a gas component.

For example, scaling a galaxy by a mass scale factor of $\Gamma_m = 0.10$ (10% scaling) implies a distance scale factor of $\Gamma_{\boldsymbol{r}} = 0.38$ and therefore a density scale factor of $\Gamma_\rho = 1.82$. The velocities and temperatures should also be scaled by $\Gamma_{\boldsymbol{v}} = 0.51$ and $\Gamma_T = 0.26$ respectively.

3.8   OVERVIEW OF SIMULATED MODELS

We have used previous work (Wurster and Thacker 2013a,b; Thacker et al. 2014) and run new simulations using all the BH models[13] described in section 3.6 at both fiducial and low resolution. Each simulation[14] is evolved for 1.5 Gyr and consists of two identical Milky Way-like galaxies initially separated by 70 kpc. The galaxies are initialized on parabolic trajectories with respect to each other (e.g. Springel et al.

---

[13]The low mass (mass-scaled) galaxies were simulated using only the PNK and WT models

[14]The fiducial resolution ONB model was evolved for 1.2 Gyr. Due to the non-local feedback prescription in the ONB model, a dense galactic core formed around the BH resulting in a significantly larger wall-clock time per step. The fiducial resolution, low mass models were also evolved for 1.2 Gyr due to time constraints.

Galaxy Component	Parameter	Value
Stellar Bulge[†]	σ_{b}	292 km s^{-1}
	R_{e}	0.7 kpc
	n	1.1
Stellar Disc[†]	R_{d}	2.46 kpc
	z_{d}	0.49 kpc
	R_{trunc}	30 kpc
	z_{trunc}	1 kpc
	σ_{R0}	119 km s^{-1}
Dark Matter Halo[†]	a_{h}	13.6 kpc
	r_{h}	275 kpc
	δr_{h}	25 kpc
	σ_{h}	330 km s^{-1}
	γ	0.81
Hot Gas Halo[‡]	r_c	1.75 kpc
	β	2/3
	μ	0.6
Galaxy Scaling[‡]	Γ_m	0.1 or 1.0

Table 3.2: The free parameters used to produce Milky Way-like galaxy models.
† denotes parameters used in GALACTICS such that the associated components' masses are consistent with Springel et al. (2005a); see §3.7.1.
‡ denotes parameters that were used when modifying the GALACTICS output (Moster et al. 2011; Kaufmann et al. 2007); see §3.7.2 and §3.7.3.

2005a). Each galaxy has a total mass of $9.60 \times 10^{11}\,\mathrm{M_{\odot}}$ ($9.60 \times 10^{10}\,\mathrm{M_{\odot}}$ for the low mass models) divided amongst 1,287,743 (168,351) particles in the fiducial (low) resolution simulations. For a detailed component breakdown of each galaxy consult table 3.3. A Plummer softening length of 120 pc (300 pc) is used in the fiducial (low) resolution simulations. Note that when the galaxies are scaled by mass the number of particles remains constant. However, the Plummer softening length is scaled by the distance scaling factor (see §3.7.3). The free parameters used to generate the ICs along with their their associated values are shown in table 3.2.

		Fiducial Resolution		Low Resolution	
	Total Mass $(10^{10}\,\mathrm{M}_\odot^\ddagger)$	Particle Mass $(10^{5}\,\mathrm{M}_\odot^\ddagger)$	Number of particles	Particle Mass $(10^{5}\,\mathrm{M}_\odot^\ddagger)$	Number of particles
Dark Matter Halo	89.92	11.75	765 000	89.92	100 000
Hot Gas Halo	0.60	0.36	165 343	2.77	21 619
Stellar Bulge	1.34	2.37	56 649	18.10	7 407
Stellar Disk	3.56	2.37	150 375	18.10	19 662
Gas Disk	0.54	0.36	150 375	2.77	19 662
Black Hole†	10^{-5}	1.00	1	1.00	1

Table 3.3: A component break down of each a galaxy at the fiducial and low resolution.
$\ddagger$: The mass unit for the low mass galaxies is 0.1 times the listed units.
$\dagger$: A different seed M_{BH} was used in some simulations.

3.9 ACTIVITY FUNCTION CALCULATIONS

We are particularly interested in studying AGN activity by tracking the AGN activity function. The activity function is calculated differentiating the time spent above a given Eddington ratio $(t(> \lambda))$:

$$\text{AF} = \frac{\mathrm{d}}{\mathrm{d}\lambda} \left(t(> \lambda) \right) . \tag{3.50}$$

To minimize the artificial effects due to stabilization of the initial transients of the ICs, and restrict the focus on the merger and post merger epochs, we limit our analysis to times later than $600\,\text{Myr}$.

At every iteration (i), the BH accretion rate $(\dot{M}^i_{BH})$ and the Eddington rate $(\dot{M}^i_{Edd})$ are calculated. The Eddington ratio (λ^i) is then calculated as follows:

$$\lambda^i = \frac{L^i}{L^i_{Edd}} = \frac{\dot{M}^i_{BH}}{\dot{M}^i_{Edd}} . \tag{3.51}$$

The time spent at a given iteration is assumed to be the timestep (δt^i) at the iteration. Hence, the time spent above a given Eddington ratio is:

$$t(> \lambda) = \sum_i \left[\delta t^i \cdot \mathcal{H}(\lambda^i - \lambda) \right] , \tag{3.52}$$

where $\mathcal{H}$ is the Heaviside step function.

Chapter 4

Simulation Results & Discussion

The main purpose of this work is to constrain the predictions of simulated BH models with observationally implied results as a means to help understand the shortcomings of the current generation of models. We study AGN activity in major merger simulations using different BH models and initial conditions (ICs). This chapter presents the results of the simulations used in this study.

4.1 Simulation Calibration

Before we present the simulation results it is important to test the sensitivity of the results to various factors such as minor variations in the ICs, and other numerical artifacts. All BH models, ICs, and the star formation algorithms have already been comparatively well tested and calibrated by Wurster and Thacker (2013a,b), Williamson and Thacker (2012), and Thacker and Couchman (2000), respectively. However, in this section we further test the sensitivity of our models to run-to-run variations, random number generation effects, as well as differences in the ICs (e.g. rotational orientation). It is important that different runs of the same ICs, or ICs with different initial random seeds for the particle distributions, do not cause significant differences in the results. In other words, constraining artificial/numerical variations will yield a limit, analogous to experimental uncertainty, within which the results are robust. The calibrations were done for models WT_l and $PNK0505_l$ due to the limited time and computational resources available. Tests using low resolution simulations provide a good first order comparison of the models and also amplify the impact of run-to-run variations due to the increased discreteness of the low resolution models.

4.1.1 Run-to-Run Variations

We first examine the differences in the results among different runs of the same simulation. The differences probed by this test are due to numerical effects (mainly floating point arithmetic effects, i.e., truncation, rounding errors) introduced by running in parallel. Because calculations are distributed across processors differently from run to run, we can get different rounding errors. The runs were performed on different nodes (16 cores each) using the same BH models (WT and PNK0505) and ICs. Figures 4.1 and 4.2 show a comparison of the BH accretion rates[1], SFR, BH mass, and the resultant activity function between different runs using the two different models. Different runs (using the same models and ICs) produce similar results: The four runs using the WT model yield BH masses, SFRs, and accretion rates that deviate from the average by a maximum of 5%, 92%, and 43% after 1.5 Gyr respectively. The PNK0505$_l$ runs produce final BH masses, SFRs, and accretion rates that deviate from the average by a maximum of 3%, 69%, and 30% respectively. The intermediate BH mass and SFR deviate within less than 80% from the average. Note that the high deviations in the SFR in the final states are exaggerated because of the low SFRs after the merger.

On the other hand, the activity functions show some differences, primarily in that they extend to lower Eddington ratios and have more power at lower Eddington ratios. At low λ the BH is accreting at low rates and is consequently more impacted by differences between simulations. So we should anticipate differences in this regime. The low λ tail in the PNK runs deviates for $\lambda < 2 \times 10^{-3}$ (different slopes) and has a cut-off that ranges between $\lambda \sim 5 \times 10^{-5}$ and $\lambda \sim 5 \times 10^{-4}$. In the case of the PNK model, the flat tail of the activity function is governed by the decay rate of mass from the accretion disc to the BH. Variation at low Eddington ratios is inevitable because of the low number of particles contributing to the local density around the BH.

---

[1]Note that all plots of the BH accretion rate and SFR show the associated quantities averaged over bins of 10 Myr.

The central dip in the WT model varies between $\lambda \sim 4 \times 10^{-3}$ and $\lambda \sim 10^{-2}$, while the low λ cutoff ranges from $\lambda \sim 10^{-4}$ to $\lambda \sim 3 \times 10^{-4}$. The high λ peaks (WT: $\lambda > 2 \times 10^{-2}$; PNK: $\lambda > 2 \times 10^{-3}$) are in good agreement for both models. Overall, although there are some differences, all activity functions, for a given model, are qualitatively similar and differ precisely where numerical resolution is expected to be an issue.
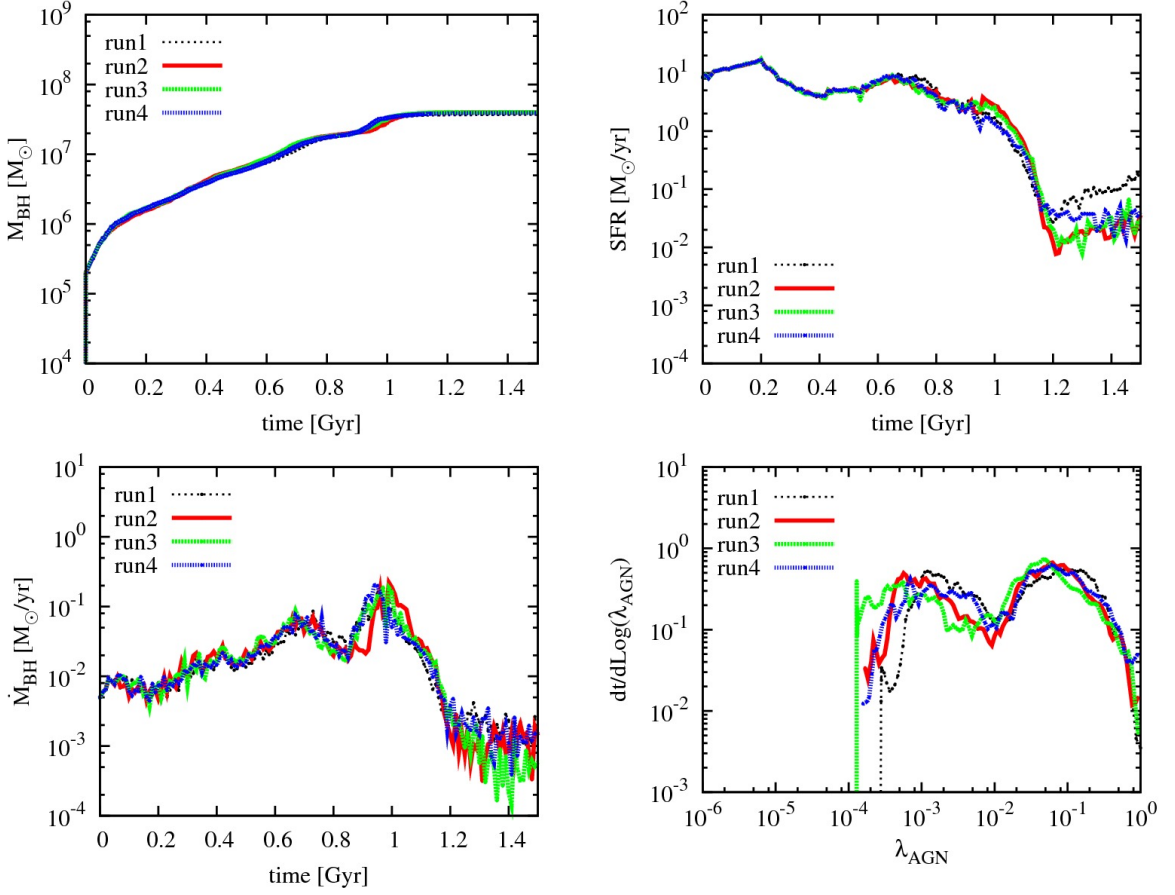
Figure 4.1: A comparison between four low resolution runs (denoted by different colors) using the WT model. The sub-figures show the total BH mass (sum of the two BH masses), total SFR, total BH accretion rate, and the activity function throughout the simulation. Different runs show -expected- similar results.
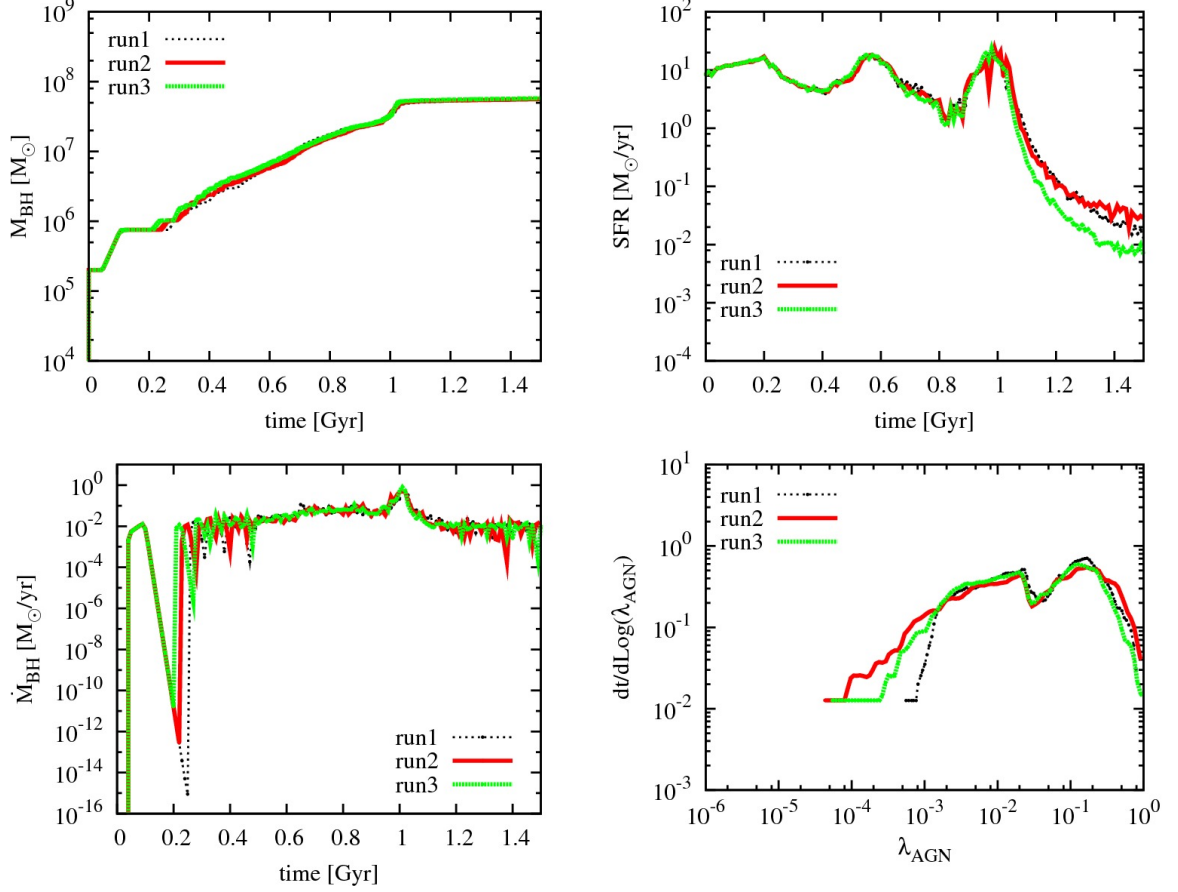
Figure 4.2: A comparison between three low resolution runs (denoted by different colors) using the PNK model. The different colors denote different runs. The sub-figures, in clockwise order, show the total BH mass (sum of the two BH masses), total SFR, activity function, and the total BH accretion rate throughout the simulation respectively. Different runs show -expected-similar results.

4.1.2 IC SEED

The motivation of this section is to check whether small differences in the initial conditions (mainly due to random number generators or numerical artifacts such as truncation errors) yield significant differences in the final results. Here we test the effects of different random seeds in the IC generator, which determines the placement of particles, on the final results. The low resolution test simulations used the PNK0505 model; their results are shown in figure 4.3. Note that differences due to initial seeds

are exaggerated at lower resolutions because of the increased discreteness. The final BH mass, SFR, and accretion rate vary from their average within a maximum of 5%, 93%, and 69% respectively. These values are broadly similar to the run-to-run variations.

Figure 4.3: A comparison between four different low resolution simulations (denoted by the different colors) using the PNK0505 model starting from ICs with different random number seeds. The sub-figures, in clockwise order, show the total BH mass (sum of the two BH masses), total SFR, activity function, and the total BH accretion rate throughout the simulation respectively. Changing the random seed did not affect the final BH mass (5% variation) however it had visible effects on the SFR (93% variation), accretion rate (69% variation) and the intermediate BH mass. The low λ tail and cut-off of the activity function were somewhat different between the simulations. These differences should be taken into considerations when comparing simulations with different ICs.

It is also worth noting that there are some obvious differences in the intermediate accretion rate as well as the SFR and intermediate BH mass during the simulation. On the other hand, the activity functions produced by the different simulations are in close agreement for $\lambda > 2 \times 10^{-3}$ contrary to the low λ tail which is affected by the mass transfer from the accretion disc onto the BH and the frequency of particle accretion, and therefore the stochasticity of the BH's environment. However, the low λ tail is not very well predicted for different seeds as the tail's slope and cut-off for $\lambda < 2 \times 10^{-3}$ shows differences. These variations provide an uncertainty within which data from simulations with different ICs is considered to be in agreement. This also highlights the challenge of having agreement between the intermediate evolution of different systems due to the chaotic nature of accretion of small increments of mass. Similar results are expected in the activity functions of simulations with different IC seeds using the WT model (see run-to-run variations). The activity functions are expected to agree for $\lambda > 2 \times 10^{-3}$ with some discrepancy in the low luminosity cut-off $(\lambda < 10^{-3})$ due to the increased discreteness.

4.1.3 BH Seed Mass

Once the various feedback and star formation algorithms are set, galaxy evolution is considered an initial value problem. Therefore understanding the effects of variations in the initial conditions is necessary. Moreover, when studying galaxy evolution and mass accretion onto black holes, one must understand the effects feedback can have on the galaxy and the simulations' final output. Therefore, examining the effects of the initial BH mass on the simulation reveals valuable information about the feedback mechanism and the comparative stability, or instability, of the galactic system against feedback. In fact this presents a test of how well the models (physics) can predict the final BH mass as a function of the seed mass, and is clearly a test of the physics rather than just numerical effects. Note that changing the BH seed mass effectively changes the simulated system therefore we might not necessarily expect the same results (e.g.

69

AF, SFR, BH mass). Figure 4.4 shows different low resolution simulations using the WT[2] model and starting from the same ICs with a different BH seed mass.

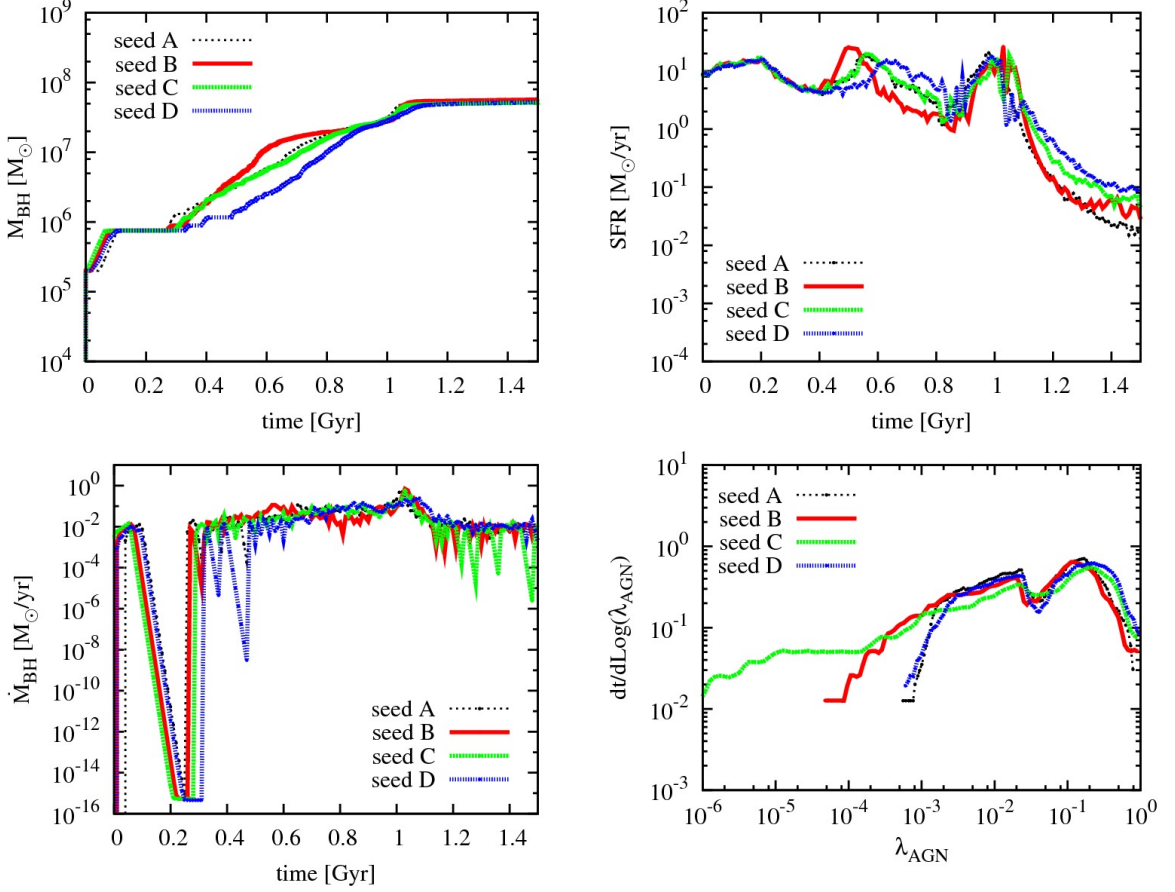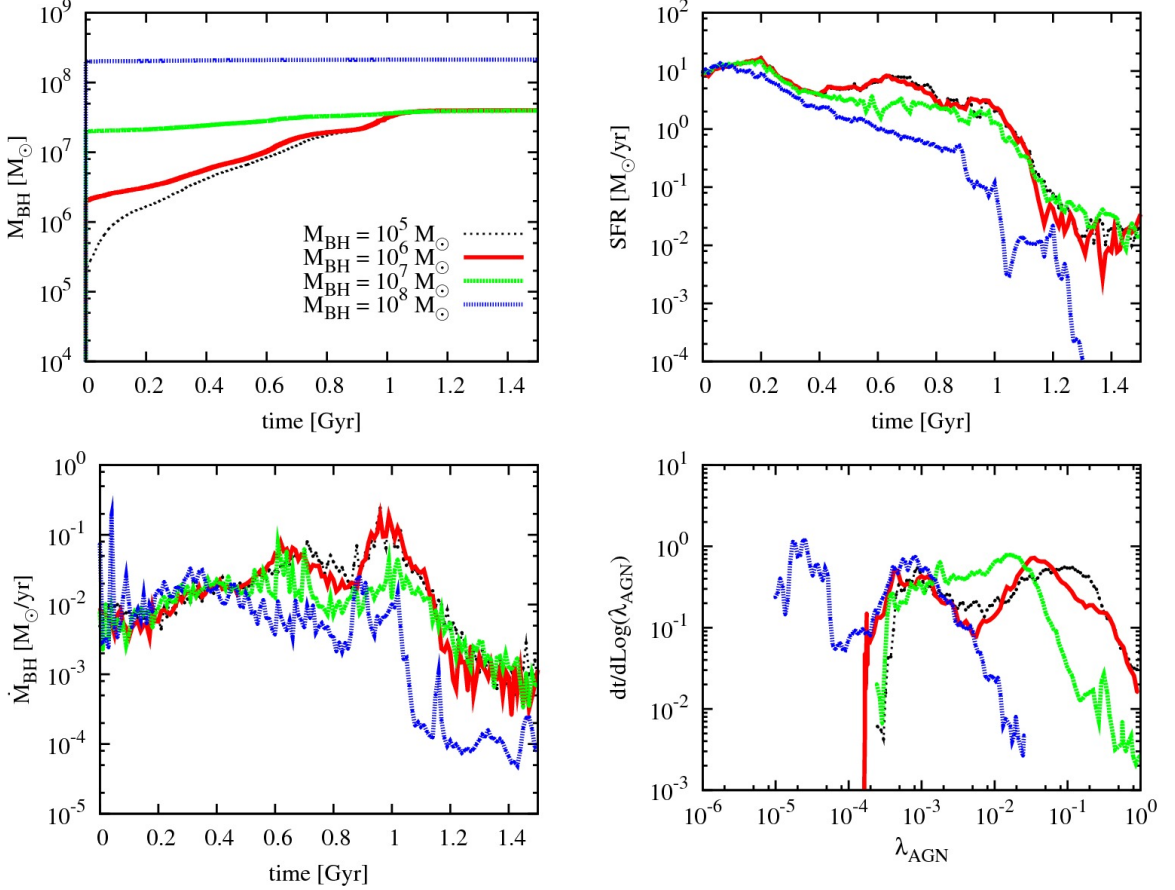**Figure 4.4:** A comparison between four different low resolution simulations (denoted by the different colors) using the WT model starting with the same ICs but with a different BH seed mass. The sub-figures, in clockwise order, show the total BH mass (sum of the two BH masses), total SFR, activity function, and the total BH accretion rate throughout the simulation respectively. With the exception of the simulation with an initial BH mass $M_{BH} = 10^8 \, \mathrm{M_\odot}$, which exhibits violent feedback therefore hindering the BH's growth and leading to a lower SFR and accretion rate, changing the BH seed mass did not significantly influence the final BH mass or SFR; the BH mass and SFR converged to values that agree within less than a factor of two. The activity functions show some differences (high λ peak, low λ tail) but still exhibit a wide lognormal shape.

The simulation with BH seed mass $M_{BH} = 10^8 \, \mathrm{M_\odot}$ exhibits violent feedback which reduces the SFR as well as the accretion rate onto the BH thus hindering the growth of the BH and leading to vastly different morphologies. The BH in the

---

[2]We limit our analysis to the WT model because of its superior ability to model BH properties and the time constraints of this study.

simulation is also well beyond the $M - \sigma$ relationship which is unrealistic. Therefore we will ignore this simulation in our comparison. For the simulations with a seed BH mass $M_{BH} \in \{10^5, 10^6, 10^7\}\,\mathrm{M_\odot}$, the feedback mechanism self regulates the system leading to similar properties at the end of the simulations: The final BH mass, SFR, and BH mass accretion rate deviate from their average by a maximum of 1.5%, 37%, and 27% respectively. Note that the models, although differing in their ICs, produce similar final BH masses with little deviation.

On the other hand, the simulations with BH mass $M_{BH} < 10^7\,\mathrm{M_\odot}$ have activity functions with similar features showing trends consistent with AGN feedback: Using a higher BH seed mass, causes a shift in the high λ peak of the activity function to lower Eddington ratios. This expected shift is consistent with AGN feedback being more aggressive for higher BH masses, therefore forcing an approximate equilibrium in terms of the local density (accretion rate) and feedback at lower densities. The peaks for the simulations with BH seed mass $M_{BH} = 10^5, 10^6, 10^7$ and $10^8\,\mathrm{M_\odot}$ are at $\lambda \sim 10^{-1}, 4 \times 10^{-2}, 1.5 \times 10^{-3}$ and 7×10^{-4} respectively. Also, we observe a shift in the low λ cut-off of the activity function to lower Eddington ratios ($M_{BH} = 10^{6,8}\,\mathrm{M_\odot}$) or a significant increase in the amount of time spent at moderate Eddington ratios ($M_{BH} = 10^7\,\mathrm{M_\odot}$). Although different BH seed masses yield similar final BH mass, the produced activity functions are expectedly different.

4.1.4 Initial Galactic Rotational Orientation

The galaxies modeled in this study are all set on parabolic paths with their gas component's angular momentum aligned with the dark matter's angular momentum (i.e. both gas and dark matter components rotate in the same direction; which we denote PP for prograde-prograde). In this section we examine the effects of changing the rotational velocity of the gas component on the final system. Changes in the rotational velocity of the gas component manifest as changes in the total angular momentum of the remnant gas and therefore changes in the accretion rate as gas becomes more prone to gravitational collapse.

Figure 4.5 shows a comparison between simulations with different rotational orientations for the gas component using both the WT and PNK models. Changing the rotational orientation of the gas component (both galaxies have retrograde gas rotational velocities; RR) allowed earlier growth in the BH mass in the PNK model due to the delayed feedback while the WT model's feedback implementation regulates the system on time-step scales. The peak in accretion at $\sim 0.06\,\mathrm{Gyr}$ ($\sim 0.15\,\mathrm{Gyr}$) in the PNK0505$_\mathrm{l}$ (WT$_\mathrm{l}$) model induces a significant burst of feedback which drives the accretion to low values therefore causing the initial deviation in the intermediate BH mass. The feedback burst is more effective in the PNK model compared to the WT model: The PNK model implements kinetic feedback which is efficient at creating a long lasting void around the BH (low densities) as opposed to the thermal feedback in the WT model which can drive outflows (Wurster and Thacker 2013a). This causes the BH growth in the PNK0505 model to be delayed further as well as causing the SFR to drop sharply at later times as compared to the gradual decrease in the WT model. Another burst in accretion occurs at the time of the core merger ($t \sim 1.0\,\mathrm{Gyr}$). The feedback associated with this burst in accretion blows the gas away in the PNK model sharply halting any further accretion and star formation, while the WT model's, less effective, feedback heats the surrounding gas causing a gradual drop in the gas density in the BH's neighborhood and therefore gradually halts accretion and reduces star formation.

The results of the simulation where only one galaxy's gas component is in retrograde rotation (PR) are less different than those of the RR simulation when compared to the PP run. Nonetheless, despite the aforementioned differences, all three simulations are within 27% and 8% for the final BH mass for the WT and PNK models respectively. Note that larger differences are observed in the intermediate BH mass for reasons already discussed. The final SFR varies within 25% of the average in the WT model while the SFR in the PNK model varies by $\sim 60\%$ from the average. Because of the low SFR values, larger differences are expected.

Figure 4.5: A comparison between six low resolution simulations (denoted by the different colors) using the WT$_l$ and PNK0505$_l$ model and starting from the ICs only differing in their gas rotational velocity direction. The left (right) column shows the simulations using the WT$_l$ (PNK0505$_l$) model. The different rows show (top to bottom) show the total BH mass (sum of the two BH masses), and the total SFR, and the accretion rate respectively. Changing the direction of the gas's rotation had a significant impact on the instantaneous BH mass and SFR which is attributed to the difference in the angular momentum in the merger's remnant.

73

The activity function of each of the simulations is shown in figure 4.6. Changing the gas's rotational orientation does not significantly affect the activity function (within run-to-run variations) in the WT model: The episodes of high accretion rates are associated with feedback bursts that push the low accretion cut-off to lower Eddington ratios with an increase in the time spent at the Eddington luminosity ($\lambda \sim 1$).

However, the activity functions produced by the PNK model are significantly different. The RR activity curve shows a strong peak at high Eddington ratios ($\lambda \sim 1$) which is consistent with the gas having less angular momentum and therefore collapsing and allowing high accretion rates. The high accretion rates are associated with powerful feedback that halts further accretion. However, the accreted mass onto the ADP can still transfer onto the BH giving rise to a long lasting flat low λ tail. On the other hand, the PP and PR activity curves are in agreement with minor differences in the PR's low λ tail which is governed by the mass transfer from the accretion disc onto the BH and the frequency of particle accretion onto the ADP.
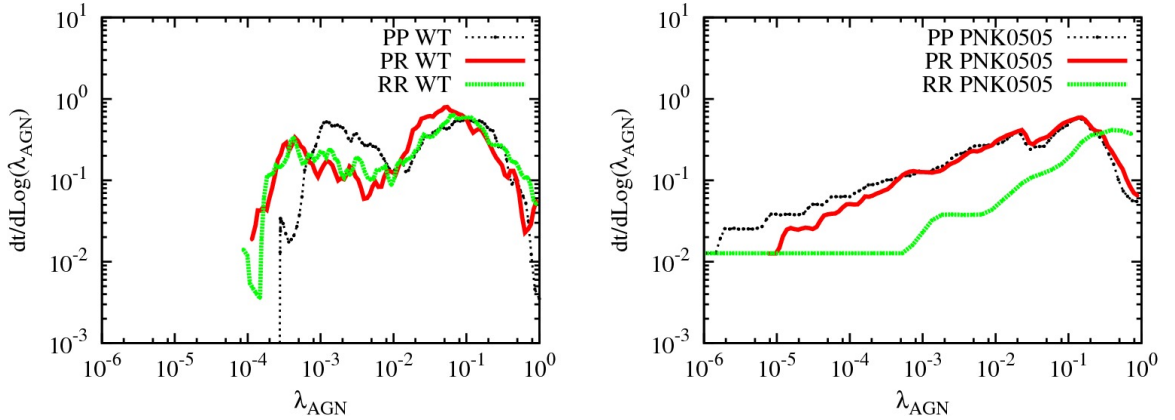
Figure 4.6: A comparison between the activity functions of two low resolution simulations (denoted by the different colors) starting from the same ICs only differing in their gas's rotational orientation. The left (right) figure shows the simulations using the WT_l ($PNK0505_l$) model. Changing the gas's rotational orientation did not affect the activity functions of the WT model contrary to those of the PNK0505 model.

4.1.5 GALACTIC INCLINATION

In addition to aligning the galaxies' gas angular momentum vector (rotational orientation), the galactic planes are also aligned which is a comparatively unlikely scenario. Here, we test the impact of changing the galactic disc alignments on the final remnant. We compare two low resolution simulations using the WT model and initial alignments $\alpha \in \{0°, 90°\}$ where α is the angle between the normal vectors ($\hat{n}_1$ & $\hat{n}_2$) of the disc planes ($\alpha = \arccos(\hat{n}_1 \cdot \hat{n}_2)$). Figure 4.7 shows a comparison of the results of the aforementioned simulations.

Although altering α changes the morphology of the remnant, the simulations with different inclinations yield final BH masses, SFRs and accretion rates that vary within 4%, 8%, and 14% from the averages, respectively. It is worth noting that although the final BH mass, SFR, and accretion rates closely agree, the simulation with $\alpha = 90°$ shows a delay in the BH merger (notice the delayed decrease in the SFR and accretion rate). On the other hand, the activity functions produced by both simulations agree for high Eddington ratios ($\lambda > 0.1$) although the tilted simulation spend more time at Eddington luminosities. The simulation with higher inclination shows more activity at intermediate Eddington ratios ($\lambda \in [10^{-2} : 10^{-1}]$) while the low λ cut-off extends to slightly lower Eddington ratios. Also, the low λ peak is not prominent. These features are consistent with AGN feedback due to high accretion rates ($\lambda \sim 1$) causing the BH to accrete more at intermediate and low Eddington ratios. The differences can again be related to the different dynamics of the remnant.
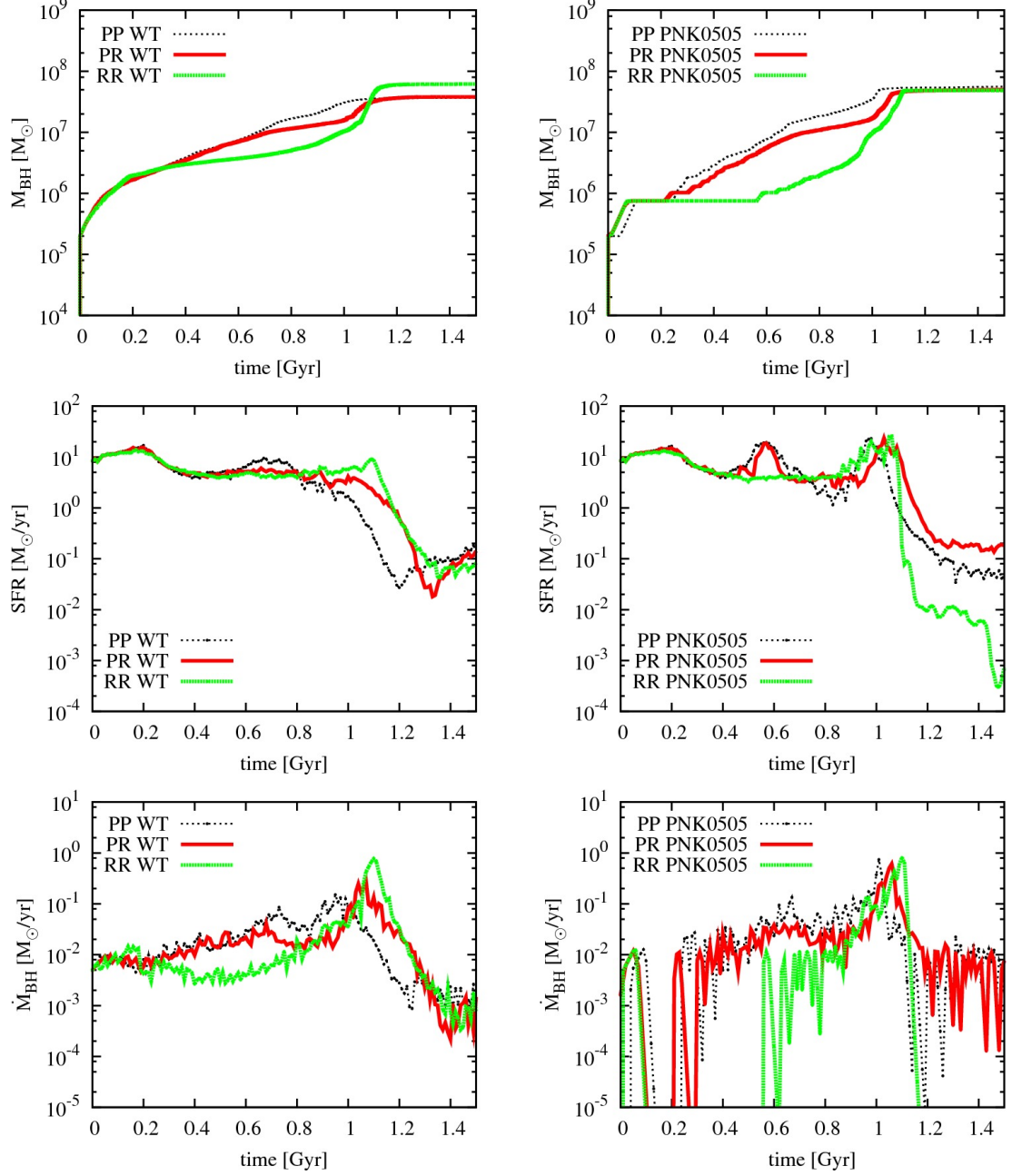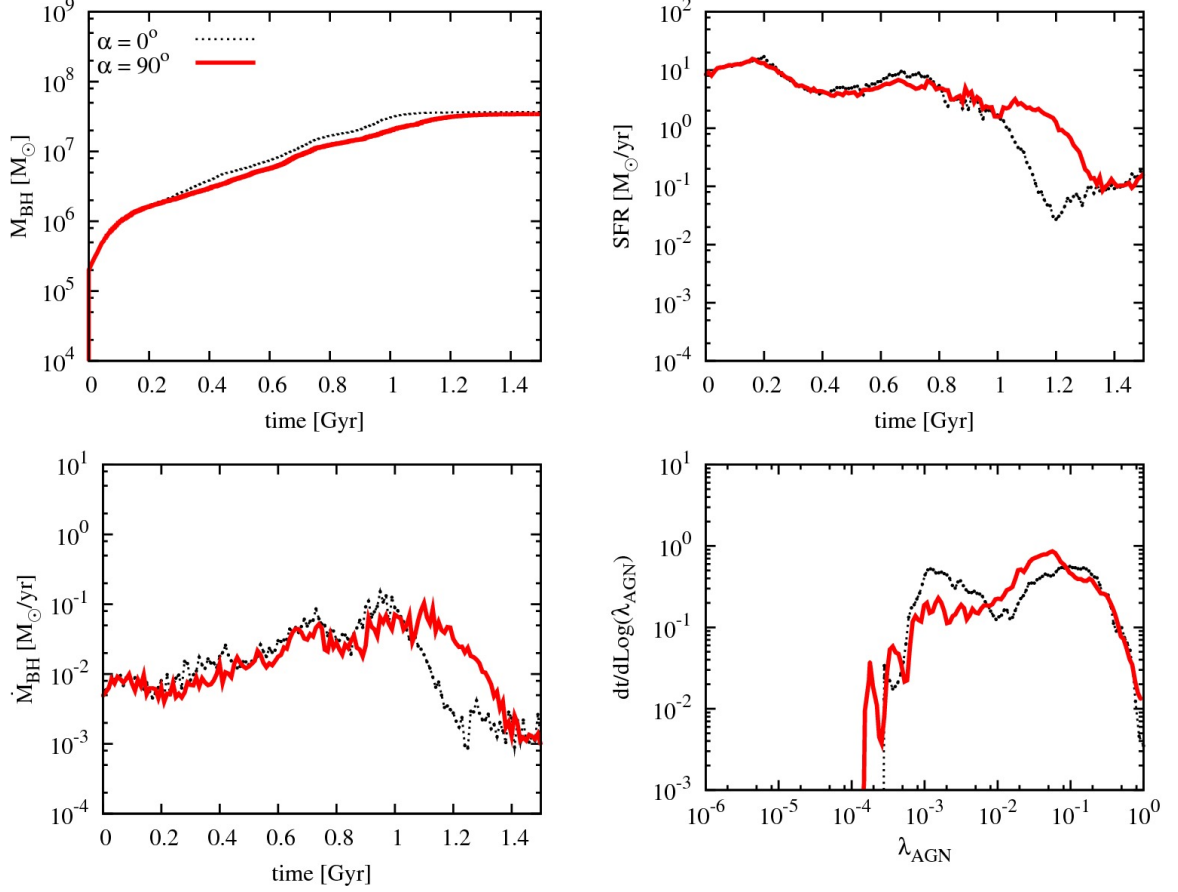
Figure 4.7: A comparison between two low resolution simulations (denoted by the different colors) using the WT model and starting from the ICs only differing in their inclination. The sub-figures show the total BH mass (sum of the two BH masses), total SFR, total BH accretion rate, and the activity function throughout the simulation. Changing the inclination of the galaxies has insignificant effect on the final BH mass, SFR, and accretion rate (variations less than 15% from their respective averages). However, there are some minor observed differences in the instantaneous values where the simulation with higher inclination shows a delayed BH merger. The activity functions are qualitatively similar with some differences in the low-λ cut-off, low-λ peak, as well as the activity at intermediate Eddington ratios. These differences can be attributed to the different dynamics of the remnant.

4.1.6 PNK: Viscous Timescale

The PNK model has two basic free parameters: the accretion radius and the viscous timescale. As shown in figure 4.9, the activity functions produced by different PNK models can be significantly different. In this section we examine the effects of using different timescales on the BH mass, SFR and the activity function. We will ignore PNK0205, and PNK0510 in this comparison as they produce nonphysical results (Wurster and Thacker 2013b). Figure 4.8 compares high resolution simulations using different PNK models. The simulations used in this section were run and analyzed in detail by Wurster and Thacker (2013b).

Different PNK models produce BH masses and SFRs that vary within 15% and 27% from the average respectively. Changing the radius of accretion does not appreciably change the activity function (see PNK0505 and PNK1005). However, decreasing the viscous timescale associated with the ADP significantly alters the activity function. Because matter is transferred faster onto the BH, the BH can spend more time at around the Eddington luminosity. Associated with the high accretion rates, AGN feedback halts the accretion causing the BH to accrete at lower rates therefore extending the low λ tail and creating a peak at intermediate Eddington ratios ($\lambda \sim 0.01$).

Conversely, increasing the timescale allows a longer delay in accretion and therefore feedback. This results in more significant differences around the BH (higher densities with more gas accumulating due to the longer periods with minimal feedback) which, in turn, allows higher accretion rates after the gas has accumulated. This behavior causes a truncation in the lower λ tail of the activity function as the BH spends less time accreting at lower rates.

77
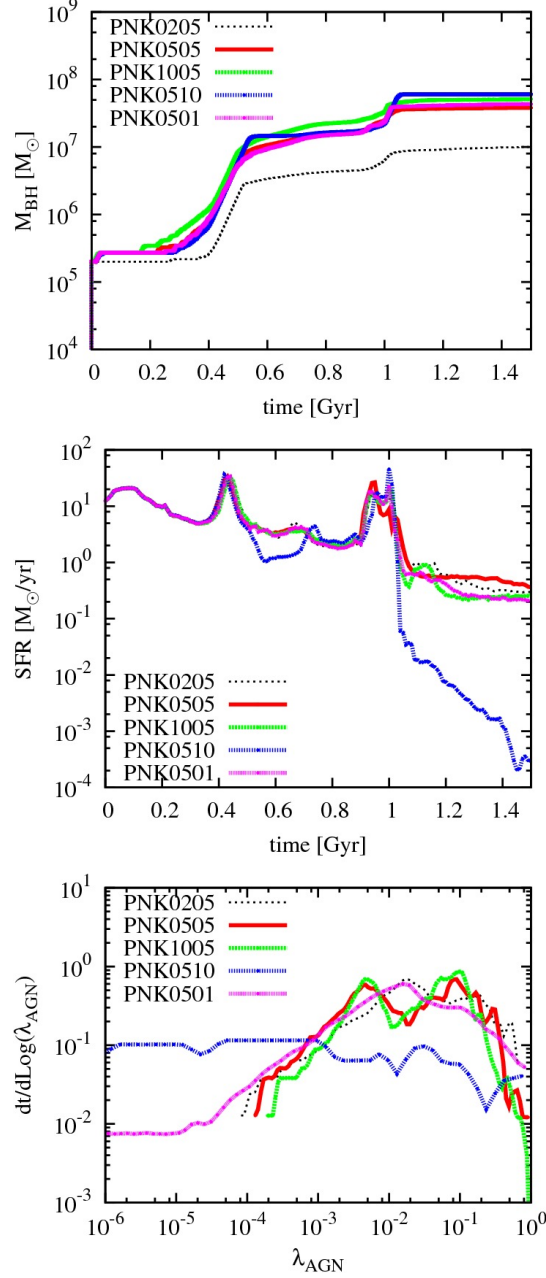
Figure 4.8: A comparison of high resolution simulations using the PNK model with different values for the viscous timescale and the accretion radius. We ignore the analysis of PNK0510 and PNK0205 which yield nonphysical results (Wurster and Thacker 2013b). Changing the PNK viscous timescale does not seem to strongly affect the BH mass or SFR (15% and 27% variation from their respective averages). However, decreasing the viscous timescale yields more activity at the Eddington luminosity ($\lambda \sim 1$). To the contrary, changing the radius of accretion does not seem to have a significant impact on the resultant AF.

4.2   AGN Activity: More Detailed Analysis

Having demonstrated the expected differences in the results due to differences in the ICs and model parameters (see §4.1), we now proceed to presenting the simulation results. In this study we are interested in examining some key properties of the AGN activity function. As discussed in chapter 2, the activity function can be related to the luminosity distribution of AGN (Hopkins and Hernquist 2009). Therefore, understanding and constraining the activity function is essential for constraining BH activity in galaxy evolution models and understanding the evolution of different galactic properties (Hickox et al. 2014).

4.2.1   Activity Functions

This section presents the activity functions produced by high resolution simulations using the models presented in table 3.1 and described in detail in chapter 3. Note that the activity functions were calculated for $t \in [0.6, 1.5]$ Gyr to minimize the artificial effects due to stabilization of the initial transients of the ICs, and restrict the focus on the merger and post-merger epochs.

Figure 4.9 and the lower panel of figure 4.8 show the activity functions produced by fiducial resolution simulations using the aforementioned models. The first observation is that none of the presented models reproduce the activity function inferred from observations (Schechter function; e.g. Hopkins and Hernquist 2009): The modeled AGN spend less time being quiescent (at low Eddington ratios), than inferred from observations. The models produce either a flat distribution (BS), a wide lognormal-like distribution (WT, DQM), a lognormal distribution with a skewed high λ tail (SDH), or a peaked activity function at high λ with a low λ tail (PNK, HPNK). The low λ tail of the PNK distribution is related to the mass transfer from the accretion disc onto the BH. Other models have a finite cut-off in Eddington ratios which is caused by the mass resolution of the simulations defining a minimum accretion rate and hence minimum luminosity and Eddington ratio. Variations of the presented models produce activity functions similar to those produced by the parent model.
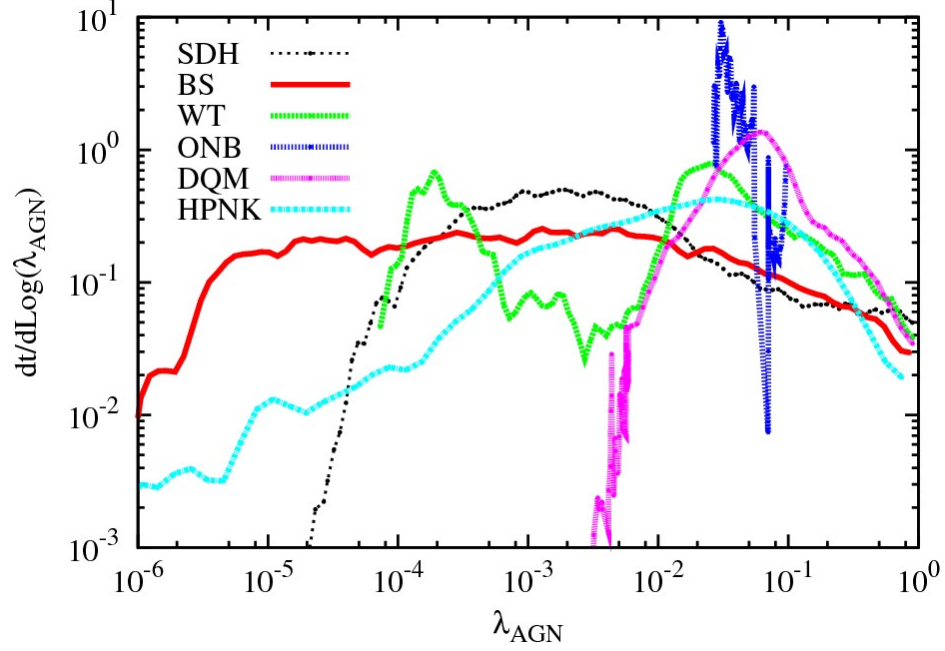
Figure 4.9: The activity functions of high resolution simulations using the models in table 3.1. None of the seven models reproduce a Schechter-like activity function as inferred from observations.

However, before even interpreting these results it is important to emphasize that the results integrate over a broad spectrum of BH masses and should ideally be considered within small mass ranges. Note that the activity function is related to the quasar luminosity distribution at a given mass (see equation 2.3). In the next sections we will examine the AF's dependence on various galactic properties.

4.2.2 ACTIVITY FUNCTIONS AND BH MASS

So far we have been calculating the AGN activity function without any distinction between BHs of different masses. However, the activity function is usually derived on a mass dependent basis. Therefore, it is more insightful to examine the mass dependent activity functions produced by different models. Note that this may introduce some bias to the analysis because a given BH mass is directly proportional to the time/stage of evolution in the merger. Nonetheless, examining the mass dependent activity function will still shed some light on the activity of AGN in different luminosity regimes. Figures 4.10 & 4.11 show the mass dependent activity function of the

AGN evolved using the models in table 3.1. The BS, SDH, and WT models seem to qualitatively reproduce a Schechter trend in their passive stage (high BH mass). Contrarily, HPNK shows an increasing time as a function of Eddington ratio at low Eddington ratios for all BH masses (the AF increases to a peak $dt/d \log \lambda$ then decrease again). In the the ONB model, the non-local feedback prescription allows the formation of a dense galactic core (Wurster and Thacker 2013b). This behavior produces a constant accretion rate which limits the activity functions to lognormal-like peaks at moderate Eddington ratios. ONB still shows an expected shift (although small) in the activity function to lower Eddington ratios at higher BH masses (higher BH mass with a constant accretion rate yields a lower Eddington ratio). Model SDH, shows an increase in the time spent at lower Eddington ratios for higher BH mass (shift in the peak to lower λ) with a decrease in the time spent at high Eddington ratios. On the other hand, model DQM shows a lognormal activity function, peaked at moderate to high λ , for all masses with an insignificant low λ tail at some masses. Lastly, the PNK0505[3] model shows an increase in the time spent at lower Eddington ratios for high BH masses although it still does not reproduce the Schechter function shape.

None of the models reproduces the AF inferred from observations (Schechter function) when integrating over the entire merger time. However, at high BH masses (passive stages of the evolution) all models spend consistently more time at lower Eddington ratios. During the passive stages of the evolution, the WT model produces an activity function that qualitatively best resembles a Schechter function (consistent with observations). The AF produced by the WT model at high BH mass shows a sharp decline in activity for $\lambda > 2 \times 10^{-2}$ and a increasing low λ tail with maximum activity at $\lambda \sim 2 \times 10^{-4}$. This resembles a Schechter function with a knee at $\lambda \sim 2 \times 10^{-2}$. A close second is the BS model which produces a Schechter like AF at high BH mass; however, the decline in activity at high Eddington ratios is very shallow and the low λ tail is flat.

---

[3]All other PNK models, except PNK0205 and PNK0510 which produce nonphysical results (Wurster and Thacker 2013b), produce similar activity functions for different mass bins
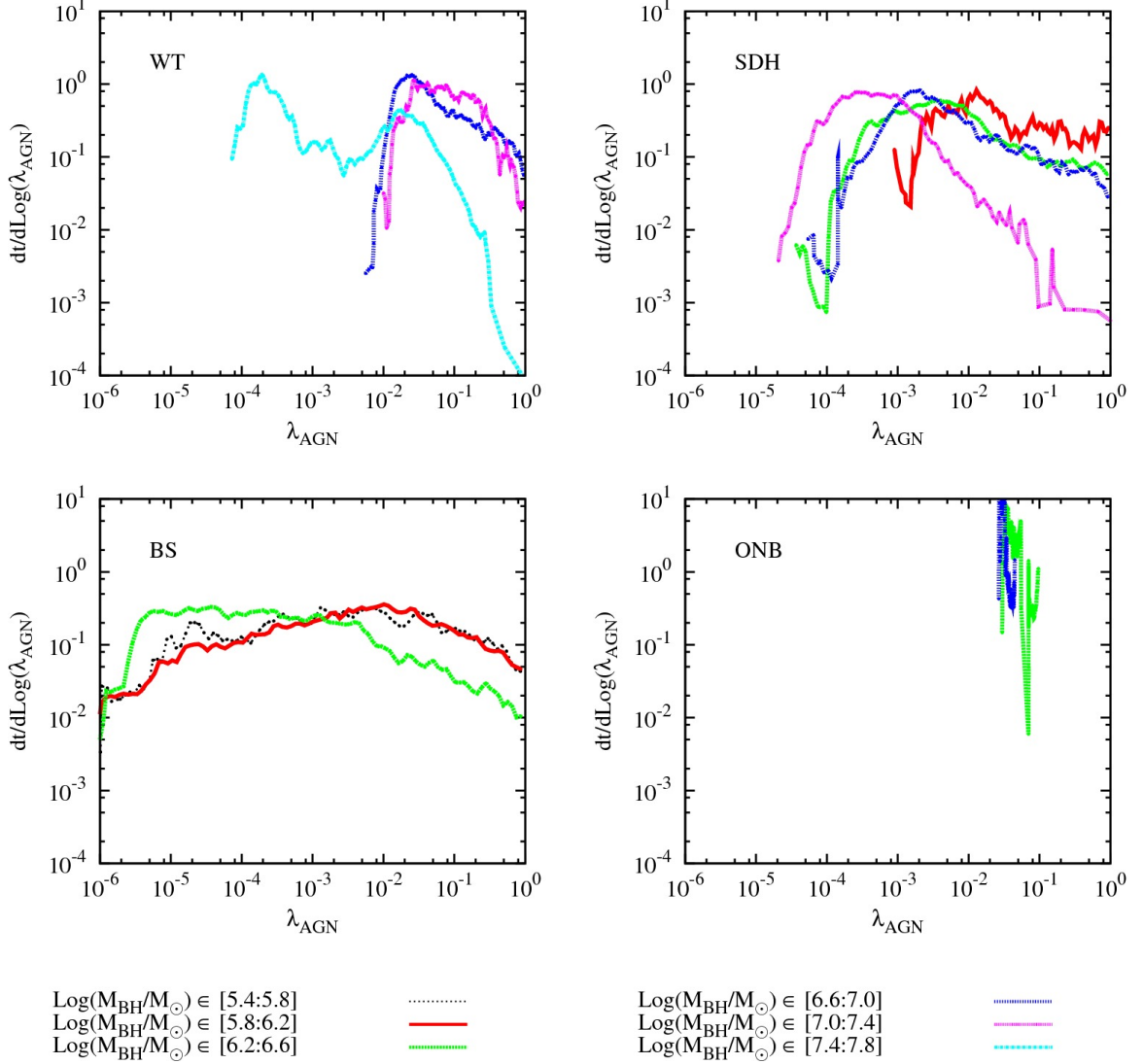
Figure 4.10: The mass dependent activity functions of high resolution simulations using models WT, SDH, BS, and ONB(see table 3.1). Note that the other three models are shown in figure 4.11. Some models produce a monotonically decreasing activity function during the galaxy's passive evolution which is consistent with the activity function inferred from observations.

4.2.3 POWER SPECTRUM OF THE AGN ACCRETION RATE

The accretion rate shows variations on different time scales during the simulation. These variations are governed by the properties of the local gas in the BH's neighborhood as well as the streaming of galactic gas onto the central region. Understanding the timescales associated with the variation of the accretion rate may help shed some light on the internal physical properties governing the accretion process although the inference is non-trivial. Figure 4.12 shows a comparison of the power spectra
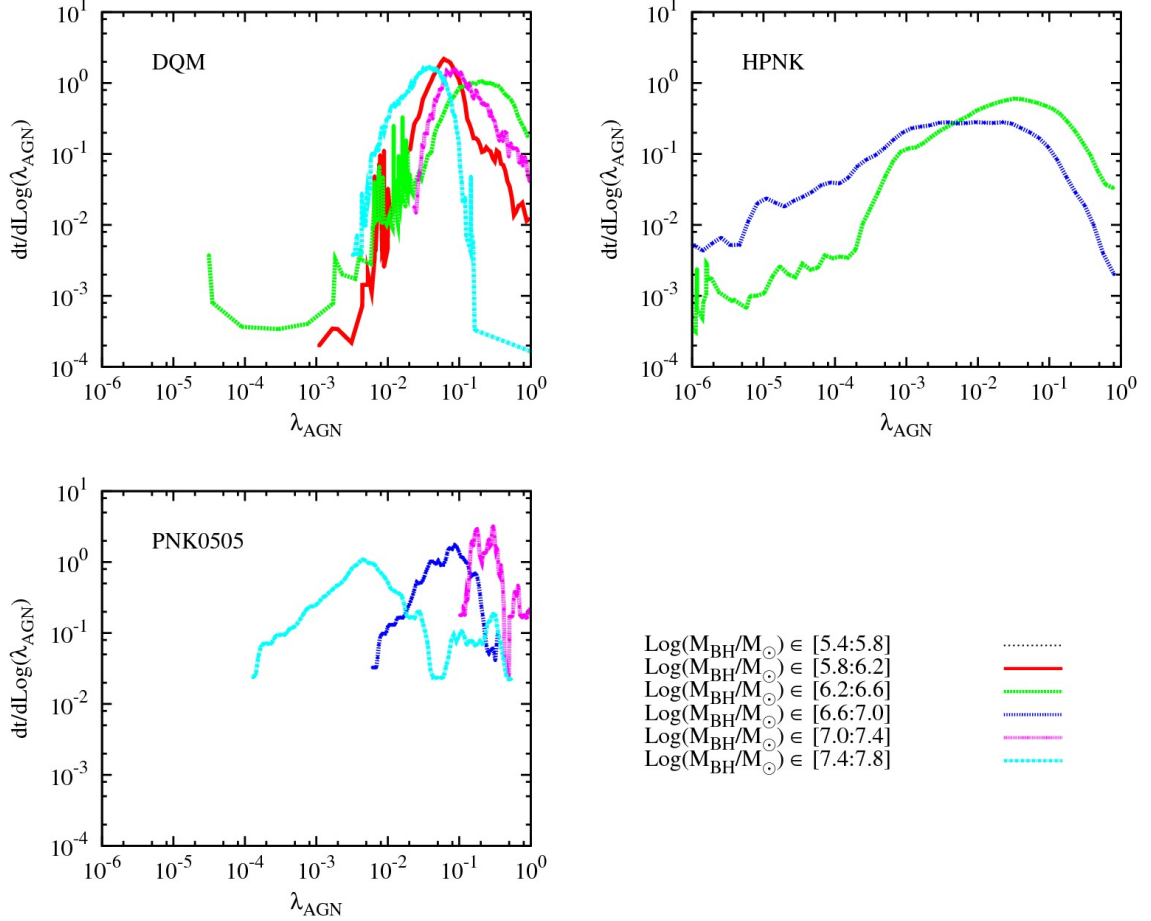
Figure 4.11: Same as figure 4.10 using models HPNK, PNK0505, and DQM. Note that the activity function represented by a delta function at $\lambda = 1$ for some intermediate mass bins during are not shown in this figure.

of the BH Eddington ratio of different models in high resolution simulations. The power spectrum (PS) of the Eddington ratio contains valuable information pertaining to the timescales that best describe the variations in accretion and therefore the various processes involved (Novak et al. 2011). The frequencies were limited to a minimum of the inverse of the time of the simulations $(1/1.5\,\mathrm{Gyr}^{-1})$ because variations on timescales larger than $1.5\,\mathrm{Gyr}$ cannot be extracted from observations over the simulation timescales. The error bars represent a 1σ variation within a frequency bin.

The high frequency peak observed in all models is caused by the chaotic behavior in the immediate neighborhood of the BH as well as numerical artifacts, primarily

the discreteness of accretion. Nonetheless, despite the complicated underlying physics, all models show a similar trend in their PS (proportional to $1/f^2$) for $f < 10\,\mathrm{Myr}^{-1}$ which is, intriguingly, consistent with a superposition of random noise and a decay in the Eddington ratio (increasing BH mass and/or decreasing accretion rates). Note that $1/f^2$ noise, also referred to as Brown noise, is common in systems exhibiting stochasticity. Here the BH evolves in a chaotic gaseous medium. Therefore the change in the accretion rate can be expressed as a function of the accretion rate and a stochastic term representing the chaotic properties of the BH environment. The models also show features of white noise at low frequencies ($f \sim 10^{-3}\,\mathrm{Myr}^{-1}$).

The ONB model shows minimal variations from the $1/f^2$ power law. The origin of such behavior is not fully understood; it may be due to the BH residing in a slowly changing environment caused by the balance between gas inflow into the galactic core and gas accretion (due to the non-local feedback) and therefore accreting at a steady accretion rate affected only by the stochastic environment.

On the other hand, the peak in the PS of some models (BS, WT, SDH, & HPNK) at $f \sim 0.3\,\mathrm{Myr}^{-1}$ may be attributed to the rapid variations in the gas characteristics around the BH due to feedback outflows and BH motion. All the models showing a peak implement thermal feedback (heating); because cooling timescales are temperature dependent, an increase in the power is observed over a range of frequencies $f \in [\sim 0.3 :\sim 25]\,\mathrm{Myr}^{-1}$. This is consistent with the power spectrum of brown noise including a driving term (fluctuation dissipation theorem). Including driving terms (feedback and cooling) produce peaks in the power spectra of the brown noise.

The wind models (PNK and DQM) follow the $1/f^2$ power law with some peaks[4] in power at intermediate frequencies which may be related to the re-collapse of material after being ejected due to feedback.

---

[4]The peak at $\sim 3\,\mathrm{Myr}^{-1}$ in the DQM model may be due to the different evolution of the system caused by the constant tracer mass (Wurster and Thacker 2013a).
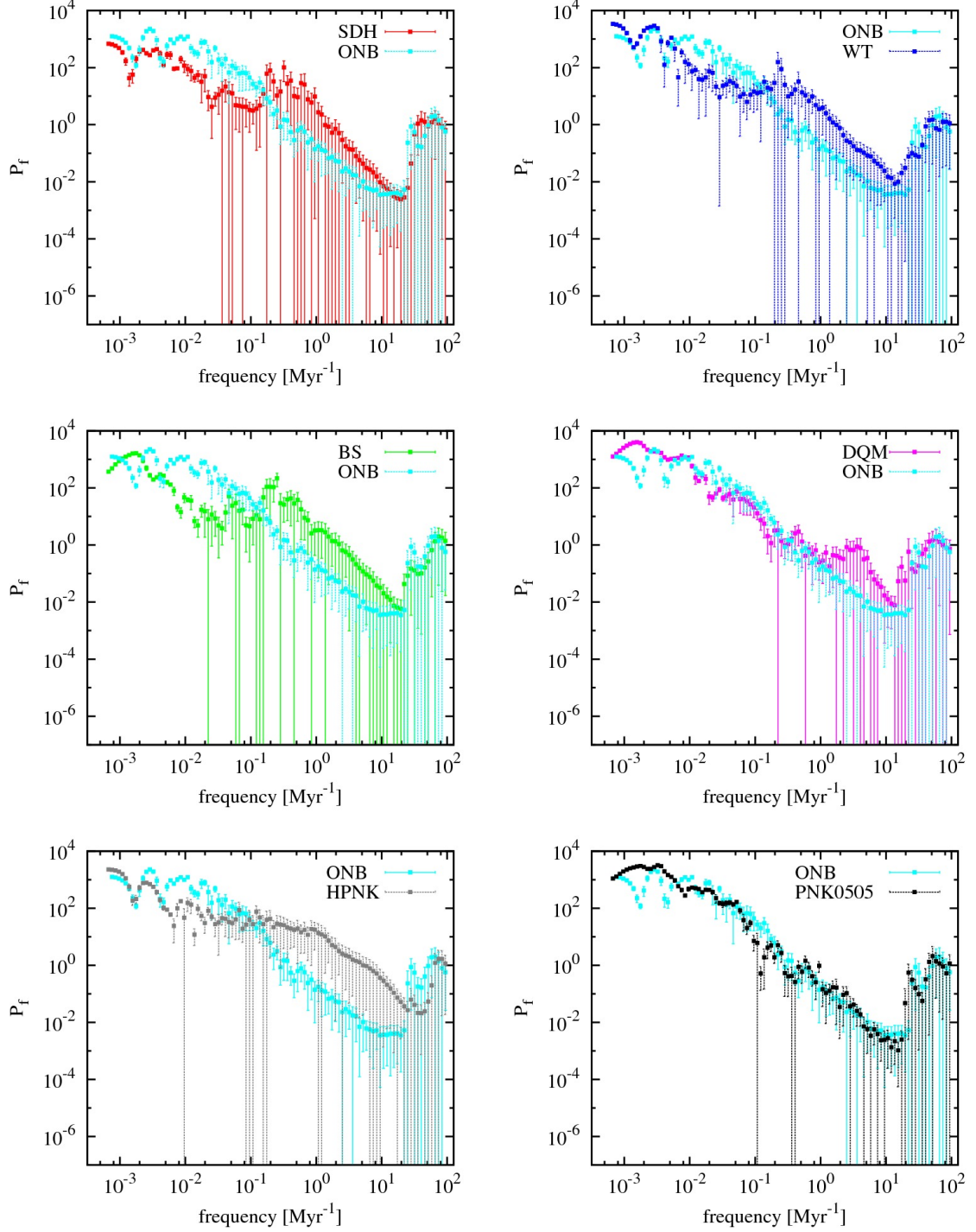
Figure 4.12: A comparison between the power spectra of the BH Eddington ratio of high resolution simulations using different BH models. The error bars show 1σ variations in the power. The models follow a somewhat surprising $1/f^2$ power law which is consistent with a superposition of random noise and a decay in the accretion rate.

85

4.2.4   WT: Modified Bondi Accretion

The activity function encapsulates important information pertaining to BH activity in a galaxy. Knowing that BH activity is directly correlated with the accretion rate, it is interesting to observe the effect of changing the accretion rate power law on the activity function. While the physics of BH accretion is well prescribed, the relation between small and large scales is interpolated in simulations. So the consideration of the effective power law for accretion is at least moderately motivated (such considerations underlie the BS model). We are particularly interested in examining the effect of changing the accretion rate on the low λ tail of the activity function (i.e. reproducing the observed low λ tail of the Schechter function by allowing the BH to spend more time at lower accretion rates) while maintaining the impact of accretion on the galaxy.

Starting from the Bondi accretion rate shown in equation 3.23, we modify it by changing its dependence on the local density (ρ). The density term is raised to the power $\kappa \in \{0.5, 2, 3\}$. To maintain a proper normalization in the accretion rate, we change the free parameter, α, such that $(\alpha, \kappa) \in \{(10, 0.5), (0.1, 2), (0.01, 3)\}$. Figure 4.13 shows the effect of changing the accretion rate used in the WT model in three low resolution simulations using the same ICs. The SFR exhibits negligible change (within less than a factor of 2 from the average) before the core merger ($t \sim 1.0\,\mathrm{Gyr}$), with some notable differences (a factor of 2.25 from the average) in the later stages of the simulation. The BH growth shows minimal differences with a final BH mass varying within 18% of the average. Although the system's self regulation produces merger remnants with similar properties, the activity functions show notable differences.
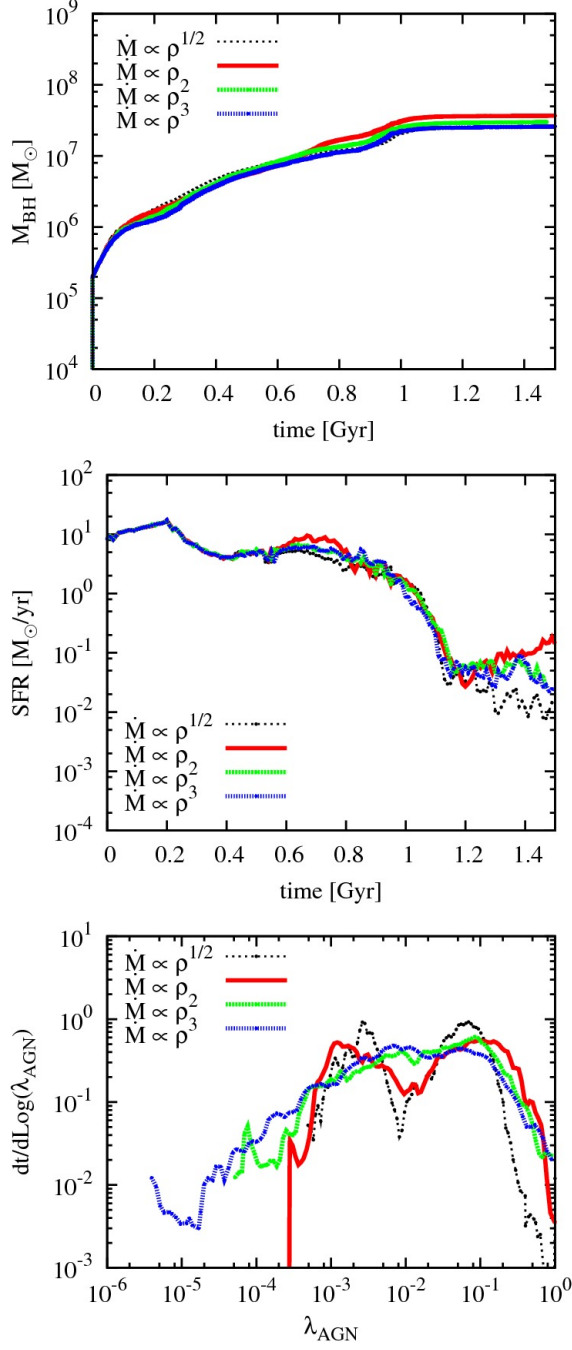
Figure 4.13: A comparison of three low resolution simulations using the WT model with different accretion rates. The top row shows the BH mass during the simulation, the middle row shows the SFR and the third row shows the activity function. Altering the accretion rate's dependence on the local density changed the final BH mass and SFR by less than a factor of two. The activity function is smoother for a higher dependency on density; it also has a tail extending to lower Eddington ratios.

Increasing the dependency on the density (increasing κ), increases the time spent at Eddington luminosities, $\lambda \sim 1$. Note that the increase in the time spent at $\lambda \sim 1$ reaches a maximum (i.e. $\dot{M}_{BH} \propto \rho^{2,3}$); this is due to AGN feedback. However, feedback due to high accretion rates regulates the system forcing the BH to accrete at lower Eddington ratios and therefore extending the low λ tail of the activity function to consistently lower Eddington ratios. Moreover, increasing the value of κ, reduces the dip at intermediate Eddington ratios and therefore the activity function appears to be smoother. However, changing the dependency of the accretion rate on density does not allow us to reproduce the activity function inferred from observations.

4.2.5 MASS DEPENDENCE OF THE ACTIVITY FUNCTION

In this section we examine the effects of the galaxy mass on the AF. We present low and fiducial resolution simulations of galaxies that have been scaled by a factor of 0.1. This is motivated by observations suggesting that the activity function is mass invariant (e.g. Hopkins and Hernquist 2009) as well as the aforementioned results: Scaling the galaxy mass implies an equivalent scaling the BH seed mass which will affect the AF (section 4.2.2 demonstrates that the AF shows significant dependence on the BH mass). Moreover, changing the galaxy seed mass affects the cumulative gas mass available in the simulation and therefore the amount of gas available for accretion.

Because of the similarities in the AFs of the models, we continue the analysis for two models only: WT and PNK0505. The WT model is chosen because of its superior ability to model BH properties (Wurster and Thacker 2013a,b; Thacker et al. 2014) and the similarities between the produced AF and the one inferred from observations during the passive stage. The PNK model is chosen because of its distinct accretion mechanism (see §3.6.6) that follows/predicts down to very low accretion rates.

Low Mass - Low Resolution Simulations

Figure 4.14 shows the AFs produced by the low mass galaxies compared to those produced by the unscaled Milky Way like galaxies using both the WT_l and $PNK0505_l$ models.
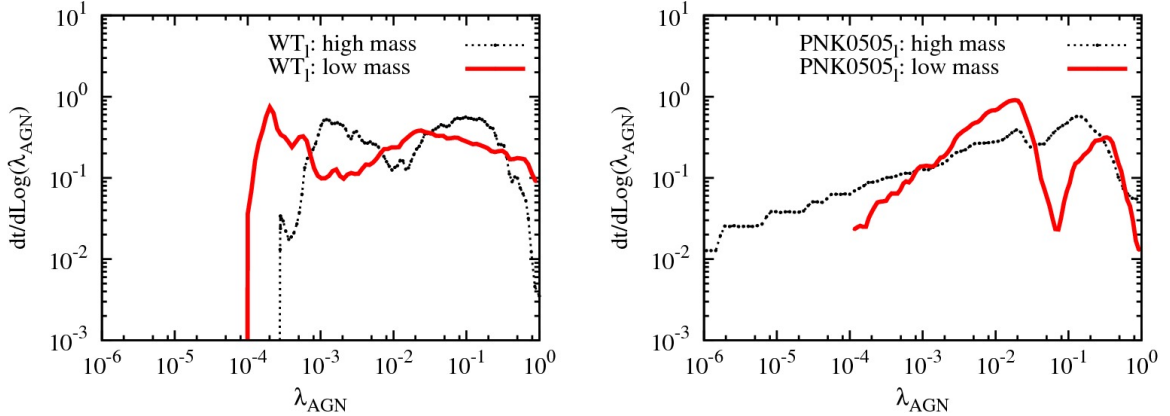
Figure 4.14: The AFs produced by low resolution simulations with low mass ICs using the WT model (left) and PNK0505 model (right) compared to simulations with unscaled Milky Way like ICs. Reducing the galaxy mass impacts the low λ tail and the intermediate λ peak ($\lambda \sim 10^{-2}$) of the AF in both models. The impact on the high λ activity ($\lambda \sim 1$) is model dependent.

The low mass simulations using the WT_l model show a significantly different growth in the BH mass over the simulation time (see figure 4.15): The BH grows by a factor of ~ 263 in the the low mass simulations as opposed to the growth of ~ 184 times in the high mass simulations at the same particle resolution. A significant portion of this growth (a factor of ~ 17 in the low mass simulations and ~ 9 in the low resolution high mass galaxies) happens during the merger following an epoch of intermediate accretion which allows the formation of a dense nucleus and therefore high accretion rates. This is consistent with the BH accreting at the Eddington luminosity which is reflected in the AF as an increase in the activity at $\lambda \sim 1$. Moreover, the high Eddington ratios are associated with a powerful feedback burst at the core merger. This feedback coupled with the lower particle masses in the low mass simulations, allows a lower λ cut-off in the low mass simulations using the WT_l

model[5]. We caution that the increase in activity in the low mass simulations at low λ may be slightly affected by the fact that the integration in the passive stage is longer (core merger at $\sim 0.72\,\mathrm{Gyr}$ in the low mass simulations compared to $\sim 1.0\,\mathrm{Gyr}$ in the high mass simulations).
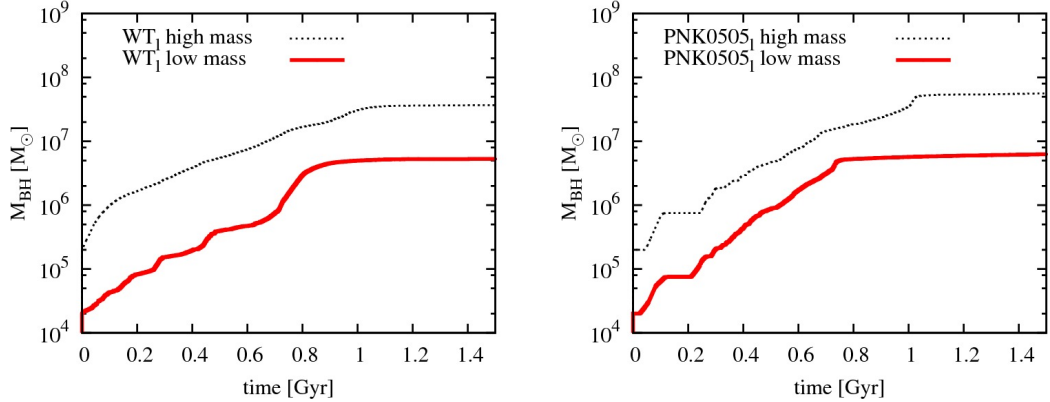
Figure 4.15: The total BH mass produced by low resolution simulations with low mass ICs using the WT model (left) and PNK0505 model (right) compared to simulations with unscaled Milky Way like ICs. The low mass galaxies using the WT model show more significant BH growth during the merger ($t > 0.6\,\mathrm{Gyr}$) when compared to the higher mass galaxies.

On the other hand, the PNK0505$_l$ model exhibits similar activity to the WT$_l$ model. During the merger, the BH accretes at high Eddington ratios, $\lambda > 10^{-1}$, until a burst of feedback (at the core merger) creates a void around the BH shifting the accretion to lower Eddington ratios and therefore creating the low λ peak ($\lambda \sim 10^{-2}$). Note that the low mass simulations show less activity at high Eddington ratios (lower peak) when compared to the high mass galaxies because the merger concludes faster. The effects of the feedback burst at the core merger can be seen as a sharp decline in the BH accretion rate as well as the densities around the BH after the merger causing a prominent dip in the activity function which becomes slightly bi-modal.

Also, reducing the gas particle mass allows lower accretion rates, and therefore less feedback, during the post merger stage; this reflects as more frequent accretion

---

[5]Contrary to the PNK0505$_l$ model where reducing the particle mass allows more frequent accretion during the passive stage and therefore cuts off the low λ tail at higher Eddington ratios.

during the post merger stage and therefore the low λ tail does not extend to low Eddington ratios ($\lambda \sim 10^{-5}$). Similar behavior is observed when increasing the particle resolution in the fiducial simulations. The low λ tail is caused by mass transfer from the accretion disc onto the BH. Increasing the time between accretion events causes the low λ tail to extend to lower Eddington ratios. However, with the low accretion rates and therefore weaker feedback, particles accrete onto the ADP more frequently and therefore interrupt the mass transfer giving rise to a truncated activity function (sharper cut-off at lower Eddington ratios).

The aforementioned differences in the AFs of the low and high mass simulations are reflected by other physical quantities: The BH growth being reduced during the merger (less activity at the Eddington luminosity; contrary to the WT_l model) in the low mass simulations (a factor of ~ 3.5 vs. ~ 7 in the high mass simulation). However, the total BH growth during the simulation is higher in the low mass simulation; the ratio of the final BH mass to the initial BH mass is ~ 314 (~ 281) for the low mass (high mass) simulation.

One can also compare the mass dependent activity function in the low mass simulations and that of the high mass simulations; such a comparison is shown in figure 4.16. For both galaxy masses the WT model shows qualitatively similar behavior (see §4.2.2): The produced AF resembles what is inferred from observations (Hopkins and Hernquist 2009) during the passive stages of evolution (high BH mass) and the AF peaks at consistently lower Eddington ratios for higher BH mass. The PNK0505 model does not reproduce what is observed, however it shows a shift in the peak of the AF to lower Eddington ratios during the post merger epoch. For a more detailed description see section 4.2.2.

Given the differences in the ICs of the low and high mass galaxies (i.e. different BH mass and particle mass), the ratio $M_{BH}/M_{BH,0}$ (ratio of the BH mass to the initial BH mass) presents a more useful indicator of evolution than the BH mass as it closely scales with time independent of the galaxy mass. This allows a direct comparison between the low mass and high mass galaxies. Figure 4.17 shows the activity functions

produced by the low mass and high mass galaxies using models WT_l and $PNK0505_l$. The aforementioned figure explicitly indicates that the AF shifts to lower Eddington ratios during the passive stages of the evolution.
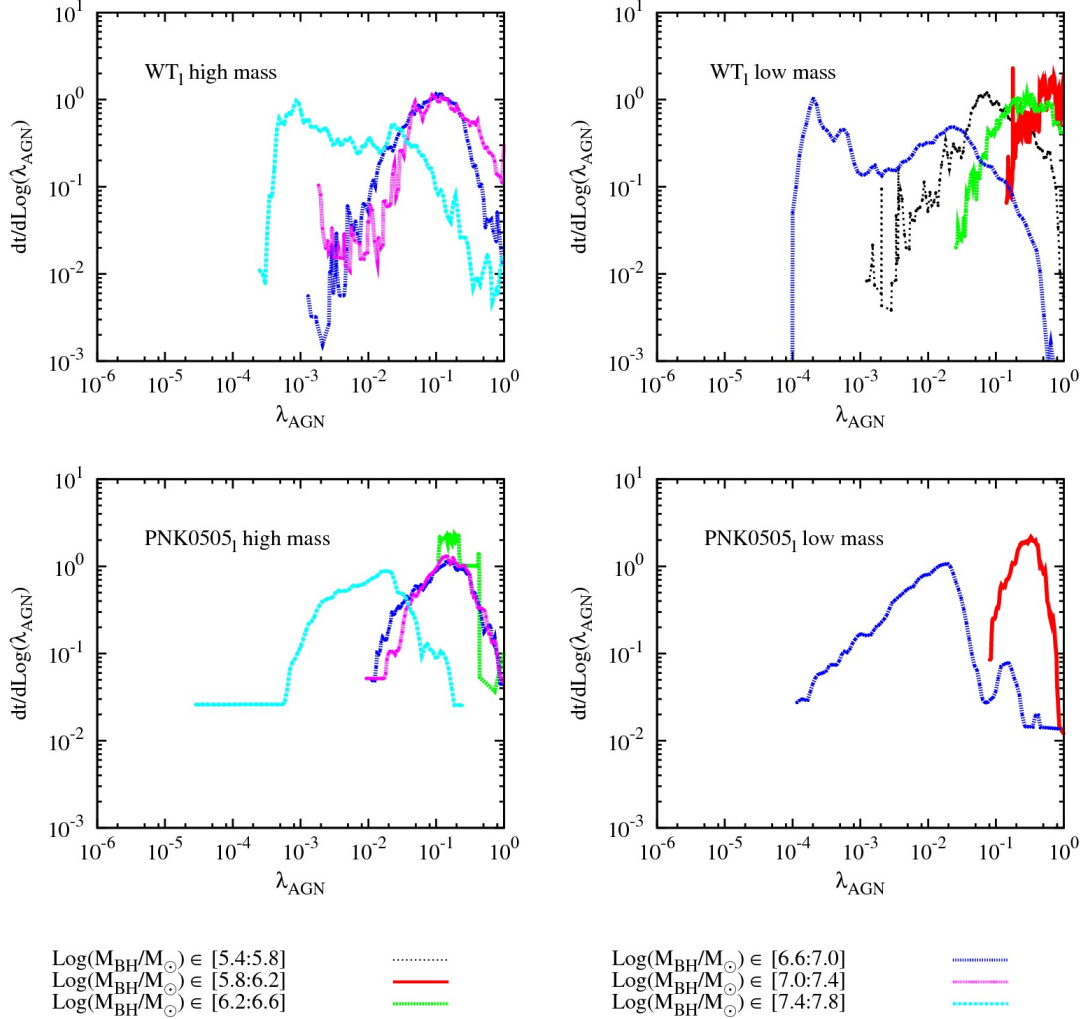
Figure 4.16: The mass dependent AFs produced by low resolution simulations with low mass ICs (right) using the WT (top) and PNK0505 (bottom) models compared to simulations with unscaled Milky Way like ICs (left). For a given model, both low mass and high mass galaxies exhibit similar behavior at different stages of the evolution. Note that the activity function represented by a delta function at $\lambda = 1$ for some intermediate mass bins are not shown in this figure.

Motivated by the shift in the AF to lower Eddington ratios for higher BH mass (which we associate with passive evolution), we next directly examine the effect of

evolution on the activity function. Figure 4.18 shows the activity function produced by low and high mass galaxies using models WT and PNK0505 across pre and post merger stages. The core merger times are shown in table 4.1. For both galaxy masses, the models show more activity at lower Eddington ratios during the passive stage of the evolution as the activity function shifts to lower Eddington ratios.

Model	Galaxy Mass	t_{merge} [Gyr]
WT_l	high mass	1.00
	low mass	0.72
$PNK0505_l$	high mass	1.07
	low mass	0.73
WT	high mass	1.02
	low mass	0.74
PNK0505	high mass	1.01
	low mass	0.74

Table 4.1: The time of the core merger (t_{merge}) in the low and high mass simulations (at both low and fiducial resolution) using the WT and PNK0505 models.

Figure 4.17: The AFs produced by low resolution simulations with low mass ICs (right) using the WT model (top) and PNK0505 model (bottom) compared to simulations with unscaled Milky Way like ICs (left). Here the AFs are plotted in different $M_{BH}/M_{BH,0}$ bins which is an indicator of the evolutionary stage. The activity function is independent of the overall galaxy mass for this resolution while it shows strong dependence on the evolutionary stage. Note that the activity function represented by a delta function at $\lambda = 1$ for some intermediate mass bins during are not shown in this figure.
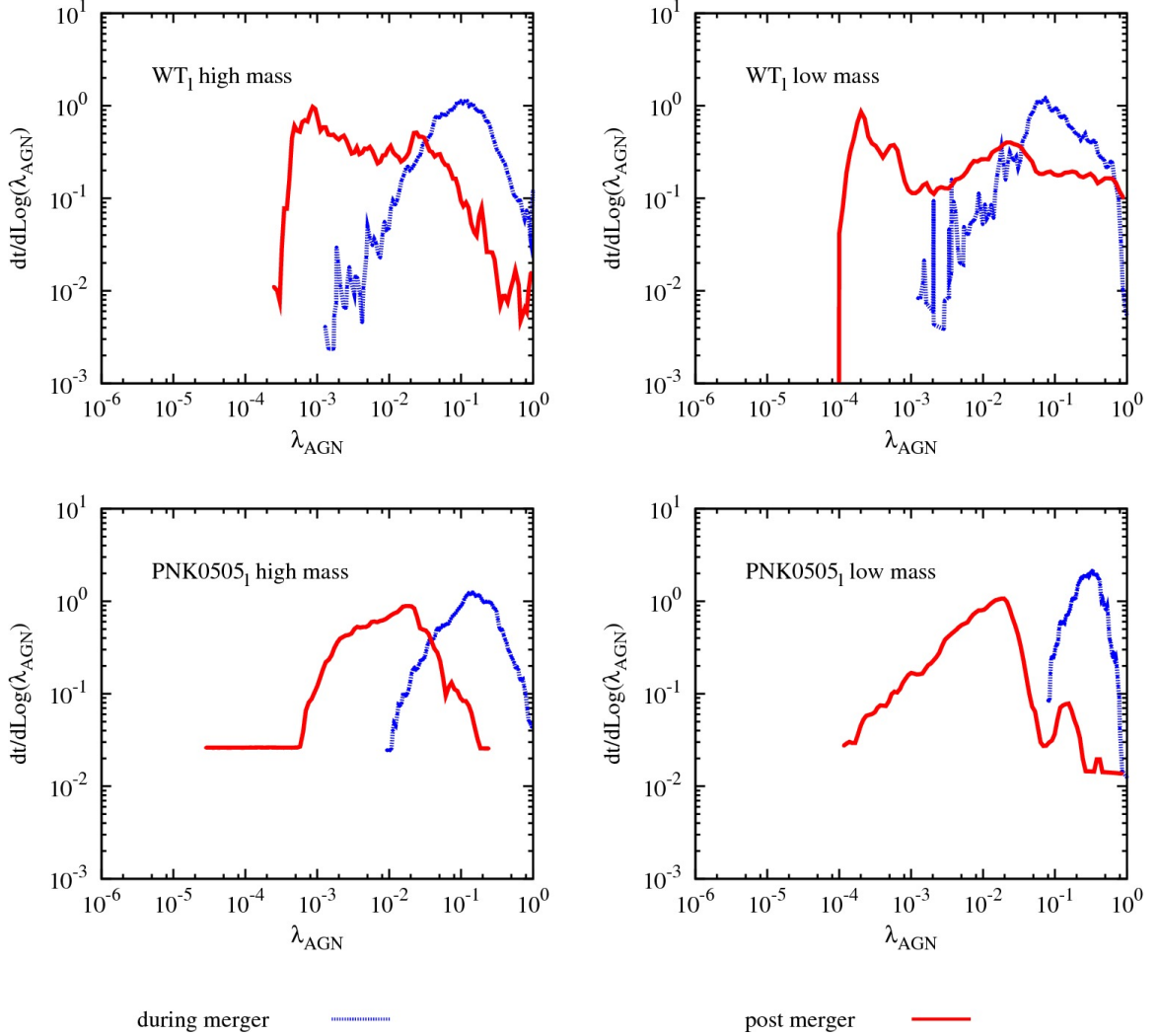
Figure 4.18: The AFs produced by low resolution simulations with low mass ICs (right) using the WT model (top) and PNK0505 model (bottom) compared to simulations with unscaled Milky Way like ICs (left). The AF is shown during different stages of the evolution indicating a strong dependence of the AF on the evolutionary state of the system

In summary, we have explicitly demonstrated how the activity function, at this resolution, is at least qualitatively, mass invariant (the activity function is a property of the evolutionary stage in major mergers instead of the overall galaxy mass or BH mass): i.e. the same BH mass bins have different activity functions between the two systems (different masses) while similar stages of evolution show similar activity functions.

Low Mass - Fiducial Resolution Simulations

Here we repeat the previous analysis but consider higher resolution (particle resolution) versions. We first highlight that the activity functions of the same models differ between the low and fiducial resolution simulations. While the fiducial resolution models exhibit steeper BH growth for $t < 600\,\text{Myr}$, the low resolution models show major outbursts in activity (BH accretion & star formation) after the core merger (Wurster and Thacker 2013b). Also lower particle resolution simulations yield a higher final BH mass (Wurster and Thacker 2013b). For a detailed comparison of the low and fiducial resolution simulations see Wurster and Thacker (2013a,b). In the PNK0505 model, such differences are reflected in the AF of the low resolution simulations as an increase in activity at high Eddington ratios ($\lambda \sim 1$) and therefore a low-λ tail that extends to lower Eddington ratios (the feedback associated with accretion at higher Eddington ratio results in the lower accretion tail). The PNK0505$_l$ model also shows a less prominent low-λ peak at $\lambda \sim 7 \times 10^{-3}$. On the other hand, the WT$_l$ model shows a low-λ cut-off at higher Eddington ratios, when compared to the fiducial (particle resolution) runs, which is consistent with more feedback energy being returned to the surrounding gas (Wurster and Thacker 2013b). The AF of the WT$_l$ model also shows less activity at high Eddington ratios.

We compare the AFs of the fiducial resolution models using low and high mass galaxies in figure 4.19. The low mass simulations were evolved for $1.2\,\text{Gyr}$ only because of time constraints. Note that stopping the simulation $300\,\text{Myr}$ early will only reduce AGN activity at low Eddington ratios as the Eddington ratio after $1.2\,\text{Gyr}$ remains at low values ($\lambda \in [10^{-5} : 10^{-4}]$).

Discussing the results of the PNK0505 model: The AF of the low mass simulation qualitatively agrees with a Schechter function for $\lambda > 10^{-2}$. The activity sharply decreases for $\lambda < 10^{-2}$ until a low-λ cut-off at $\lambda \sim 2 \times 10^{-3}$. Conversely, the AF of the high mass (Milky Way like galaxies) simulation shows two peaks at $\lambda \sim 10^{-1}$ and $\lambda \sim 5 \times 10^{-3}$ with a monotonically decreasing low-λ tail for $\lambda \in [10^{-4} : 5 \times 10^{-3}]$. The discrepancy in the AFs of the low and high mass galaxies at low λ (low λ tail
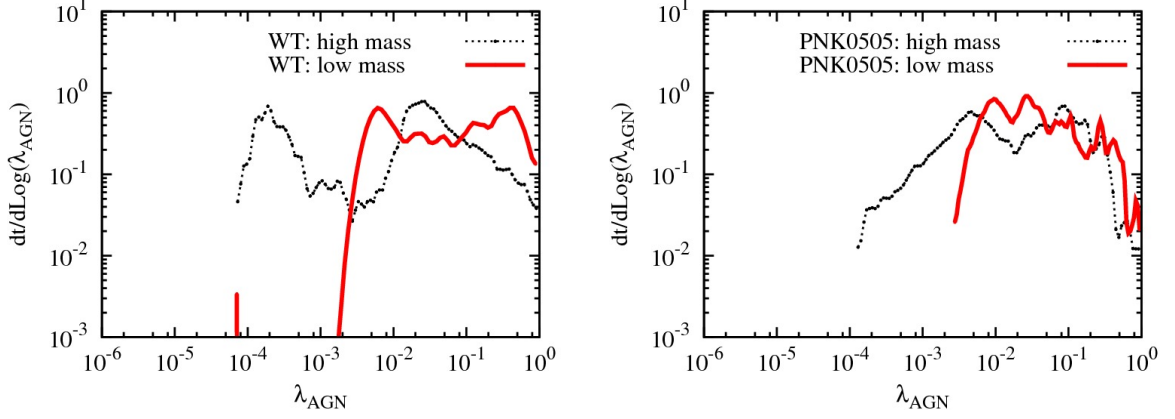
Figure 4.19: The AFs produced by fiducial resolution simulations with low mass ICs ($\lambda_m = 0.1$) using the WT model (left) and PNK0505 model (right) compared to simulations with unscaled Milky Way like ICs. The low mass PNK0505 simulation qualitatively reproduces the observed Schechter like AF for $\lambda > 10^{-2}$.

v.s. sharp cut-off) is consistent with the low mass simulations having more frequent accretion; therefore the tail produced by mass transfer from the ADP onto the BH is constantly interrupted by accretion (see the discussion in the low-mass, low-resolution simulations). The peak at $\lambda \sim 10^{-2}$ is consistent with the Eddington ratio showing little variation from said value after the merger, specifically $t > 850\,\mathrm{Myr}$, which is also consistent with the BH residing in a slowly changing environment. The sharp decrease in activity at high-λ ($\lambda \sim 3 \times 10^{-1}$) reflects the intensity of the feedback creating a void around the BH in the high mass simulations which causes lower densities around the BH.

The low mass simulations using the WT model show a flat AF for $\lambda > 5 \times 10^{-3}$. The increase in activity at high Eddington ratios ($\lambda \sim 1$) in the low mass simulation is consistent with the increased BH growth during the merger. The WT model also exhibits less energetic feedback than the PNK model which allows a smooth transition (recall the feedback in the PNK model caused a sharp drop in the accretion rates) in the accretion rate between the merger and post merger epochs. Such a transition extends the AF to intermediate Eddington ratios ($\lambda \sim 10^{-2}$) with semi-constant activity. The sharp drop in the AF of the low mass simulation at $\lambda \sim 5 \times 10^{-3}$ is partly due to not extending the simulation to $1.5\,\mathrm{Gyr}$, as well as the low feedback energies being returned to the system, and the lower cooling time in the low mass

97

simulations causing the BH to accrete at intermediate Eddington ratios. Note that although not visible in the graph, the AGN in the low mass simulation is active at low Eddington ratios ($\lambda \in [10^{-5} : 10^{-4}]$). However, the time spent at low Eddington ratios is extremely short yielding values of $\frac{\mathrm{d}t}{\mathrm{d}\log(\lambda_{AGN})} \sim 10^{-5}$.

Figure 4.20 shows the AF of low and high mass fiducial resolution simulations binned by BH mass. The AFs throughout the evolution of both low and high mass galaxies show similar trends for each of the PNK0505 and WT models. During the passive stages of the evolution the BH accretes at consistently lower Eddington ratios causing the AF to shift to lower Eddington ratios with an exception being the core merger.

Figure 4.20: The mass dependent AFs produced by fiducial resolution simulations with low mass ICs (right) using the WT (top) and PNK0505 (bottom) models compared to simulations with unscaled Milky Way like ICs (left). Note that the activity function represented by a delta function at $\lambda = 1$ for some intermediate mass bins during are not shown in this figure.

Similar to the low resolution (particle resolution) simulations, the fiducial resolution simulations, at both high and low galaxy mass, yield activity functions that shift to lower Eddington ratios during the passive stages of the evolution indicating a weak dependence of the AF on the BH or galaxy mass and a strong dependence on

the evolutionary state of the system. Figures 4.21 and 4.22 indicate an obvious shift to low Eddington ratios during the passive stages of the evolution (high $\frac{M_{BH}}{M_{BH,0}}$).

Log(M_{BH}/$M_{BH,0}$) $\in$ [0.5:1.0]	....	Log(M_{BH}/$M_{BH,0}$) $\in$ [2.0:2.5]	....
Log(M_{BH}/$M_{BH,0}$) $\in$ [1.0:1.5]	————	Log(M_{BH}/$M_{BH,0}$) $\in$ [2.5:3.0]	....
Log(M_{BH}/$M_{BH,0}$) $\in$ [1.5:2.0]	....	Log(M_{BH}/$M_{BH,0}$) $\in$ [2.5:3.0]	....
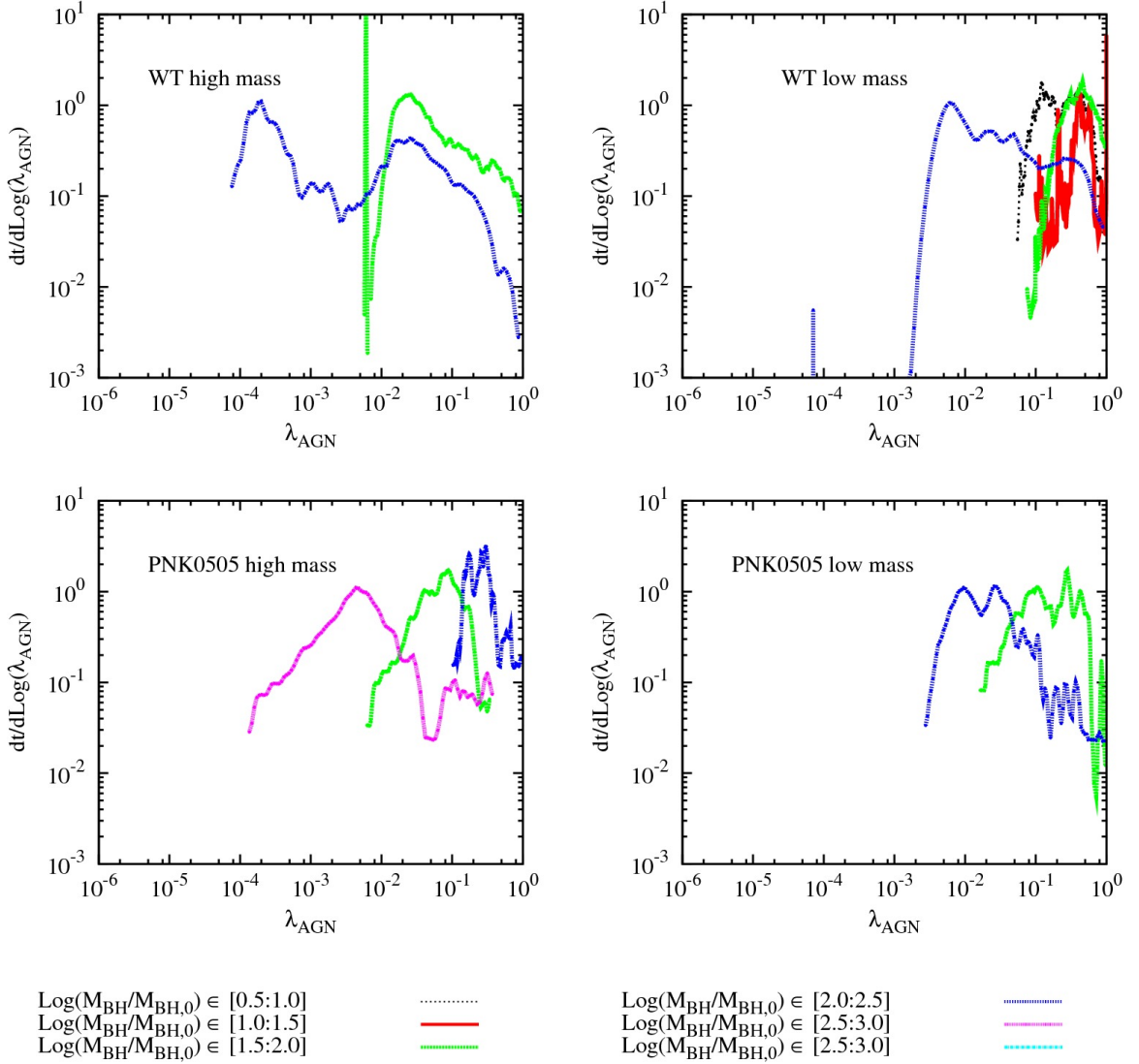
Figure 4.21: The AFs produced by fiducial resolution simulations with low mass ICs (right) using the WT model (top) and PNK0505 model (bottom) compared to simulations with unscaled Milky Way like ICs (left). Here the AFs are plotted in different $M_{BH}/M_{BH,0}$ bins which is an indicator of the evolutionary stage. The activity function is independent of the overall galaxy mass for this resolution while it shows strong dependence on the evolutionary stage. Note that the activity function represented by a delta function at $\lambda = 1$ for some intermediate mass bins during are not shown in this figure.
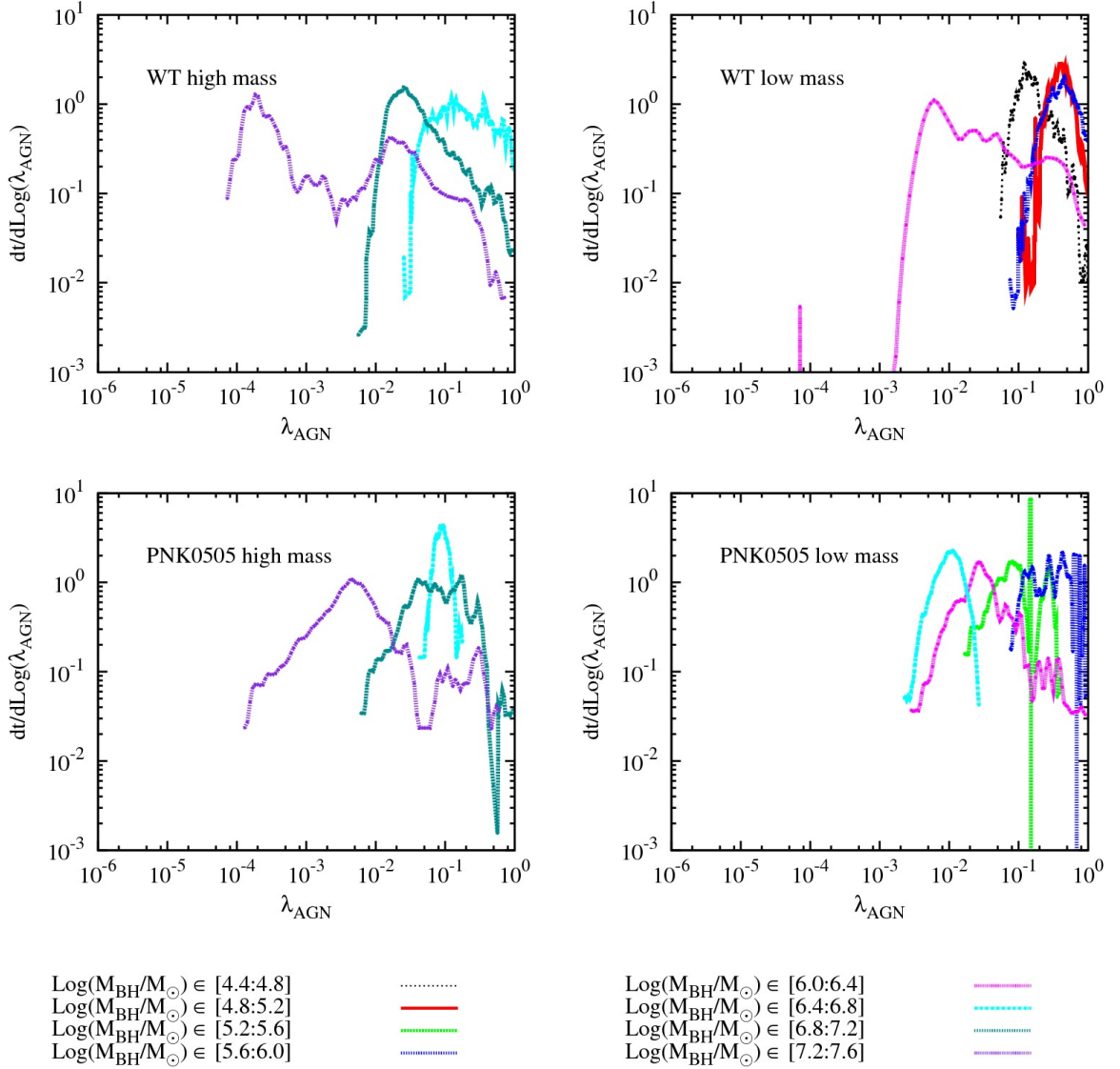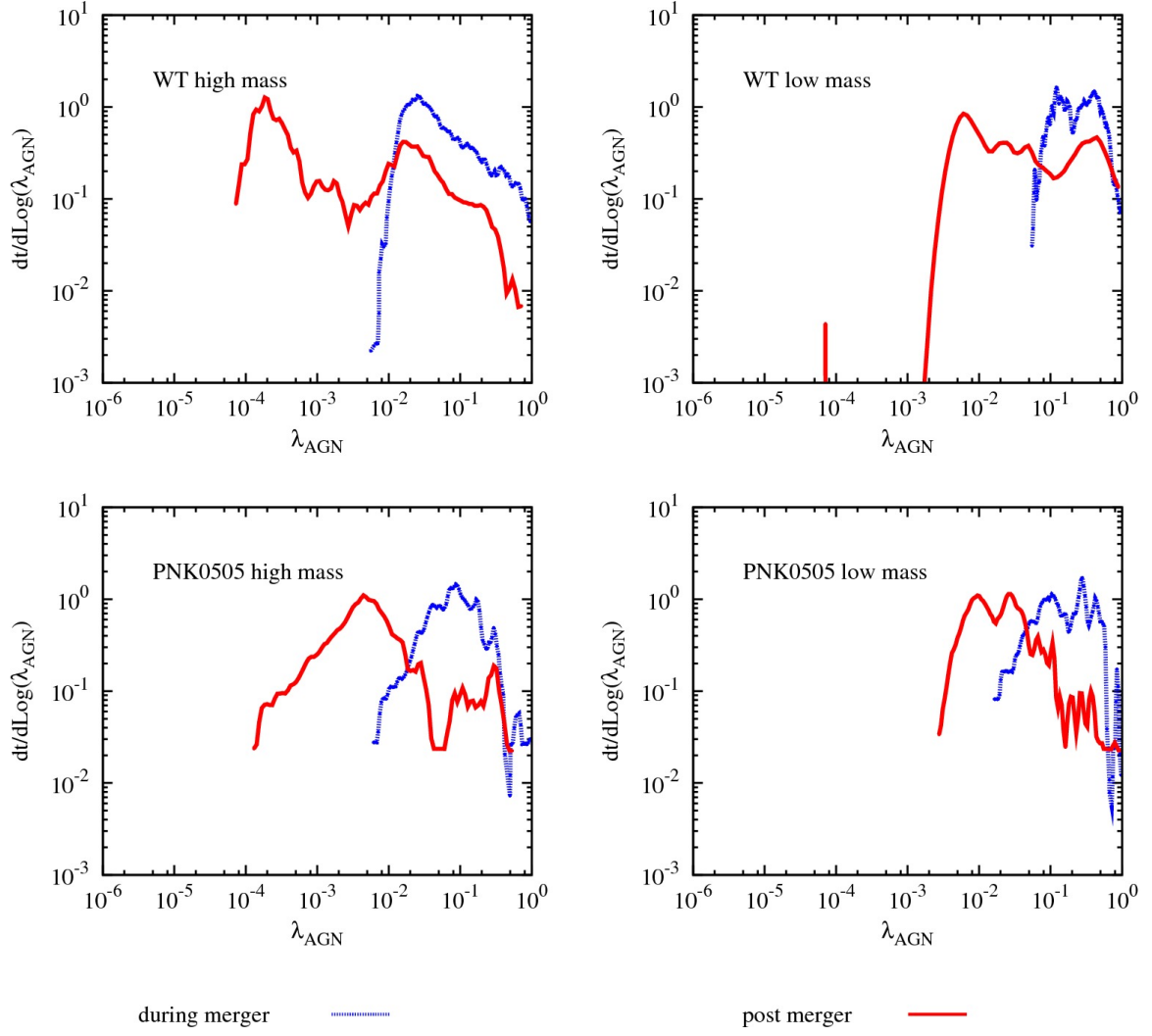
Figure 4.22: The AFs produced by fiducial resolution simulations with low mass ICs (right) using the WT model (top) and PNK0505 model (bottom) compared to simulations with unscaled Milky Way like ICs (left). The AF is shown during different stages of the evolution indicating a strong dependence of the AF on the evolutionary state of the system.

Chapter 5

CONCLUSIONS AND FUTURE WORK

5.1 CONCLUSIONS

This work focused on further understanding the predictions of simulated black hole (BH) models in N-body, hydrodynamical galaxy merger simulations. This helps uncover the shortcomings of the models when compared with various observational constraints such as the quasar luminosity function. Improving the models is key if we are to better understand the underlying physics of essential processes in galaxy evolution such as BH accretion and AGN feedback.

The analysis presented in this work includes numerical simulations using the following seven BH evolution and feedback models: BS, DQM, HPNK, ONB, PNK, SDH, and WT (see §3); all of which were simulated, at both low and fiducial resolution, using the same numerical code (HYDRA_OMP), ICs[1], star formation and stellar feedback algorithms. Note that all the BH models were developed in previous studies and were implemented in HYDRA_OMP by Wurster and Thacker (2013a,b) and Thacker et al. (2014). The analysis we present, includes an examination of the differences resulting from numerical effects as well as changes in the ICs. However, our primary conclusions pertain to the activity functions produced by the various models and their dependence on free parameters, such as the accretion radius and viscous timescales in the PNK model or the α parameter in the modified Bondi accretion rate, as well as the mass of the merging galaxies.

Before listing our conclusions, we caution that some are based upon low resolution simulations which produce coarse and noisy results. Although, noisy results can hide some of the underlying physics, low resolution simulations can still provide

---

[1]The same ICs were used at a given resolution except for the simulations of the low mass galaxies.

a good first order test of the models which can be considered an upper limit for the variations in the fiducial resolution simulations. That said, it is worth emphasizing that even our low resolution models have significantly better mass resolution than the current generation of cosmological simulations such as the Illustris Collaboration (Vogelsberger et al. 2014; Genel et al. 2014) and the EAGLE project (Schaye et al. 2015). The primary conclusions are as follows.

i. We tested differences amongst different runs of the same simulation using WT_l and $PNK0505_l$. These variations in the final results are induced by numerical artifacts such as rounding errors, and unavoidable truncation errors. The BH mass, SFR, and accretion rate vary within 5%, 92%, and 43% from their respective averages. The instantaneous and intermediate values of the SFR and BH mass show more variation. It is worth noting the difficulty in matching intermediate properties in the evolution of non-linear systems such as galaxy mergers. On the other hand, the activity functions of different runs (with the same ICs) agree well for high Eddington ratios ($\lambda > 10^{-2}$). Because the low λ tail of the AF is subject to changes due to the chaotic BH neighborhood, different runs may differ at the low λ end. However, all AFs produced by the different runs agree qualitatively.

ii. We also tested the effects of changing the rotational orientation of the gas component in low resolution simulations using the the WT_l model. Changing the rotational orientation of the gas component of the galaxies causes changes in the angular momentum of the remnant. Because of the self regulation of the system, the final BH mass and SFR vary by less than 60% from their respective averages. However, changing the angular momentum of the gas component has some distinct effects on the activity functions produced by such systems. The systems with lower angular momentum show increasing activity at high λ which causes the low λ tail to extend to lower Eddington ratios (due to feedback).

iii. The initial (seed) BH mass, plays a key role in the evolution of the system. Increasing the BH seed mass manifests as a change in the initial accretion rate and the feedback energy returned to the system. However, the self-regulated system yields final BH masses, SFRs and accretion rates that vary within less than 37% from their respective averages. Increasing the BH seed mass does, however, produce significant differences in the activity function: The high λ peak in systems with higher BH seed masses is shifted to lower Eddington ratios.

iv. The simulations used in this study, and many others, often use galaxies that are aligned in one plane. This is not the case for all observed galaxies. Therefore checking that the results are largely independent of galaxy orientation is key. We have found that increasing the inclination of the galaxies causes a slight delay in the merger time, but the final BH mass, SFR and accretion rates vary within 15% of their respective averages. The activity function at high Eddington ratios remains unchanged as it is governed by the high accretion epochs. However, the intermediate and low λ activity is affected by the different properties of the remnant (i.e. different morphology, angular momentum). Thus while intermediate states may differ, final states are broadly the same.

v. Testing the differences due to ICs with different initial random seeds is also important in numerical work. Small changes in the ICs should not yield significant differences in the final results. Changing the IC random seed induced variations within a factor of 2 in the final BH mass (within 5%), final SFR (within 93%) and final accretion rate (within 70%). The activity functions produced by the different simulations (with different seeds) vary only for low Eddington ratios ($\lambda < 3 \times 10^{-3}$).

vi. None of the seven models produce the activity function inferred from observations when calculated over the multiple stages of the simulation. The models

produce a flat distribution (BS), a lognormal distribution (WT, DQM), a lognormal distribution with a skewed high-λ tail (SDH), or an activity function with an increasing low-λ tail and a peak at high Eddington ratios (PNK, HPNK).

vii. Some models produce a Schechter like activity function that agrees (qualitatively) with that inferred from observations during the passive stages of the evolution. This could be an indicator of the sensitivity of the activity function to the gas fraction.

viii. Reducing the mass of the galaxy has a visible impact on the activity function (integrated over different evolutionary stages). The activity function produced by the low mass galaxies using the WT model is flat for $\lambda > 10^{-2}$. The activity function produced by the low mass galaxies using the PNK0505 model show a Schechter like activity function. This, combined with the AF shifting to consistently lower Eddington ratios during the passive stages of the evolution (for both low and high mass galaxies at both low and high resolution), could also be considered as an indicator of the sensitivity of the activity function to the gas fraction and gas mass.

ix. We have demonstrated that the models reproduce the observed (Kauffmann and Heckman 2009; Hopkins and Hernquist 2009) mass-invariant activity functions: The AF is independent of the overall galaxy mass. Instead the AF is a function of the evolutionary state of the system.

x. The power spectrum of the Eddington ratio follows a $1/f^2$ power law for all models which is consistent with the superposition of a decay in the Eddington ratio (diminishing gas reservoir and increasing BH mass) and random noise (stochastic accretion). The ONB model deposits feedback energy into the halo and therefore does not affect the immediate neighborhood of the BH. Hence, ONB follows the $1/f^2$ power law (with minimal deviation) with a peak at high frequency due to the chaotic neighborhood as well as a flat, white noise like, power spectrum at low frequencies ($f \sim 1/1.5\,\mathrm{Gyr}$). Models that return feedback as heat, show an

increase in the power for $f \in [0.3 : 25]\,\mathrm{Myr}^{-1}$ while still following a $1/f^2$ power law which may be attributed to the cooling timescales. They follow a power spectrum of brown noise with driving terms (heating and cooling). On the other hand, models returning feedback kinetically, show some peaks in the power at intermediate frequencies which can be related to the re-collapse of the gas after being ejected due to feedback.

xi. Modifying the dependence of the modified Bondi accretion law used to calculate the accretion rate can have some significant effects on the activity function. Using a higher dependence on density, allows more activity at Eddington luminosities, as well as more accretion at intermediate λ and extends the low λ tail to lower Eddington ratios. However, despite considering a number of possible accretion models, this still does not produce a monotonically decreasing low λ tail as in a Schechter function.

xii. The PNK model has two main free parameters: the radius of accretion and the viscous timescale. Changing the radius of accretion does not have a significant impact on the AF. However, decreasing the viscous timescale allows material to accrete faster onto the BH, therefore increasing the time spent at Eddington luminosities. Because of the associated feedback, high accretion rates cause the low λ tail to extend to lower Eddington ratios.

5.2 FUTURE WORK

This work has demonstrated the dependence of the activity function on the evolutionary stage of the merger as well as galactic mass and other properties (i.e. rotational orientation, BH mass). However, further research is required to draw conclusions about the activity functions in a cosmological context and extend the analysis to all BH models.

The simulations in this study used merging Milky-Way like galaxies in an isolated environment. A more realistic approach would require simulating a catalogue of

galaxies in a cosmological context. The galaxies in such a simulation will be subject to various environmental effects (e.g. tidal effects, stripping effects, minor mergers) which are suggested to be a cause of low luminosity AGN (e.g. Ellison et al. 2015). Moreover, performing a similar analysis using a cosmological simulation provides a variety of galaxy types with different properties. This will allow the comparison of instantaneous AGN populations (quasar luminosity function) instead of time evolution of one AGN (activity function). Although current efforts, such as the Illustris Collaboration (Vogelsberger et al. 2014; Genel et al. 2014) and the EAGLE project (Schaye et al. 2015), simulate catalogues of galaxies in a cosmological context, they lack the resolution (spatial and mass resolution) to study AGN evolution and feedback in detail; even the low resolution models that were used in this study have significantly better mass resolution (> 5 times) than the EAGLE and Illustris simulations. With such coarse resolution, higher levels of sub-resolution (sub-grid) modeling are required and the small resolution physics that governs BH accretion and feedback cannot be resolved.

One can also enhance this study by altering the ICs to include halo substructure. Including substructure will allow depositing small packets of cold gas[2] into the galactic core inducing accretion at low Eddington ratios. DM satellites can also create density fluctuations (e.g. Dubinski et al. 2008, Gauthier et al. 2006) in the galactic core which may have an effect on AGN accretion. It is clearly the case that accurate simulation of the numerous factors that contribute to BH accretion is a challenge that will remain for some considerable time.

The Eddington ratio power spectrum of the different models show some important features (i.e. peaks at distinct frequencies, $1/f^2$ power law). Further analysis is required to unveil the underlying physics. The effects of cooling on the power spectrum should be further investigated by varying the cooling rates (increase/decrease cooling rates) as well as turning cooling off. One can also examine the temperature

---

[2]The gas can be either stripped from the DM halos or accreted into the core after the destruction of the DM substructure. D'Onghia et al. (2010) showed that dynamical processes can destroy dark matter substructure in the inner regions of the galactic halo.

dependent gas fraction in the BH's neighborhood which will further help understand the effects of cooling on the environment. On the other hand, the source of the peaks in the power spectrum of the kinetic feedback models can be investigated by varying the feedback mechanism (heating, kinetic, or halo heating) in a given model. Also, tracking the in/out-flowing gas flux in spherical shells centered at the BH will help understand the dynamics of the inflow/outflow of gas. The aforementioned analysis will enhance our understanding of the relationship between the feedback mechanisms and some features in the Eddington ratio power spectrum.

In spite of the current progress, important questions regarding BH accretion and AGN feedback remain unanswered. The details of BH accretion, the underlying physics, and the processes contributing to accretion are not fully understood yet. Moreover, it is still unclear whether the current AGN models properly represent the impact of AGN feedback. Gabor and Bournaud (2014) suggest that high resolution simulations including AGN feedback produce notably different results because feedback energy escapes along low density gradients above and below the galactic disc. The results presented by Gabor and Bournaud (2014) imply that the current models over-estimate the actual impact of AGN feedback in the galactic medium, which may be the case. Further research is required to constrain the current BH evolution and AGN feedback models and better model the effects of AGN feedback and the related processes.

Bibliography

Abadi, M. G., Moore, B., and Bower, R. G. (1999). Ram pressure stripping of spiral galaxies in clusters. MNRAS, 308:947–954.

Alexander, D. M. and Hickox, R. C. (2012). What drives the growth of black holes? New A Rev., 56:93–121.

Aller, M. C. and Richstone, D. O. (2007). Host Galaxy Bulge Predictors of Super-massive Black Hole Mass. ApJ, 665:120–156.

Barnes, J. and Hut, P. (1986). A hierarchical O(N log N) force-calculation algorithm. Nature, 324:446–449.

Barnes, J. E. and Hernquist, L. (1996). Transformations of Galaxies. II. Gasdynamics in Merging Disk Galaxies. ApJ, 471:115.

Barnes, J. E. and Hernquist, L. E. (1991). Fueling starburst galaxies with gas-rich mergers. ApJ, 370:L65–L68.

Barrow, J. D. and Saich, P. (1993). Growth of large-scale structure with a cosmological constant. MNRAS, 262:717–725.

Bauer, F. E., Alexander, D. M., Brandt, W. N., Schneider, D. P., Treister, E., Horn-schemeier, A. E., and Garmire, G. P. (2004). The Fall of Active Galactic Nuclei and the Rise of Star-forming Galaxies: A Close Look at the Chandra Deep Field X-Ray Number Counts. AJ, 128:2048–2065.

Begelman, M. C., Blandford, R. D., and Rees, M. J. (1984). Theory of extragalactic radio sources. *Reviews of Modern Physics*, 56:255–351.

Begelman, M. C. and Rees, M. J. (1978). The fate of dense stellar systems. MNRAS, 185:847–860.

Begelman, M. C., Volonteri, M., and Rees, M. J. (2006). Formation of supermassive black holes by direct collapse in pre-galactic haloes. MNRAS, 370:289–298.

Behroozi, P. S., Wechsler, R. H., and Conroy, C. (2013). The Average Star Formation Histories of Galaxies in Dark Matter Halos from z = 0-8. ApJ, 770:57.

Bell, E. F., Papovich, C., Wolf, C., Le Floc'h, E., Caldwell, J. A. R., Barden, M., Egami, E., McIntosh, D. H., Meisenheimer, K., Pérez-González, P. G., Rieke, G. H., Rieke, M. J., Rigby, J. R., and Rix, H.-W. (2005). Toward an Understanding of the Rapid Decline of the Cosmic Star Formation Rate. ApJ, 625:23–36.

Bondi, H. (1952). On spherically symmetrical accretion. MNRAS, 112:195–+.

Bondi, H. and Hoyle, F. (1944). On the mechanism of accretion by stars. MNRAS, 104:273–+.

Booth, C. M. and Schaye, J. (2009). Cosmological simulations of the growth of supermassive black holes and feedback from active galactic nuclei: method and tests. MNRAS, 398:53–74. (BS09).

Bower, R. G., Benson, A. J., Malbon, R., Helly, J. C., Frenk, C. S., Baugh, C. M., Cole, S., and Lacey, C. G. (2006). Breaking the hierarchy of galaxy formation. MNRAS, 370:645–655.

Buff, J. and McCray, R. (1974). Accretion Flows in Galactic X-Ray Sources. Optically Thin Spherically Symmetric Model. ApJ, 189:147–156.

Castor, J. I., Abbott, D. C., and Klein, R. I. (1975). Radiation-driven winds in Of stars. ApJ, 195:157–174.

Cavaliere, A. and Fusco-Femiano, R. (1976). X-rays from hot plasma in clusters of galaxies. A&A, 49:137–144.

Ciotti, L. and Ostriker, J. P. (2001). Cooling Flows and Quasars. II. Detailed Models of Feedback-modulated Accretion Flows. ApJ, 551:131–152.

Ciotti, L. and Ostriker, J. P. (2007). Radiative Feedback from Massive Black Holes in Elliptical Galaxies: AGN Flaring and Central Starburst Fueled by Recycled Gas. ApJ, 665:1038–1056.

Conroy, C. and White, M. (2013). A Simple Model for Quasar Demographics. ApJ, 762:70.

Couchman, H. M. P. (1991). Mesh-refined P3M - A fast adaptive N-body algorithm. ApJ, 368:L23–L26.

Couchman, H. M. P., Thomas, P. A., and Pearce, F. R. (1995). Hydra: an Adaptive-Mesh Implementation of P 3M-SPH. ApJ, 452:797.

Courteau, S., Dutton, A. A., van den Bosch, F. C., MacArthur, L. A., Dekel, A., McIntosh, D. H., and Dale, D. A. (2007). Scaling Relations of Spiral Galaxies. ApJ, 671:203–225.

Cowie, L. L., Ostriker, J. P., and Stark, A. A. (1978). Time-dependent spherically symmetric accretion onto compact X-ray sources. ApJ, 226:1041–1062.

Cowie, L. L., Songaila, A., Hu, E. M., and Cohen, J. G. (1996). New Insight on Galaxy Formation and Evolution From Keck Spectroscopy of the Hawaii Deep Fields. AJ, 112:839.

Dasyra, K. M., Tacconi, L. J., Davies, R. I., Genzel, R., Lutz, D., Naab, T., Burkert, A., Veilleux, S., and Sanders, D. B. (2006). Dynamical Properties of Ultraluminous Infrared Galaxies. I. Mass Ratio Conditions for ULIRG Activity in Interacting Pairs. ApJ, 638:745–758.

Debuhr, J., Quataert, E., and Ma, C.-P. (2011). The growth of massive black holes in galaxy merger simulations with feedback by radiation pressure. MNRAS, 412:1341–1360. (DQM11).

Dekel, A. and Birnboim, Y. (2006). Galaxy bimodality due to cold flows and shock heating. MNRAS, 368:2–20.

Dekel, A., Devor, J., and Hetzroni, G. (2003). Galactic halo cusp-core: tidal compression in mergers. MNRAS, 341:326–342.

Diemand, J., Kuhlen, M., and Madau, P. (2007). Formation and Evolution of Galaxy Dark Matter Halos and Their Substructure. ApJ, 667:859–877.

D'Onghia, E., Springel, V., Hernquist, L., and Keres, D. (2010). Substructure Depletion in the Milky Way Halo by the Disk. ApJ, 709:1138–1147.

Dressler, A. (1989). Observational Evidence for Supermassive Black Holes. In Osterbrock, D. E. and Miller, J. S., editors, *Active Galactic Nuclei*, volume 134 of *IAU Symposium*, page 217.

Dubinski, J., Gauthier, J.-R., Widrow, L., and Nickerson, S. (2008). Spiral and Bar Instabilities Provoked by Dark Matter Satellites. In Funes, J. G. and Corsini, E. M., editors, *Formation and Evolution of Galaxy Disks*, volume 396 of *Astronomical Society of the Pacific Conference Series*, page 321.

Ellison, S. L., Patton, D. R., and Hickox, R. C. (2015). Galaxy pairs in the Sloan Digital Sky Survey - XII. The fuelling mechanism of low-excitation radio-loud AGN. MNRAS, 451:L35–L39.

Fabian, A. C. (2012). Observational Evidence of Active Galactic Nuclei Feedback. ARA&A, 50:455–489.

Farouki, R. and Shapiro, S. L. (1981). Computer simulations of environmental influences on galaxy evolution in dense clusters. II - Rapid tidal encounters. ApJ, 243:32–41.

Feldmann, R. and Mayer, L. (2015). The Argo simulation - I. Quenching of massive galaxies at high redshift as a result of cosmological starvation. MNRAS, 446:1939–1956.

Ferrarese, L. and Merritt, D. (2000). A Fundamental Relation between Supermassive Black Holes and Their Host Galaxies. ApJ, 539:L9–L12.

Fioc, M. and Rocca-Volmerange, B. (1997). PEGASE: a UV to NIR spectral evolution model of galaxies. Application to the calibration of bright galaxy counts. A&A, 326:950–962.

Gabor, J. M. and Bournaud, F. (2013). Simulations of supermassive black hole growth in high-redshift disc galaxies. MNRAS, 434:606–620.

Gabor, J. M. and Bournaud, F. (2014). Active galactic nuclei-driven outflows without immediate quenching in simulations of high-redshift disc galaxies. MNRAS, 441:1615–1627.

Gauthier, J.-R., Dubinski, J., and Widrow, L. M. (2006). Substructure around M31: Evolution and Effects. ApJ, 653:1180–1193.

Gebhardt, K., Bender, R., Bower, G., Dressler, A., Faber, S. M., Filippenko, A. V., Green, R., Grillmair, C., Ho, L. C., Kormendy, J., Lauer, T. R., Magorrian, J., Pinkney, J., Richstone, D., and Tremaine, S. (2000). A Relationship between Nuclear Black Hole Mass and Galaxy Velocity Dispersion. ApJ, 539:L13–L16.

Genel, S., Vogelsberger, M., Springel, V., Sijacki, D., Nelson, D., Snyder, G., Rodriguez-Gomez, V., Torrey, P., and Hernquist, L. (2014). Introducing the Illustris project: the evolution of galaxy populations across cosmic time. MNRAS, 445:175–200.

Gillessen, S., Eisenhauer, F., Trippe, S., Alexander, T., Genzel, R., Martins, F., and Ott, T. (2009). Monitoring Stellar Orbits Around the Massive Black Hole in the Galactic Center. ApJ, 692:1075–1109.

Gilli, R., Comastri, A., and Hasinger, G. (2007). The synthesis of the cosmic X-ray background in the Chandra and XMM-Newton era. A&A, 463:79–96.

Gingold, R. A. and Monaghan, J. J. (1977). Smoothed particle hydrodynamics - Theory and application to non-spherical stars. MNRAS, 181:375–389.

Gingold, R. A. and Monaghan, J. J. (1982). Kernel estimates as a basis for general particle methods in hydrodynamics. *Journal of Computational Physics*, 46:429–453.

Greene, J. E. and Ho, L. C. (2007). The Mass Function of Active Black Holes in the Local Universe. ApJ, 667:131–148.

Gunn, J. E. and Gott, III, J. R. (1972). On the Infall of Matter Into Clusters of Galaxies and Some Effects on Their Evolution. ApJ, 176:1.

Häring, N. and Rix, H.-W. (2004). On the Black Hole Mass-Bulge Mass Relation. ApJ, 604:L89–L92.

Hasinger, G., Miyaji, T., and Schmidt, M. (2005). Luminosity-dependent evolution of soft X-ray selected AGN. New Chandra and XMM-Newton surveys. A&A, 441:417–434.

Heckman, T. M., Kauffmann, G., Brinchmann, J., Charlot, S., Tremonti, C., and White, S. D. M. (2004). Present-Day Growth of Black Holes and Bulges: The Sloan Digital Sky Survey Perspective. ApJ, 613:109–118.

Hernquist, L. (1989). Tidal triggering of starbursts and nuclear activity in galaxies. Nature, 340:687–691.

Hernquist, L. and Katz, N. (1989). TREESPH - A unification of SPH with the hierarchical tree method. ApJS, 70:419–446.

Hickox, R. C., Jones, C., Forman, W. R., Murray, S. S., Brodwin, M., Brown, M. J. I., Eisenhardt, P. R., Stern, D., Kochanek, C. S., Eisenstein, D., Cool, R. J., Jannuzi, B. T., Dey, A., Brand, K., Gorjian, V., and Caldwell, N. (2007). A Large Population of Mid-Infrared-selected, Obscured Active Galaxies in the Boötes Field. ApJ, 671:1365–1387.

Hickox, R. C., Mullaney, J. R., Alexander, D. M., Chen, C.-T. J., Civano, F. M., Goulding, A. D., and Hainline, K. N. (2014). Black Hole Variability and the Star Formation-Active Galactic Nucleus Connection: Do All Star-forming Galaxies Host an Active Galactic Nucleus? ApJ, 782:9.

Hobbs, A., Power, C., Nayakshin, S., and King, A. R. (2012). Modelling supermassive black hole growth: towards an improved sub-grid prescription. MNRAS, 421:3443–3449.

Hockney, R. W. and Eastwood, J. W. (1981). *Computer Simulation Using Particles.*

Hopkins, A. M. (2004). On the Evolution of Star-forming Galaxies. ApJ, 615:209–221.

Hopkins, P. F. and Hernquist, L. (2006). Fueling Low-Level AGN Activity through Stochastic Accretion of Cold Gas. ApJS, 166:1–36.

Hopkins, P. F. and Hernquist, L. (2009). Quasars Are Not Light Bulbs: Testing Models of Quasar Lifetimes with the Observed Eddington Ratio Distribution. ApJ, 698:1550–1569.

Hopkins, P. F., Hernquist, L., Cox, T. J., Di Matteo, T., Martini, P., Robertson, B., and Springel, V. (2005a). Black Holes in Galaxy Mergers: Evolution of Quasars. ApJ, 630:705–715.

Hopkins, P. F., Hernquist, L., Cox, T. J., Di Matteo, T., Robertson, B., and Springel, V. (2005b). Luminosity-dependent Quasar Lifetimes: A New Interpretation of the Quasar Luminosity Function. ApJ, 630:716–720.

Hopkins, P. F., Hernquist, L., Cox, T. J., Di Matteo, T., Robertson, B., and Springel, V. (2006a). A Unified, Merger-driven Model of the Origin of Starbursts, Quasars, the Cosmic X-Ray Background, Supermassive Black Holes, and Galaxy Spheroids. ApJS, 163:1–49.

Hopkins, P. F., Hernquist, L., Cox, T. J., and Kereš, D. (2008). A Cosmological Framework for the Co-Evolution of Quasars, Supermassive Black Holes, and Elliptical Galaxies. I. Galaxy Mergers and Quasar Activity. ApJS, 175:356–389.

Hopkins, P. F., Hernquist, L., Cox, T. J., Robertson, B., Di Matteo, T., and Springel, V. (2006b). The Evolution in the Faint-End Slope of the Quasar Luminosity Function. ApJ, 639:700–709.

Hopkins, P. F., Hernquist, L., Cox, T. J., Robertson, B., and Krause, E. (2007a). A Theoretical Interpretation of the Black Hole Fundamental Plane. ApJ, 669:45–66.

Hopkins, P. F., Hernquist, L., Cox, T. J., Robertson, B., and Krause, E. (2007b). An Observed Fundamental Plane Relation for Supermassive Black Holes. ApJ, 669:67–73.

Hopkins, P. F., Lidz, A., Hernquist, L., Coil, A. L., Myers, A. D., Cox, T. J., and Spergel, D. N. (2007c). The Co-Formation of Spheroids and Quasars Traced in their Clustering. ApJ, 662:110–130.

Hopkins, P. F. and Quataert, E. (2010). How do massive black holes get their gas? MNRAS, 407:1529–1564.

Hoyle, F. and Lyttleton, R. A. (1939). The effect of interstellar matter on climatic variation. *PCPS*, 35:405–+.

Hubble, E. P. (1929). A spiral nebula as a stellar system, Messier 31. ApJ, 69:103–158.

Inoue, Y., Inoue, S., Kobayashi, M. A. R., Makiya, R., Niino, Y., and Totani, T. (2013). Extragalactic Background Light from Hierarchical Galaxy Formation: Gamma-Ray Attenuation up to the Epoch of Cosmic Reionization and the First Stars. ApJ, 768:197.

Ishibashi, W. and Fabian, A. C. (2012). Active galactic nucleus feedback and triggering of star formation in galaxies. MNRAS, 427:2998–3005. (IF12).

Jakobsen, P., Jansen, R. A., Wagner, S., and Reimers, D. (2003). Caught in the act: A helium-reionizing quasar near the line of sight to Q0302-003. A&A, 397:891–898.

Katz, N. (1992). Dissipational galaxy formation. II - Effects of star formation. ApJ, 391:502–517.

Kauffmann, G. and Heckman, T. M. (2009). Feast and Famine: regulation of black hole growth in low-redshift galaxies. MNRAS, 397:135–147.

Kauffmann, G., Heckman, T. M., Tremonti, C., Brinchmann, J., Charlot, S., White, S. D. M., Ridgway, S. E., Brinkmann, J., Fukugita, M., Hall, P. B., Ivezić, Ž., Richards, G. T., and Schneider, D. P. (2003). The host galaxies of active galactic nuclei. MNRAS, 346:1055–1077.

Kaufmann, T., Mayer, L., Wadsley, J., Stadel, J., and Moore, B. (2007). Angular momentum transport and disc morphology in smoothed particle hydrodynamics simulations of galaxy formation. MNRAS, 375:53–67.

Kawata, D., Gibson, B. K., Barnes, D. J., Grand, R. J. J., and Rahimi, A. (2014). Numerical simulations of bubble-induced star formation in dwarf irregular galaxies with a novel stellar feedback scheme. MNRAS, 438:1208–1222.

Kennicutt, Jr., R. C. (1998). The Global Schmidt Law in Star-forming Galaxies. ApJ, 498:541.

Kocevski, D. D., Faber, S. M., Mozena, M., Koekemoer, A. M., Nandra, K., Rangel, C., Laird, E. S., Brusa, M., Wuyts, S., Trump, J. R., Koo, D. C., Somerville, R. S., Bell, E. F., Lotz, J. M., Alexander, D. M., Bournaud, F., Conselice, C. J., Dahlen, T., Dekel, A., Donley, J. L., Dunlop, J. S., Finoguenov, A., Georgakakis, A., Giavalisco, M., Guo, Y., Grogin, N. A., Hathi, N. P., Juneau, S., Kartaltepe, J. S., Lucas, R. A., McGrath, E. J., McIntosh, D. H., Mobasher, B., Robaina, A. R., Rosario, D., Straughn, A. N., van der Wel, A., and Villforth, C. (2012). CANDELS: Constraining the AGN-Merger Connection with Host Morphologies at z ˜ 2. ApJ, 744:148.

Komoroczi, A., Abe, S., and Urai, J. L. (2013). Meshless numerical modeling of brittleâĂŞviscous deformation: first results on boudinage and hydrofracturing using a coupling of discrete element method (DEM) and smoothed particle hydrodynamics (SPH). *Springer*, 17:373.

Komossa, S. (2001). X-Ray Evidence for Supermassive Black Holes at the Centers of Nearby Galaxies. In Knapen, J. H., Beckman, J. E., Shlosman, I., and Mahoney, T. J., editors, *The Central Kiloparsec of Starbursts and AGN: The La Palma Connection*, volume 249 of *Astronomical Society of the Pacific Conference Series*, page 450.

Kormendy, J. (1993). Kinematics of extragalactic bulges: evidence that some bulges are really disks. In Dejonghe, H. and Habing, H. J., editors, *Galactic Bulges*, volume 153 of *IAU Symposium*, page 209.

Kormendy, J. and Bender, R. (2009). Correlations between Supermassive Black Holes, Velocity Dispersions, and Mass Deficits in Elliptical Galaxies with Cores. ApJ, 691:L142–L146.

Kormendy, J. and Bender, R. (2011). Supermassive black holes do not correlate with dark matter haloes of galaxies. Nature, 469:377–380.

Kormendy, J., Bender, R., and Cornell, M. E. (2011). Supermassive black holes do not correlate with galaxy disks or pseudobulges. Nature, 469:374–376.

Kormendy, J. and Gebhardt, K. (2001). Supermassive black holes in galactic nuclei. In Wheeler, J. C. and Martel, H., editors, *20th Texas Symposium on relativistic astrophysics*, volume 586 of *American Institute of Physics Conference Series*, pages 363–381.

Kormendy, J., Gebhardt, K., and Richstone, D. (2000). The M − L bulge Correlation. In *American Astronomical Society Meeting Abstracts #196*, volume 32 of *Bulletin of the American Astronomical Society*, page 702.

Kormendy, J. and Ho, L. C. (2013). Coevolution (Or Not) of Supermassive Black Holes and Host Galaxies. ARA&A, 51:511–653.

Kormendy, J. and Richstone, D. (1995). Inward Bound—The Search For Supermassive Black Holes In Galactic Nuclei. ARA&A, 33:581.

Kriek, M., van Dokkum, P. G., Franx, M., Illingworth, G. D., Coppi, P., Förster Schreiber, N. M., Gawiser, E., Labbé, I., Lira, P., Marchesini, D., Quadri, R., Rudnick, G., Taylor, E. N., Urry, C. M., and van der Werf, P. P. (2007). The Origin of Line Emission in Massive z ~ 2.3 Galaxies: Evidence for Cosmic Downsizing of AGN Host Galaxies. ApJ, 669:776–790.

Kuijken, K. and Dubinski, J. (1995). Nearly Self-Consistent Disc / Bulge / Halo Models for Galaxies. MNRAS, 277:1341.

Lacey, C. and Cole, S. (1993). Merger rates in hierarchical models of galaxy formation. MNRAS, 262:627–649.

Lacy, M., Storrie-Lombardi, L. J., Sajina, A., Appleton, P. N., Armus, L., Chapman, S. C., Choi, P. I., Fadda, D., Fang, F., Frayer, D. T., Heinrichsen, I., Helou, G., Im, M., Marleau, F. R., Masci, F., Shupe, D. L., Soifer, B. T., Surace, J., Teplitz, H. I., Wilson, G., and Yan, L. (2004). Obscured and Unobscured Active Galactic Nuclei in the Spitzer Space Telescope First Look Survey. ApJS, 154:166–169.

Larson, R. B., Tinsley, B. M., and Caldwell, C. N. (1980). The evolution of disk galaxies and the origin of S0 galaxies. ApJ, 237:692–707.

Lidz, A., Hopkins, P. F., Cox, T. J., Hernquist, L., and Robertson, B. (2006). The Luminosity Dependence of Quasar Clustering. ApJ, 641:41–49.

Loeb, A. and Rasio, F. A. (1994). Collapse of primordial gas clouds and the formation of quasar black holes. ApJ, 432:52–61.

Lucy, L. B. (1977). A numerical approach to the testing of the fission hypothesis. AJ, 82:1013–1024.

Madau, P., Ferguson, H. C., Dickinson, M. E., Giavalisco, M., Steidel, C. C., and Fruchter, A. (1996). High-redshift galaxies in the Hubble Deep Field: colour selection and star formation history to z~4. MNRAS, 283:1388–1404.

Madau, P. and Rees, M. J. (2001). Massive Black Holes as Population III Remnants. ApJ, 551:L27–L30.

Magorrian, J., Tremaine, S., Richstone, D., Bender, R., Bower, G., Dressler, A., Faber, S. M., Gebhardt, K., Green, R., Grillmair, C., Kormendy, J., and Lauer, T. (1998). The Demography of Massive Dark Objects in Galaxy Centers. AJ, 115:2285–2305.

Marconi, A. and Hunt, L. K. (2003). The Relation between Black Hole Mass, Bulge Mass, and Near-Infrared Luminosity. ApJ, 589:L21–L24.

Martini, P. (2004). QSO Lifetimes. *Coevolution of Black Holes and Galaxies*, page 169.

McLure, R. J. and Dunlop, J. S. (2002). On the black hole-bulge mass relation in active and inactive galaxies. MNRAS, 331:795–804.

McNamara, B. R. and Nulsen, P. E. J. (2007). Heating Hot Atmospheres with Active Galactic Nuclei. ARA&A, 45:117–175.

Monaghan, J. J. (1992). Smoothed particle hydrodynamics. ARA&A, 30:543–574.

Monaghan, J. J. and Gingold, R. A. (1983). Shock Simulation by the Particle Method SPH. *Journal of Computational Physics*, 52:374.

Monaghan, J. J. and Lattanzio, J. C. (1985). A refined particle method for astrophysical problems. A&A, 149:135–143.

Moore, B., Lake, G., and Katz, N. (1998). Morphological Transformation from Galaxy Harassment. ApJ, 495:139–151.

Moster, B. P., Macciò, A. V., Somerville, R. S., Naab, T., and Cox, T. J. (2011). The effects of a hot gaseous halo in galaxy major mergers. MNRAS, 415:3750–3770.

Murray, N., Quataert, E., and Thompson, T. A. (2005). On the Maximum Luminosity of Galaxies and Their Central Black Holes: Feedback from Momentum-driven Winds. ApJ, 618:569–585.

Narayan, R., Mahadevan, R., and Quataert, E. (1998). *in Abramowicz M. A., Bjornsson G., Pringle J. E., eds, Theory of Black Hole Accretion Disks.* Cambridge Univ. Press, Cambridge.

Narayan, R. and Yi, I. (1994). Advection-dominated accretion: A self-similar solution. ApJ, 428:L13–L16.

NASA-WMAP Science team (2014). WMAP # 121238.

Navarro, J. F., Frenk, C. S., and White, S. D. M. (1996). The Structure of Cold Dark Matter Halos. ApJ, 462:563.

Navarro, J. F. and White, S. D. M. (1993). Simulations of Dissipative Galaxy Formation in Hierarchically Clustering Universes - Part One - Tests of the Code. MNRAS, 265:271.

Nayakshin, S. and Power, C. (2010). Simulations of momentum feedback by black hole winds. MNRAS, 402:789–802.

Nesvadba, N. P. H., Lehnert, M. D., De Breuck, C., Gilbert, A. M., and van Breugel, W. (2008). Evidence for powerful AGN winds at high redshift: dynamics of galactic outflows in radio galaxies during the "Quasar Era". A&A, 491:407–424.

Novak, G. S., Ostriker, J. P., and Ciotti, L. (2011). Feedback from Central Black Holes in Elliptical Galaxies: Two-dimensional Models Compared to One-dimensional Models. ApJ, 737:26.

Okamoto, T., Nemmen, R. S., and Bower, R. G. (2008). The impact of radio feedback from active galactic nuclei in cosmological simulations: formation of disc galaxies. MNRAS, 385:161–180. (ONB08).

Oppenheimer, B. D. and Davé, R. (2006). Cosmological simulations of intergalactic medium enrichment from galactic outflows. MNRAS, 373:1265–1292.

Orban de Xivry, G., Davies, R., Schartmann, M., Komossa, S., Marconi, A., Hicks, E., Engel, H., and Tacconi, L. (2011). The role of secular evolution in the black hole growth of narrow-line Seyfert 1 galaxies. MNRAS, 417:2721–2736.

Perlmutter, S., Turner, M. S., and White, M. (1999). Constraining Dark Energy with Type Ia Supernovae and Large-Scale Structure. *Physical Review Letters*, 83:670–673.

Ponti, G., Terrier, R., Goldwurm, A., Belanger, G., and Trap, G. (2010). Discovery of a Superluminal Fe K Echo at the Galactic Center: The Glorious Past of Sgr A* Preserved by Molecular Clouds. ApJ, 714:732–747.

Power, C., Nayakshin, S., and King, A. (2011). The accretion disc particle method for simulations of black hole feeding and feedback. MNRAS, 412:269–276. (PNK11).

Rasmussen, J., Sommer-Larsen, J., Pedersen, K., Toft, S., Benson, A., Bower, R. G., and Grove, L. F. (2009). Hot Gas Halos Around Disk Galaxies: Confronting Cosmological Simulations with Observations. ApJ, 697:79–93.

Rees, M. J., Begelman, M. C., Blandford, R. D., and Phinney, E. S. (1982). Ion-supported tori and the origin of radio jets. Nature, 295:17–21.

Ricotti, M., Ostriker, J. P., and Mack, K. J. (2008). Effect of Primordial Black Holes on the Cosmic Microwave Background and Cosmological Parameter Estimates. ApJ, 680:829–845.

Riess, A. G., Filippenko, A. V., Challis, P., Clocchiatti, A., Diercks, A., Garnavich, P. M., Gilliland, R. L., Hogan, C. J., Jha, S., Kirshner, R. P., Leibundgut, B., Phillips, M. M., Reiss, D., Schmidt, B. P., Schommer, R. A., Smith, R. C., Spyromilio, J., Stubbs, C., Suntzeff, N. B., and Tonry, J. (1998). Observational Evidence from Supernovae for an Accelerating Universe and a Cosmological Constant. AJ, 116:1009–1038.

Rubin, V. C. and Ford, Jr., W. K. (1970). Rotation of the Andromeda Nebula from a Spectroscopic Survey of Emission Regions. ApJ, 159:379.

Rubin, V. C., Thonnard, N., and Ford, Jr., W. K. (1978). Extended rotation curves of high-luminosity spiral galaxies. IV - Systematic dynamical properties, SA through SC. ApJ, 225:L107–L111.

Ryden, B. (2003). *Introduction to Cosmology.* Pearson Education Inc. Publishing as Addison Wesley.

Ryu, S. G., Nobukawa, M., Nakashima, S., Tsuru, T. G., Koyama, K., and Uchiyama, H. (2013). X-Ray Echo from the Sagittarius C Complex and 500-year Activity History of Sagittarius A*. PASJ, 65:33.

Salpeter, E. E. (1964). Accretion of Interstellar Matter by Massive Objects. ApJ, 140:796–800.

Schawinski, K., Evans, D. A., Virani, S., Urry, C. M., Keel, W. C., Natarajan, P., Lintott, C. J., Manning, A., Coppi, P., Kaviraj, S., Bamford, S. P., Józsa, G. I. G., Garrett, M., van Arkel, H., Gay, P., and Fortson, L. (2010). The Sudden Death of the Nearest Quasar. ApJ, 724:L30–L33.

Schaye, J., Crain, R. A., Bower, R. G., Furlong, M., Schaller, M., Theuns, T., Dalla Vecchia, C., Frenk, C. S., McCarthy, I. G., Helly, J. C., Jenkins, A., Rosas-Guevara, Y. M., White, S. D. M., Baes, M., Booth, C. M., Camps, P., Navarro, J. F., Qu, Y., Rahmati, A., Sawala, T., Thomas, P. A., and Trayford, J. (2015). The EAGLE project: simulating the evolution and assembly of galaxies and their environments. MNRAS, 446:521–554.

Schirmer, M., Diaz, R., Holhjem, K., Levenson, N. A., and Winge, C. (2013). A Sample of Seyfert-2 Galaxies with Ultraluminous Galaxy-wide Narrow-line Regions: Quasar Light Echoes? ApJ, 763:60.

Shakura, N. I. and Sunyaev, R. A. (1973). Black holes in binary systems. Observational appearance. A&A, 24:337–355.

Shankar, F., Salucci, P., Granato, G. L., De Zotti, G., and Danese, L. (2004). Supermassive black hole demography: the match between the local and accreted mass functions. MNRAS, 354:1020–1030.

119

Shankar, F., Weinberg, D. H., and Miralda-Escudé, J. (2013). Accretion-driven evolution of black holes: Eddington ratios, duty cycles and active galaxy fractions. MNRAS, 428:421–446.

Shapiro, P. R., Martel, H., Villumsen, J. V., and Owen, J. M. (1996). Adaptive Smoothed Particle Hydrodynamics, with Application to Cosmology: Methodology. ApJS, 103:269.

Shaver, P. A., Wall, J. V., Kellermann, K. I., Jackson, C. A., and Hawkins, M. R. S. (1996). Decrease in the space density of quasars at high redshift. Nature, 384:439–441.

Shi, Y., Rieke, G., Lotz, J., and Perez-Gonzalez, P. G. (2009). Role of Galaxy Mergers in Cosmic Star Formation History. ApJ, 697:1764–1783.

Shima, E., Matsuda, T., Takeda, H., and Sawada, K. (1985). Hydrodynamic calculations of axisymmetric accretion flow. MNRAS, 217:367–386.

Silk, J. and Mamon, G. A. (2012). The current status of galaxy formation. *Research in Astronomy and Astrophysics*, 12:917–946.

Silk, J. and Norman, C. (2009). Global Star Formation Revisited. ApJ, 700:262–275.

Silk, J. and Rees, M. J. (1998). Quasars and galaxy formation. A&A, 331:L1–L4.

Snyder, G. F., Hopkins, P. F., and Hernquist, L. (2011). Relation Between Globular Clusters and Supermassive Black Holes in Ellipticals as a Manifestation of the Black Hole Fundamental Plane. ApJ, 728:L24.

Soltan, A. (1982). Masses of quasars. MNRAS, 200:115–122.

Springel, V., Di Matteo, T., and Hernquist, L. (2005a). Modelling feedback from stars and black holes in galaxy mergers. MNRAS, 361:776–794. (SDH05).

Springel, V., White, S. D. M., Jenkins, A., Frenk, C. S., Yoshida, N., Gao, L., Navarro, J., Thacker, R., Croton, D., Helly, J., Peacock, J. A., Cole, S., Thomas, P., Couchman, H., Evrard, A., Colberg, J., and Pearce, F. (2005b). Simulations of the formation, evolution and clustering of galaxies and quasars. Nature, 435:629–636.

Stacy, A., Greif, T. H., and Bromm, V. (2012). The first stars: mass growth under protostellar feedback. MNRAS, 422:290–309.

Steidel, C. C., Hunt, M. P., Shapley, A. E., Adelberger, K. L., Pettini, M., Dickinson, M., and Giavalisco, M. (2002). The Population of Faint Optically Selected Active Galactic Nuclei at z ~ 3. ApJ, 576:653–659.

Subramanian, K., Rees, M. J., and Chitre, S. M. (1987). Gravitational lensing by dark galactic haloes. MNRAS, 224:283–298.

Taranu, D. S., Dubinski, J., and Yee, H. K. C. (2013). Mergers in Galaxy Groups. I. Structure and Properties of Elliptical Remnants. ApJ, 778:61.

Taylor, P. and Kobayashi, C. (2014). Seeding black holes in cosmological simulations. MNRAS, 442:2751–2767.

Thacker, R. J. and Couchman, H. M. P. (2000). Implementing Feedback in Simulations of Galaxy Formation: A Survey of Methods. ApJ, 545:728–752.

Thacker, R. J. and Couchman, H. M. P. (2006). A parallel adaptive P^{3}M code with hierarchical particle reordering. *Computer Physics Communications*, 174:540–554.

Thacker, R. J., MacMackin, C., Wurster, J., and Hobbs, A. (2014). AGN feedback models: correlations with star formation and observational implications of time evolution. MNRAS, 443:1125–1141.

Thomas, P. A. and Couchman, H. M. P. (1992). Simulating the formation of a cluster of galaxies. MNRAS, 257:11–31.

Treister, E. and Urry, C. M. (2012). The Cosmic History of Black Hole Growth from Deep Multiwavelength Surveys. *Advances in Astronomy*, 2012:16.

Tremaine, S., Gebhardt, K., Bender, R., Bower, G., Dressler, A., Faber, S. M., Filippenko, A. V., Green, R., Grillmair, C., Ho, L. C., Kormendy, J., Lauer, T. R., Magorrian, J., Pinkney, J., and Richstone, D. (2002). The Slope of the Black Hole Mass versus Velocity Dispersion Correlation. ApJ, 574:740–753.

Turk, M. J., Abel, T., and O'Shea, B. (2009). The Formation of Population III Binaries from Cosmological Initial Conditions. *Science*, 325:601–.

Ueda, Y., Akiyama, M., Ohta, K., and Miyaji, T. (2003). Cosmological Evolution of the Hard X-Ray Active Galactic Nucleus Luminosity Function and the Origin of the Hard X-Ray Background. ApJ, 598:886–908.

Umemura, M. (2001). A Radiation-Hydrodynamical Model for Supermassive Black Hole-to-Bulge Mass Relation and Quasar Formation. ApJ, 560:L29–L32.

van Albada, T. S., Bahcall, J. N., Begeman, K., and Sancisi, R. (1985). Distribution of dark matter in the spiral galaxy NGC 3198. ApJ, 295:305–313.

Vasudevan, R. V. and Fabian, A. C. (2007). Piecing together the X-ray background: bolometric corrections for active galactic nuclei. MNRAS, 381:1235–1251.

Vogelsberger, M., Genel, S., Springel, V., Torrey, P., Sijacki, D., Xu, D., Snyder, G., Nelson, D., and Hernquist, L. (2014). Introducing the Illustris Project: simulating the coevolution of dark and visible matter in the Universe. MNRAS, 444:1518–1547.

Widrow, L. M. and Dubinski, J. (2005). Equilibrium Disk-Bulge-Halo Models for the Milky Way and Andromeda Galaxies. ApJ, 631:838–855.

Widrow, L. M., Pym, B., and Dubinski, J. (2008). Dynamical Blueprints for Galaxies. ApJ, 679:1239–1259.

Williamson, D. J. and Thacker, R. J. (2012). Effective viscosity from cloud-cloud collisions in 3D global smoothed particle hydrodynamics simulations. MNRAS, 421:2170–2186.

Woods, D. F., Geller, M. J., and Barton, E. J. (2006). Tidally Triggered Star Formation in Close Pairs of Galaxies: Major and Minor Interactions. AJ, 132:197–209.

Wurster, J. and Thacker, R. J. (2013a). A comparative study of AGN feedback algorithms. MNRAS, 431:2513–2534.

Wurster, J. and Thacker, R. J. (2013b). Accretion disc particle accretion in major merger simulations. MNRAS, 431:539–553.

Yu, Q. and Lu, Y. (2008). Toward Precise Constraints on the Growth of Massive Black Holes. ApJ, 689:732–754.

Yu, Q., Lu, Y., and Kauffmann, G. (2005). Evolution of Accretion Disks around Massive Black Holes: Constraints from the Demography of Active Galactic Nuclei. ApJ, 634:901–909.

Yu, Q. and Tremaine, S. (2002). Observational constraints on growth of massive black holes. MNRAS, 335:965–976.

Zubovas, K., King, A. R., and Nayakshin, S. (2011). The Milky Way's Fermi bubbles: echoes of the last quasar outburst? MNRAS, 415:L21–L25.

Zubovas, K. and Nayakshin, S. (2012). Fermi bubbles in the Milky Way: the closest AGN feedback laboratory courtesy of Sgr A*? MNRAS, 424:666–683.

Zubovas, K., Nayakshin, S., King, A., and Wilkinson, M. (2013). AGN outflows trigger starbursts in gas-rich galaxies. MNRAS, 433:3079–3090.

Zwicky, F. (1933). Die Rotverschiebung von extragalaktischen Nebeln. *Helvetica Physica Acta*, 6:110–127.

Zwicky, F. (1937). On the Masses of Nebulae and of Clusters of Nebulae. ApJ, 86:217.